Influence of Turbulence on Fuel Slick Fires with an Immersed Conductive Object

By

Li Chang

A Dissertation

Submitted to the Faculty

of

WORCESTER POLYTECHNIC INSTITUTE

in partial fulfillment of the requirements for the

Degree of Doctor of Philosophy

in

Fire Protection Engineering

Sept 2021

Approved:

_____

Professor Ali S. Rangwala, Worcester Polytechnic Institute, Advisor

_____

Professor Albert Simeoni, Committee Member

_____

Professor Chih-Jen (Jackie) Sung, Committee Member

_____

Doctor Harri Kytomaa, Committee Member

_____

Professor Seong-Kyun Im, Committee Member

Abstract

The hazard associated with crude oil spills has been a major environmental concern as the increasing demands of offshore drilling and oil tanker transport in recent decades. The burning of hydrocarbon liquid fuel floating on water has been a problem of great interest, as it forms the theoretical basis of the oil spill clean-up technique called *in-situ* burning (ISB). To understand the burning behavior of such configuration, this study analyzes the problem of a floating liquid fuel on wavy water by introducing a bench-scale platform capable of simulating ocean-like turbulent conditions in a controllable fashion. Further, this study investigates the application of an immersed conductive metal for burning enhancement under turbulent conditions.

A series of lab-scale experiments are designed to systematically investigate the fuel layer burning with the turbulent water sublayer and the immersed metal object. The first set of experiment studies the subcooled nucleate boiling using an electrically heated thin nichrome wire in a dodecane layer that sits on a turbulence water surface. The surface turbulence is generated by a confined-jet cylinder platform. Four stages of bubble behaviors are observed characterizing different regions of the nucleate boiling curve. They are, respectively: sweeping stage, bouncing and merging stage, hanging stage, and film boiling stage. Bubble departure frequency (BDF) and critical heat flux (CHF) increase as a function of turbulence intensity represented by root-mean-square (RMS) velocity. Bubble departure size decreases as a function of turbulence RMS velocity. Bubble propulsion mechanism is dominated by two competing factors: Marangoni force and thermocapillary convection. Both are subject to the impact of turbulent eddies, which facilitates the bubble lift-off, and improves the heat transfer performance.

The second set of experiments are conducted to understand the influence of surface turbulence on the crude oil slick burning on a water bath. As the turbulence intensity increases, a mitigated burning process with smaller flame height and boilover behavior is observed. The thermocouple array measurements indicate that the water sublayer cannot develop temperature gradients even at the low level of turbulence intensity at $u' = 0.017$ m/s. The heat reaching the water is instantly taken away because of the turbulent mixing thus facilitating the heat loss of the oil slick, which causes a reduction in MLR up to 34% at $u' = 0.033$ m/s compared to baseline. The convective heat transfer coefficient in the water sublayer is obtained by matching the one-dimensional

conduction model to the measurement data and has the values of $h_{conv} = 78, 93, 125$ W/m^2 corresponding to turbulence intensity $u' = 0.017, 0.025, 0.033$ m/s. The heat and mass transfer characteristics during the oil slick burning are highly related and both are subject to the impact of the presence of turbulence in the water sublayer.

The final sets of the experiments study the heptane and dodecane layer burning on a turbulence water surface with an immersed copper rod. Under zero turbulence condition ($u' = 0$ m/s), the fuel layer burning rate is noticeably affected by the fuel type, or more specifically, the boiling point of the fuel compared to the water boiling point. The dodecane layer (boiling point of 216 °C) burning cases has nucleate boiling on the rod's surface in the water sublayer, while the nucleate boiling occurs on the rod's surface within the fuel layer in heptane layer (boiling point of 98 °C) burning cases. The different nucleate boiling region causes suppression and facilitation on the dodecane and heptane burning rate respectively. The heat transfer by bubble generation is estimated by bubble counting using highspeed image processing. While the nucleate boiling is not observed for both types of fuel on the rod's surface under turbulence conditions ($u' = 0.017$ and 0.033 m/s), the suppression and facilitation effects by bubbles in no turbulence condition are no longer in consideration, and the convective heat loss at the water interface become a major factor. For each burning configuration, a burning rate formulation coupled with experimental results is used to capture the details in the heat and mass transfer features.

Finally, a theoretical analysis on the effects of multiple copper rods placement is studied using the measurement data adopted from the experiments. The results predict an over 300% increase for dodecane burning rate when 4 copper rods with diameter of 10 mm are immersed in the fuel layer under turbulence intensity of $u' = 0.03$ m/s. For heptane burning cases, the burning rate increases to more than 400% the baseline when 3 rods are immersed in the fuel slick. This analysis provides a reasonable engineering basis to determine the number of the copper rods required for the Flame Refluxer™ design to achieve a certain level of enhancement.

Acknowledgments

I would like to express my sincere gratitude to my advisor, Prof. Ali S. Rangwala for his guidance since the beginning. I feel lucky enough to have him as my advisor and a few lines cannot express my thankfulness. It is his patience and knowledge that helped me through the challenges in many aspects.

Also, I would like to thank Prof. Albert Simeoni, Prof. Chih-Jen Sung, Dr. Harri Kytomaa, and Prof. Seong-Kyun Im as my dissertation committee. Their valuable comments and precious advice helped me complete this work.

I will remember all my colleagues and friends I once worked with in the WPI Combustion Lab: Kemal, Hamed, Suhas, Mahesh, Pi, Sharanya, Gio, Veronica, Nate, Matt, Chuming. I want to thank them all here.

And I want to thank my lovely host family parents for caring about me since the first time I visited U.S. ten years ago. Finally, I would like to thank my dear parents for their priceless love and support. They are amazing in any possible way, and they always have my back, encouraging me to keep on going.

Contents

List of Tables

List of Figures

13

Nomenclature

A_1, A_R	Rod cross-section area
A_2	Rod surface area within fuel layer
$A_3, A_{r,w}$	Rod surface area within water layer
A_F	Fuel surface area
A_P	Pool surface area
B	Spalding B number
$c_{p,air}$	Specific heat of air
$c_{p,F}$	Specific heat of fuel
$c_{p,W}$	Specific heat of water
d	Inner diameter of the jet nozzle
d_w	Diameter of the wire
d_r	Diameter of the rod
D	Diameter of the pool
D_B	Diameter of the bubble
F_b	Buoyancy force
F_d	Drag force
F_f	Friction force
F_g	Gravitational force
F_{ma}	Marangoni force
h_{conv}	Convective heat transfer coefficient
g	Gravitational acceleration
Δh	Vertical height variant
$H_v, \Delta H_F$	Latent heat of vaporization
H	Vertical distance between surface and nozzle
H_f	Thickness of the fuel layer
H_w	Thickness of the rod immersed water layer
I	Electric current
k_F	Thermal conductivity of fuel
L	Fuel initial thickness
L_F	Heat of gasification of fuel
$\dot{m}_F$	Mass loss rate
N	Number of discrete turbulence data points
Nu_D	Nusselt number around the rod
$\dot{q}''$	Surface heat flux
$\dot{q}''_{cond}$	Conductive heat flux
$\dot{q}_e$	External heat transfer from the rod
$\dot{q}_{loss}$	Heat loss
$\dot{q}''_S$	Flame heat flux
$\dot{q}''_{vap}$	Surface heat flux used for vaporization
Q	Volumetric flow rate
$\dot{Q}_{e,fuel}$	Energy transferred from the rod to the fuel layer

$\dot{Q}_{e,water}$ Energy transferred from the rod to the water layer
r Regression rate
R Resistance of the wire
$R(t)$ Autocorrelation function
Re_D Reynolds number around the rod bottom
S Distance between thermal couple measurement locations
$t_{p,d}$ Thermal penetration time in dodecane layer
T_1 Temperature of the bubble top region
T_2 Temperature of the bubble bottom region
T_b Boiling point
T_f Flame temperature
T_R Surface temperature on the rod
T_S Surface temperature of the fuel
T_{wire} Temperature of the wire
T_{sat} Saturation temperature
u', u_{rms} Root-mean-square velocity, turbulence intensity in horizontal direction
u_i Turbulence velocity
$\bar{u}$ Mean flow velocity
U Voltage
v' Root-mean-square velocity, turbulence intensity in vertical direction

Geek

Λ Turbulence integral length scale
α Electric resistance and temperature coefficient, thermal diffusivity
α_F Thermal diffusivity of fuel
τ Turbulence characteristic time
σ Surface tension
ρ_F Density of fuel
ρ_∞ Density of ambient air
χ Specific fraction of energy feedback to the fuel surface

Subscripts

F, fuel   Fuel
g Gas phase
int   Fuel/water interface
rod   Rod
surf   Fuel surface
W   Water sublayer
+   Immediately above the interface
−   Immediately beneath the interface

Chapter 1: Introduction

1.1 *In-situ* burning

Oil spills have been some of the most challenging accidents harming the environment and natural reserves. Even today and foreseeable future, the increasing demand for fossil fuel around the globe forces us to be faced with this painstaking process to clean up the spilled oil. In 2010, the Deepwater Horizon oil spill constituted an ecosystem-level injury in the northern Gulf of Mexico where 3.19 million barrels of oil (50,000 m^3) were released into the ocean [1]. Over the years, in-situ burning (ISB) has become an accepted disposal method for spill clean-up [2–4]. During the Deepwater Horizon accident, 411 separate ISB events consumed up to 310,000 barrels of floating crude oil [5]. However, the average regression rate for large-size pool fire is only about 3.5 mm/min [6], which is low compare to the clean-up capacity of a major spill accident. In addition, because of the ocean being a massive heat sink, the burning efficiency is affected by the insufficient temperature of the burning oil slick. In the conventional ISB process, the heat feedback from the flame zone is limited due to the buoyancy-induced convection (thermal plume) and radiation loss to the ambient [7]. Only a small amount of the heating energy is captured by the fuel layer for vaporization and combustion [8].

The earlier studies on the combustion of crude and fuel oils on water bed were focused since the 1970s as a tool to mitigate spill accidents [9–16]. Works done by Blinov and Khudyakov [6] demonstrated a thoroughly experimental analysis covering multiple aspects of liquid pool burnings, which included ignition, burning rate, flame spread, water effects, extinction, etc. The work of Thompson et al. [9] set down the guideline that attempted to analyze the process of oil spill burning, which provided the perspective of using ISB as the response to spill accidents in practice. A review by Evans et al. [17] introduced the ISB related research conducted by the National Institute of Standards and Technology (NIST) to understand and predict the important features of burning oil on water. In addition to ISB large field experiments, smaller scale pool fires were also conducted, which allowed closer observations and finer measurements. Arai et al. [18] analyzed pool fires of liquid fuel floating on water bed with pool diameters varying from 4.8, 9.8, and 20.3 cm. The results showed that for a small pool fire system, the boiling of the water sublayer during boilover

would cause a decrease in both flame height and mass burning rate with the process of combustion, while the large pool fires showed opposite results. Garo et al. [19] studied the boilover burning of oil on a 15 cm water pan. The results indicated that the boilover intensity appeared related to the initial oil-layer thickness and pan diameter. Discussions were elevated to the macro-scale: surface tension effects, and growth and expansion of the water bubble at the nucleation sites. A 1-D heat conduction model was calculated to compare with experimental temperature distribution history. They included the effect of the fuel boiling point in the following study [20], where a transparent pyrex pan was used and with the help of a video camera illuminated by a laser sheet, the visualization of the burning fuel slick was made possible. Based on those works, Torero et al. [21] provided a more complete engineering model to the complex ISB process. Their analytical expression described the effects of pool diameter and initial fuel layer thickness, and a 1-D conduction model was developed to model thermal diffusion in both fuel and water layers. The experiments showed that only a small fraction (the order of 1%) of heat released by the flame is retained by the fuel layer and water bath. These pioneer research paved the way to study ISB and showed that the key challenge of this process is the limited heat feedback from the flame to fuel layers.

1.2 Conductive objects in pool fire

The idea of altering the thermal coupling effects in pool fires by a simple placement of conductive objects started to grow in recent years. Some early studies [6,22–24] have investigated the effects of nearby or flame-engulfed objects on pool fires. However, in all studies, the object was analyzed only be the flames and not in contact with the liquid. The primary purpose of these studies was to analyze the structural response of for example an airplane fuselage engulfed by a pool fire. Recently, a novel experimental approach to enhance the burning of oil-water emulsions by immersed objects (Flame Refluxer^{TM}) was introduced by Rangwala et al. [25], where the hexane burning rate in a 0.1 m pan was increased up to 10 times and 6 times in 1 m pan respectively. The concept was followed by other researchers and was the fundamental inspiration of this work. Sezer et al. [26,27] developed a computational model to predict the mass loss rate of the pool fires with thermally conductive objects and metal mesh blankets. Arsava et al. [28–30] further studied the ISB enhancement concept using a copper porous mesh to heat the oil layer with conical copper coils to collect heat from the flame. The ISB experiments on a thin slick of crude oil resting on

water achieved an efficiency of ~400% above baseline in 0.28 m pan and 500-700% in a 1.2 m pan. As a key to enhance the burning rate is to find a way to direct the heat from the flame zone back into the burning oil layer. The formation of nucleating bubbles at the immersed FR surface is believed to be essential for the mass and heat transfer enhancement in a pool fire [31]. As additional fuel vapor is directly released into the flame upon bubble bursting at the fuel surface, this mechanism is very similar to the burning facilitation because of boilover [18–21]. While boilover requires a certain level of superheated water sublayer to occur, the advantage of FR is that the enhancement can take place throughout the entire burn. Because the metal FR surface temperature can easily reach the fuel's boiling temperature, once the onset of nucleation occurs the heat feedback circle through the immersed object will be further boosted with increased boiling heat transfer coefficient. However, the gap between the nucleating bubbles and the theoretical model was not completely understood. The current work will connect bubbles' nucleation latent energy with the mass transfer number in a more precise fashion. Besides, the turbulence effect will be included to match with the real ISB environment.

1.3 Ocean turbulence

Turbulence is the dominant physical process in the transfer of momentum and heat, and in dispersing small particles in the natural water resources. Ocean turbulence is similar to the turbulence in other naturally occurring fluid motions and in flows generated in engineering applications. The sea surface is covered by wind-driven waves [32], injecting momentum into the underlaying sea water. The water immediately below the surface is generally in the state of irregular motion that is refer to as "turbulence" [33]. The turbulence in the ocean surface layer is a medium in the transfer of momentum, heat, freshwater, particulates, and gases between the ocean and atmosphere [34].

In the 1940s, Kolmogorov hypothesized that the distribution of eddy sizes should depend on only two parameters: the dissipation rate and the viscosity. Thus, for all types of turbulence, from flow over a wing to convection in the interior of the planet, appear as manifestations of a single process whose form depends only on the viscosity of the fluid and the rate at which energy cascades towards smaller scales [35]. This is generally regarded as the beginning of the modern era of

turbulence theory. The energy cascade concept was also brought up early in the 1922 by Richardson who immortalized his idea in the verse quoted as:

"Big whorls have little whorls

That feed on their velocity

And little whorls have lesser whorls

And so on to viscosity"

1.4 Lab-scale turbulence platform

The generation of controllable lab-scale turbulence has been a great demand as it is the foundation of various studies related to dynamic water conditions. Such as the study of particle sediment in a river bed [36], the evaporation rate of liquid natural gas during transport [37] and so on. For *in-situ* burning process, the fuel slick is directly under the effects of the turbulent water sublayer. To carefully examine such effects, a structurally simplified type of turbulence, also referred to as isotropic turbulence is applied in this work. Isotropic turbulence is an ideal version of realistic turbulence, but it is suitable for analytical studies. The experimental platform used in this work is motivated by the studies using upward confined jet to generate surface isotropic turbulence [36–40] due to its applicability during a pool fire. Based on the theoretical study [41] on the structure of an axisymmetric confined jet, the jet boundary would fill the cylindrical cross-section when the distance from the jet nozzle was more than three times the confinement diameter. After this distance, the turbulent velocity fluctuations began to dominate over the mean circulatory velocity. Sonin et al. [38] applied the confined jet configuration to generated isotropic surface turbulence, and polypropylene spheres were used to trace the turbulent surface for velocity fluctuation measurements. More accurate measurement techniques such as Laser Doppler Velocimetry (LDV) by Brown et al. [39] and Particle Image Velocimetry (PIV) by Khoo et al. [42] were used to verify the isotropic characteristics of the surface turbulence using a similar setup. The results showed that the turbulence velocity components in vertical and horizontal directions become nearly uniform or isotropic in a horizontal plane above three times the confinement diameter. This zone of isotropic turbulence is an ideal experimental platform to analyze the role of turbulence on pool fires coupled with sub-cool nucleate boiling. The turbulence can be controlled by adjusting the velocity levels

19

at the nozzle so that turbulence corresponding to open water resources can be obtained in a laboratory environment. In this work, PIV is used to measure the surface region turbulence and the results are compared with the natural water resources turbulence data. The studies on bubble behaviors (departure frequency, bubble size, bubble dynamics) in such pool fire configuration are very limited, and to add turbulence at the surface region has never been looked into.

1.5 Research objectives
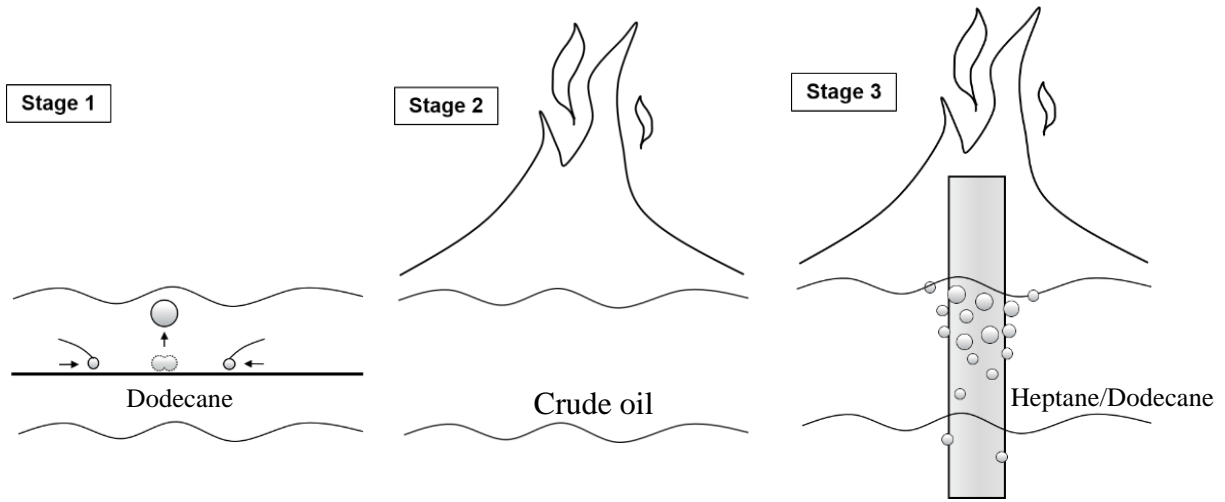
Figure 1. 1: Schematic of experimental Stage 1, 2, and 3.

This study analyzes the problem of a floating liquid fuel on wavy water by introducing a bench-scale platform capable of simulating ocean-like turbulent conditions in a controllable fashion. Further, this study investigates the application of an immersed conductive metal for burning enhancement under turbulent conditions. Previous studies have shown that by placing metal objects between the flame and fuel layer, the sustained nucleate boiling at the immersed metal section would facilitate the heat and mass transfer and eventually faster burnout of the floating fuel layer. However, the behavior of the bubbles and their interaction with a turbulent field induced by the action of waves for example remains unexplored. As shown in Figure 1.1, this study peels of the complexity stage by stage and analyzes the problem with 3 experiment stages: 1) Subcooled nucleate boiling experiments using thin nichrome wire in dodecane layer in Chapter 2, 2) Crude oil slick burning in Chapter 3, and 3) Heptane and dodecane fuel slick burning with an immersed copper rod in Chapter 4.

Figure 1.2 shows a floating fuel slick pool fire with an immersed copper rod. Both fuel and water layers are made turbulent. The bottom of the copper rod reaches into the water so that the collected heat is dissipated into fuel ($\dot{Q}_{e,fuel}$) and water ($\dot{Q}_{e,water}$) as external heat sources to different liquid layers.
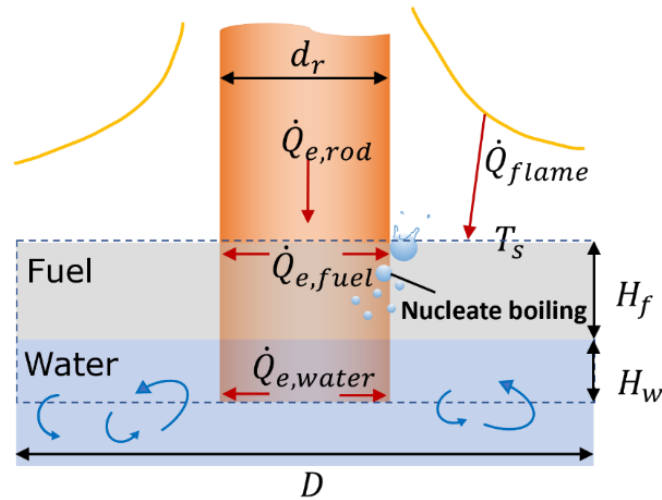
Figure 1. 2: Schematic of the floating fuel layer burning on water with immersed copper rod and turbulence.

The study of the burning rate under such complex settings, the experiment will start with the baseline condition which is fuel slick burning without immersed copper rod and turbulence. Then process to fuel slick burning with the copper rod but without turbulence. They pave the way to the final phase which is to have the copper rod and turbulence together. The initial fuel thickness and rod position will be constant throughout the whole study. The varying parameters are rod diameter, fuel type, and turbulence strength. The following questions will be answered:

1. What is the influence of turbulence on sub-cooled nucleate boiling heat transfer and how does the bubble behavior vary?

2. How will turbulence affect the burning of floating oil slick?

3. Which parameters (turbulence strength, copper rod diameter) are influential in determining the burning rate of the fuel slick? How to model the mass burning rate?

Chapter 2: Subcooled nucleate boiling experiments using thin nichrome wire in dodecane layer

2.1 Introduction

As an effective way to enhance heat transfer, subcooled boiling has been studied extensively in the last decades. A typical way of investigating heat transfer under the boiling phenomenon is by submerging a heated element in a liquid pool at ambient temperature with bubble generation taking heat away from the hot surface, which is known as subcooled nucleate pool boiling. Among previous experiments, nucleate boiling on many varieties of metals in different shapes and configurations were investigated, such as thin wires [43–50], strips [51,52], tubes [53–56], and plates [43,57–63].

A comprehensive study by Bergles et al. [64] reported that the surrounding liquid environment plays an important role in terms of affecting heat transfer characteristics by vortex flow, fluid vibration, electrostatic field, and additives. Saturation pressure and thermal properties of working fluids are some other major parameters [65]. Apart from the intrinsic properties of the liquid, nucleate boiling in flow environments was investigated mainly for the interests of cooling effects on the deceleration rods in nuclear power plants and other high-heat flux management. Griffith [59] conducted forced convection boiling experiments using a copper plate in a flow created by a continuous pump. Results showed bubble departure size decreased with increasing flow velocity, and flow drag force was normally smaller than the buoyant force and surface force. Situ et al. [66] studied bubble behaviors of boiling flow experiments within a vertical upward annular channel. Bubble departure frequency (BDF) was correlated with nucleate boiling heat flux, where the correlation was examined by data from similar flow boiling experiments done by Thorncroft et al. [52] and Base et al. [67]. All studies related to flow boiling were performed in one-directional flows. Nucleate boiling in an isotropic turbulent environment surprisingly has rarely been focused on, while this question calls for more understanding.

Based on the studies on turbulence in natural water resources [32,34], the water surface region shows turbulent characteristics because of the wind-driven mechanisms and confinements of

geographic terrains. Large eddies gradually deform into smaller eddies and eventually dissipate in the environment as heat [33,68]. The complexity of the turbulence might easily defy the experiment analysis. Therefore, a structural simplified type of turbulence is created in the lab-scale to deal with this issue, which is referred to as isotropic turbulence. By definition, isotropic turbulence is invariant with direction and with no bulk flow. Among previous literature, two methods have been used to create isotropic turbulence in small-scale water tanks. The first method is by directing a confined jet upwards from the bottom of a cylindrical container [36–39,42], and the second method is by using an oscillating grid at the bottom of a water tank [69–71]. The experimental platform in this work is motivated by the studies using upward confined jet to generate surface isotropic turbulence due to its applicability during a pool fire experiment.

Based on the theoretical study [41] on the structure of an axisymmetric confined jet, the jet boundary fills up the cylindrical cross-section when the distance from the jet nozzle reaches more than three times the confinement diameter. After this distance, the turbulent velocity fluctuations begin to dominate over the mean circulatory velocity. Sonin et al. [38] apply such confined jet configuration to generate isotropic surface turbulence, and polypropylene spheres are used to trace the turbulent surface for velocity fluctuation measurements. More accurate measurement techniques such as Laser Doppler Velocimetry (LDV) by Brown et al. [39] and Particle Image Velocimetry (PIV) by Khoo et al. [42] are used to verify the isotropic characteristics of the surface turbulence using similar setups. The results show that the turbulence velocity components in vertical and horizontal directions become nearly uniform or isotropic in a horizontal plane above three times the confinement diameter. By controlling the flow rate through the jet nozzle, the turbulence intensity can be set at an exact range of values.

Compared with previous nucleate boiling studies, the isotropic turbulence adds to the facts that influence existing bubble propulsion mechanisms, which allows an insight into the interconnected relationships between turbulence strength, bubble behavior, and heat transfer characteristic.

2.2 Experimental setup

2.2.1 Description of apparatus

23

Figure 2.1 shows a schematic of the experimental apparatus used in this study. The experiments were performed in a cylindrical Pyrex glass tube with an inner diameter D = 100 mm. The tube was filled with water up to a height of H = 330 mm from the nozzle. The Pyrex glass tube was surrounded by a 180 mm x 180 mm rectangular acrylic tank. A thickness of a 40 mm dodecane fuel layer was carefully added on top as shown in Figure 2.1. At the bottom of the Pyrex glass tube, a cylindrical jet nozzle with diameter d = 12.7 mm was placed at the center location, from which a centrifugal pump drove water jet upwards. Next to the center jet nozzle, two suction ports were fixed symmetrically to feed water back into the centrifugal pump. The layout was to ensure a symmetric profile of the jet. A turbine type flowmeter and a control valve were installed in the pipeline to adjust the flow rate, Q. Studies have shown when the distance between the region of interest and the nozzle is more than three times of the diameter of the confinement, the jet boundary will attach to the confinement wall, after which the vertical momentum of the jet will be distributed horizontally [40]. The results showed that the horizontal velocity component of the turbulence increased to a similar magnitude as the vertical velocity component. Particle Image Velocimetry (PIV) technic was used to measure the turbulence velocity near the surface.

The nucleate boiling experiments were performed using thin nichrome wire with a length, l = 70 mm and diameter, d = 0.127 mm. The nichrome wire was fixed at the bottom of two copper rods which acted as electrodes 20 mm below the surface of the dodecane layer as shown in Figure 2.1. The diameter of the copper rods was 12.8 mm, comparing which to the thin nichrome wire, the electric resistance of the copper rods was negligible. The copper rods were fixed by a wood ladder structure to ensure constant tension on the nichrome wire for each experiment, therefore mitigated the resistance change due to wire stretch. A DC power supply (Mastech DC Power Supply HY5005E-2) was used to heat the wire and two digital multimeters (Fluke 45 Dual Display Digital Multimeter and Keithley 2110 Digital Multimeter) were used to measure voltage, U and current, I of the nichrome wire (Fig. 2.1). Heat flux, $\dot{q}''$ (kW/m^2) on the surface of nichrome wire is expressed as:

$$\dot{q}'' = \frac{UI}{\pi dl} \; , \tag{1.1}$$

An indirect wire temperature measuring method by the calibrated relationship between temperature and resistance introduced in studies [43,47] was adopted because of the difficulty of using thermocouples or other direct measurements. The resistance of the wire varied linearly with the wire temperature and the temperature coefficient of resistance was calculated using 3 repeated experiments as $\alpha = 9 \times 10^{-4}$ Ω/°C. Before each experiment, the initial resistance of the nichrome wire was measured at room temperature. During the experiment, the power supply output was gradually increased, at the same time the wire resistance was recorded as $R = U/I$, therefore the corresponding average wire temperature was obtained. Each experiment was performed three times, and the nichrome wire was replaced after each experiment.

To capture the bubble behaviors, a high-speed camera (Chronos 1.4) with a macro-lens was used. The frame rate of the high-speed camera was set to 2111 frames per second (FPS), giving a corresponding pixel resolution of 1280 x 512 recording at the center portion of the nichrome wire. A LED light (Godox SL-100W) was placed at the back of the experimental facility. A thin white cloth was placed on the back of the rectangular acrylic tank, creating a bright and soft background for high-speed recording. Also, a DSLR (Canon 5D Mark III) was used to observe the entire length of wire to measure bubble departure frequency (BDF) and bubble departure size, D_B. Each measurement was averaged over a 60-second duration. The standard error of bubble departure size measurement is 1.7%.
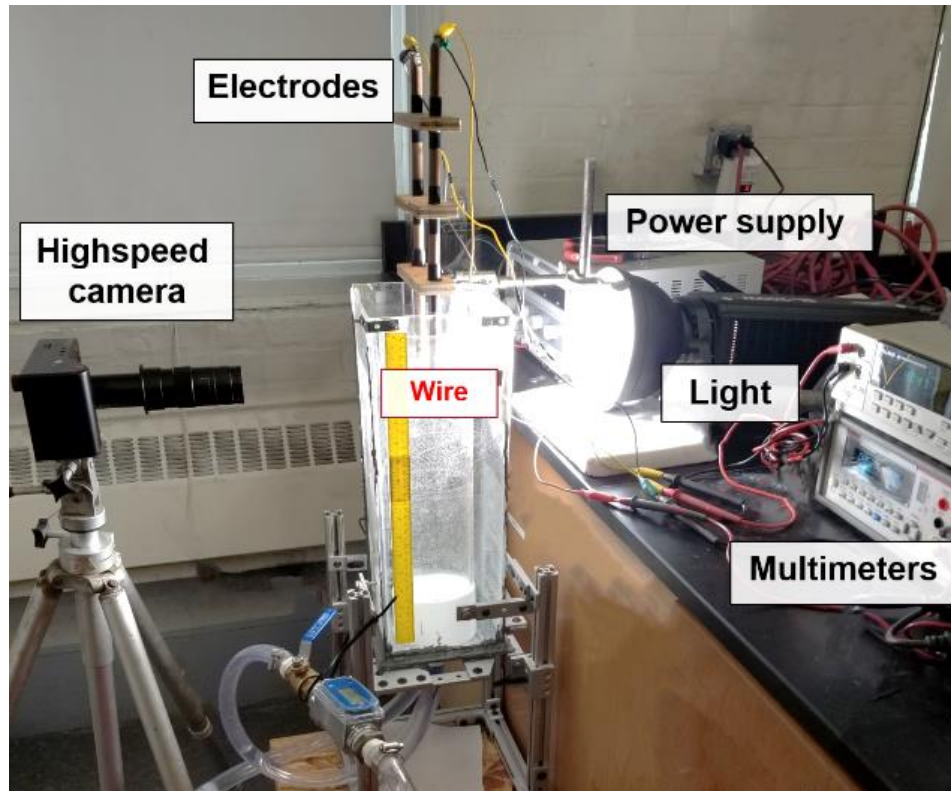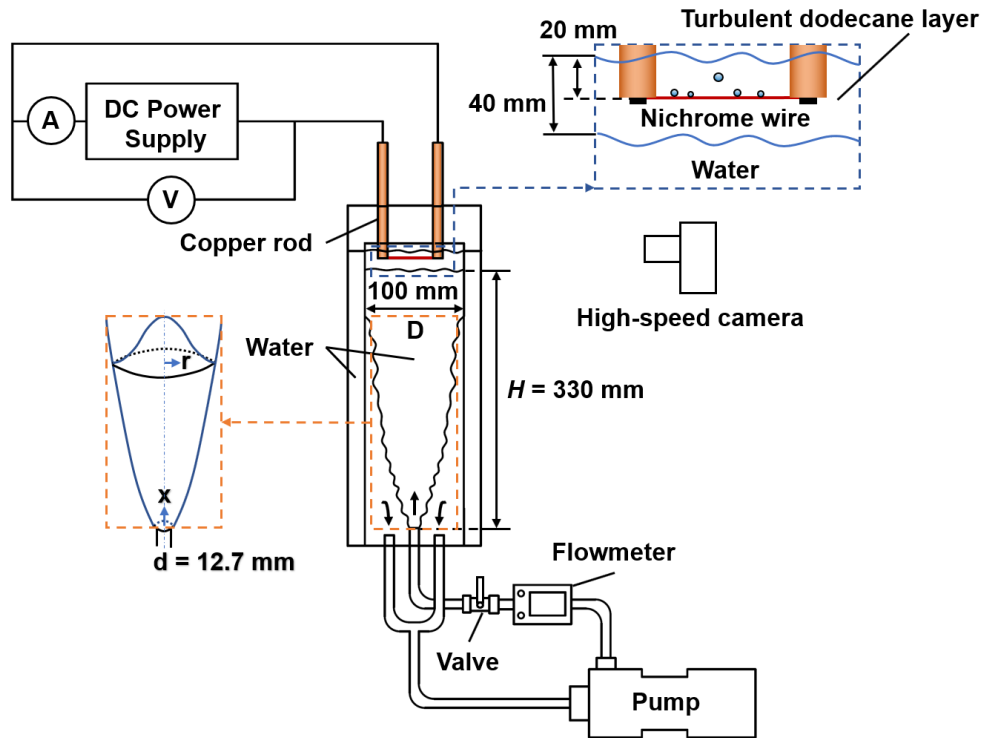
Figure 2. 1: Nucleate boiling experimental setup with turbulence generation system. 40 mm thick dodecane is poured on top of a water sublayer.

2.2.2 Measurement of turbulence

The turbulence root-mean-square (RMS) velocity was measured before the nucleate boiling experiments, and the relationship between turbulence and water flow rate through the nozzle at the bottom was determined. The measurement domain was set to be 350 mm vertically away from the nozzle, which is the same level of nichrome wire elevation in nucleate boiling experiments. PIV was used to measure velocity at a series of discrete points, u_i in both vertical and horizontal directions. The turbulence strength given by RMS velocity was calculated as:

$$u_{rms} = \sqrt{\frac{1}{N}\sum_{i=1}^{N}(u_i - \bar{u})^2} \ , \tag{1.2}$$

where, N is the number of discrete data points. $(u_i - \bar{u})$ represents the turbulent fluctuation, and mean velocity, $\bar{u}$ is calculated as:

$$\bar{u} = \frac{1}{N}\sum_{1}^{N} u_i \ , \tag{1.3}$$

PIV method requires trace particles seeded in the turbulent fluid. Air bubbles with an average diameter of 100 μm were used as the seeding particles. The diameter was measured based on the length per pixel from the captured images. The tracers of such size were reported to have a velocity deviation of 5% because of gravitational force in 10 cm/s water flow [72]. The measurement domain was chosen to be the surface region where was 350 mm vertically away from the nozzle. Chronos 1.4 highspeed camera was used to record at the resolution of 1280 × 1024 corresponding to a window of 68 × 55 mm.

The highspeed camera was set to 1057 frames per second and the record time for each RMS velocity was 3 seconds, which yielded 3000 available continuous frames. Image processing and analysis were implemented in PIVLab [73]. The interrogation area was set to 1.7 × 1.7 mm (32 × 32 pixels) with 50% overlap. This resolution followed the "1/4 rule" with the tracer displacement of ~0.03 mm between frames to ensure detection accuracy. The particle image density (number per interrogation area) was about 8, which reached the minimum recommended number of 5 to

achieve close to 100% valid detection probability [74]. Image processing and analysis were implemented in PIVLab [75].

For the surface turbulence calibration measurements, the volumetric flow rate, Q was controlled at 2, 3, 4, 5 GPM. At each flow rate, RMS velocity components in vertical and horizontal directions were measured, then plotted with the corresponding characteristic flow velocity, Q/Dd as shown in Figure 2.2. The results by Sonin et al. [38] were also shown for comparison. The measurement results showed a linear relationship between flow rates and RMS velocity, which indicated isotropic turbulence in the region of interest. Also, the magnitude of turbulence can be easily adjusted by changing the flow rate to create a desired turbulence condition in the upper water surface. Since the mean flow velocity approximates to zero for the isotropic turbulence, the turbulence intensity and root-mean-square velocity both represent the fluctuation strength of the turbulence, which is symbolled by u_{rms} and u'.
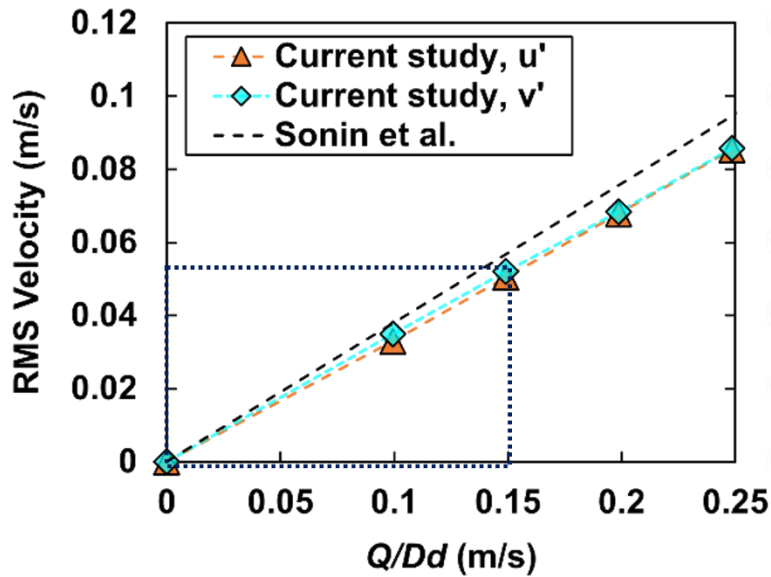
Figure 2. 2: Root-mean-square (RMS) velocity as a function of flowrate. The operating range of current experiments is marked using a dotted rectangle.

The correlation for the RMS value of velocity component in the confined jet configuration is expressed as: $u' = \left(\frac{Q}{Dd}\right) \Phi(Re) \exp(-1.2Z/D)$, where $\Phi(Re)$ is non-dimensional Reynolds number function and becomes a constant when the confined jet is fully developed and isotropic turbulence is formed. In this study, $\Phi(Re) = 17.5$ compared with 21.8 from Sonin et al. [38] and

18.7 from Hu [36]. The system Reynolds number, based on the flow rate through the nozzle and cylinder diameter $(Re_s = (Q/Dd)D/v)$ [38] ranges from 34,000 to 68,000. Mycek et al. [76] reported that turbulent velocities of various natural water resources were in the range of $2 - 60$ cm/s, as shown in Table 1. The velocity values are calculated by the mean flow velocity multiplied by the intensity (%) which yields velocity results representing the turbulence fluctuation intensity. The turbulence in the current study was controlled within the lower side of natural turbulence values.

Table 2. 1: Turbulence strength from different natural open water resources [75] compared with the current study.

Location	Turbulence Strength (cm/s)
Sound of Islay in the Inner Hebrides of Scotland, UK	$24 - 26$ cm/s
4 km west of the Island of Eday in the Orkney Islands. Scotland, UK	$15 - 16.5$ cm/s
Puget Sound. WA. US	$10.9 - 14.8$ cm/s
Easter River in NYC. US	$30 - 69$ cm/s
Strangford Narrows in the northeast corner of island of Ireland. UK	$6 - 31.5$ cm/s
Northern Georgia Strait, British Columbia. CA	$2 - 10$ cm/s
Turbulence in current study	$1.7 - 5.2$ cm/s

2.2.3 Turbulence macroscale

The discussion so far pertains to the turbulent environment alone. Other parameters will arise because of the nucleate boiling experiment interfering with the turbulence. The movement of bubbles generated on the wire can influence the turbulence structure between the liquid phase and gas phase for similar reasons as particles moving through the turbulent gas field reported by Crowe et al. [77]: (1) displacement of the turbulent flow by flow around bubbles; (2) generation of wakes behind bubbles; (3) turbulent energy dissipation to the bubble motion; (4) disturbance of flow because of the bubble interaction; and (5) additional length scale by the bubble movement that

may affect the turbulence dissipation. Considerations of difference between the bubble size and the turbulence integral length scale become important. When the bubble size is large enough to generate wakes that influence the existing turbulent dodecane layer or to influence the turbulence length scale and corresponding energy dissipation, the previous turbulence measurements may be inaccurate for nucleate boiling experiment analysis. Gore and Crowe [78] showed that the particle size needs to be more than $0.1 \times$ of turbulence integral length scale to cause the change of turbulence intensity.

The macroscale of the system (turbulence integral length scale) was defined as [39]:

$$\Lambda = u_{rms} \cdot \tau , \tag{1.4}$$

where τ was a characteristic time,

$$\tau = \int_0^\infty R(t)dt , \tag{1.5}$$

and

$$R(t) = \langle u'(t + t')u'(t') \rangle / u_{rms}^2 , \tag{1.6}$$

was the autocorrelation of the velocity fluctuation, $u' = (u_i - \bar{u})$. The symbol $\langle \cdot \rangle$ represented the ensemble average. Figure 2.3 shows an example of the function $R(t)$ measured with a depth of 2 cm below the surface. The flow rate is 3 GPM, and the corresponding u_{rms} is 0.050 m/s.
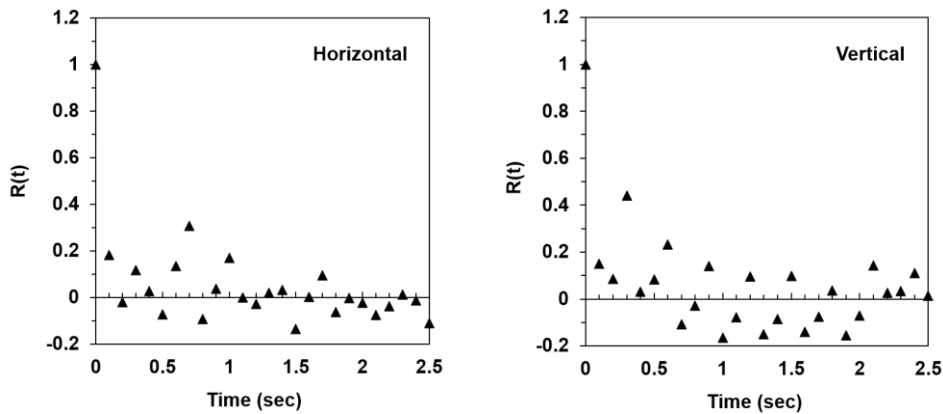
Figure 2. 3: Autocorrelations of the velocity fluctuation at depth of 2 cm below the surface. u_{rms} = 0.050 m/s at flow rate of 3 GPM.

Table 2 summarizes the results for the turbulence integral length scale. The average length scale or the turbulence eddy size at the measurement location is about 38 mm ($0.38D$). Brown et al. [39] measured the integral length scale near the surface at a distance of $H/D = 3.6$ ($H/D = 3.3$ in this study). They reported that the length scale was approximated independent of Reynolds number, isotropic in direction and given by $\Lambda \cong 0.24D$, which indicates the length scale in this study is an appropriate value. Because the measurement elevation is lower meaning the distance between the surface and nozzle increases, and the dissipation of turbulence increases which causes a smaller length scale of the eddies.

Table 2. 2: PIV measurements of integral length scale at a depth of 2 cm below the surface. Operating flow rates are 2, 3, and 4 GPM with corresponding RMS velocities ranging from 0.033 – 0.068 m/s.

RMS Velocity (m/s)	Characteristic time τ (sec)	Integral length scale Λ (m)
Horizontal components, u_{rms}		
0.033	1.58	0.0411
0.050	1.08	0.0408
0.068	0.58	0.0331
Vertical components, v_{rms}		
0.035	1.54	0.0413
0.052	0.96	0.0360
0.068	0.60	0.0353
		Average: $\Lambda = 0.038$ m $\cong 0.38\ D$

2.3 Experimental results

2.3.1 Subcooled nucleate boiling on a wire without turbulence

Figure 2.4 shows the nucleate boiling curve of the no turbulence (baseline) experiment. Along with the observations from a high-speed camera, four distinctive stages of bubble behaviors are observed, as shown in Figure 2.5. For the no turbulence case, the onset of nucleate boiling (ONB) starts at a heat flux around 0.3×10^3 kW/m^2, and critical heat flux (CHF) is observed at 1.8×10^3

31

kW/m^2. Before ONB, no bubbles are observed on the wire, meaning the heat transfer mechanism is by convection, and only sensible energy is involved. Once ONB is reached, bubble generation is observed. The evaporation of the surrounding liquid takes away heat as latent energy from the hot wire surface, resulting in a noticeable heat transfer coefficient increase in the slope (Fig. 2.4), which indicates the heat transfer improvement in stages I and II. The heat flux keeps increasing gradually before and after CHF, while the wire experiences a jump in temperature after CHF. After this point, the nucleate boiling curve enters the film boiling stage, where the bubble generation is so intense that a film of vapor is observed to wrap over the entire wire. Because of the low heat conductivity of gas vapor, more heat is trapped within the wire, and shortly leading to the wire collapsing and glowing red. A structural breakdown of the wire is observed soon after the film boiling stage is reached, which is referred to as burnout.
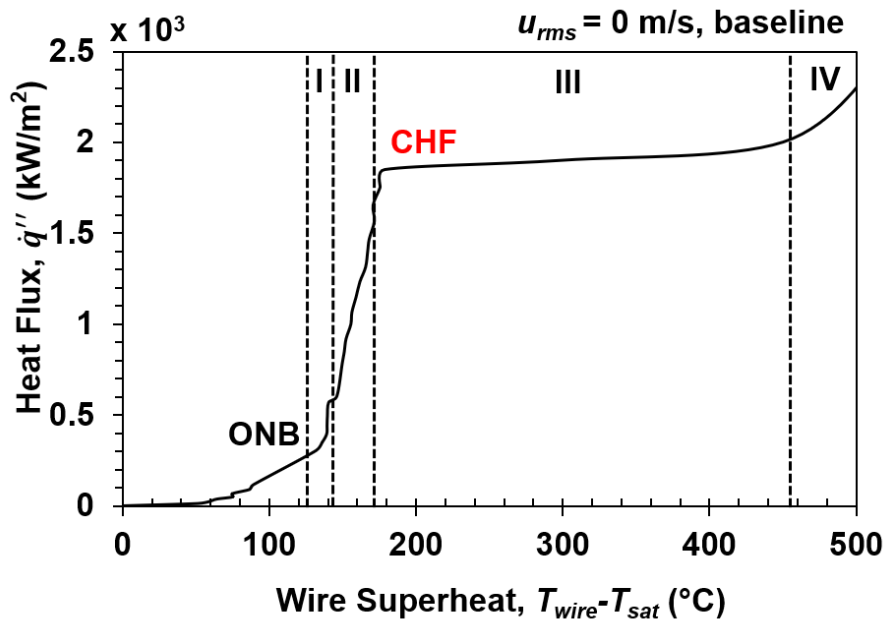
Figure 2. 4: Nucleate boiling curve of $u_{rms} = 0$ m/s (baseline) case. ONB is observed at around 0.3×10^3 kW/m^2, and CHF is observed at around 1.8×10^3 kW/m^2. Labels I to IV on the nucleate boiling curve represent four stages during the subcooled boiling process.

Figure 2.5a-d shows the four stages of bubble behaviors in detail. The differences in heat transfer between each stage are well-explained by bubble behaviors. The propulsion mechanism of the bubble is by Marangoni stresses [79,80]: when a bubble moves, a mixing zone is generated behind the bubble, where cool liquid enters and affects the thermal boundary layer. With bubble front

thermal boundary intact, a temperature difference between the front and back of the bubble is created, which induces a surface tension difference that drives the bubble movement. The Marangoni effect can also be referred as the thermocapillary effect when the surface tension is induced by temperature difference [49].

Figure 2.5a shows, in Stage I where ONB is reached, a single small bubble is observed to sweep smoothly along the whole wire at a nearly constant speed. The bubble only changes sweeping direction when it contacts the copper electrodes at two ends of the wire. A curvy thermal plume attaches to the top of the bubble because of the thermocapillary convection driving hot fluid upwards. With heat flux increasing, Figure 2.5b shows Stage II of bubble bouncing and merging. In this stage, bubbles move randomly on the wire. Upon contact, bubbles either bounce backward against each other or merge into a single large one. Bubbles continuously gain in size eventually reaching a turning condition where buoyancy force overcomes the tension stress on the wire and departures from the wire. Also, the thermal plume becomes irregulate in shape, because of the interaction between thermal plumes from multiple bubbles and the wire, thus indicating the thermal boundary layer of thickness equal to or greater than bubble diameter has developed. Then in Stage III shown in Figure 2.5c, the heat flux value approaches CHF, where the bubbles no longer move along the wire. Instead, the bubbles stay clustered in position, and merge with adjacent bubbles, growing in size until they depart upwards. The bubbles hanging on the wire are larger (diameters of 0.5 – 1 mm) compared with previous stages (0.3 – 0.5 mm). This is because the temperature between the upper and lower bottom of the bubble now becomes significant enough to induce stronger Marangoni stress as the bubble upper interface reaching further into the cooler liquid region. The stress holds the bubble from detaching, so it requires a larger volume to create sufficient buoyant force to overcome this stress. Moreover, huge amounts of fast-moving tiny bubbles (diameters of 0.05 – 0.1 mm) are generated on the wire, forming a nearly constant force on the two sides of the large hanging bubbles. The tiny bubbles continuously acting on the larger ones and force large bubbles to stay in position. The high velocity of tiny bubbles is observed because of the strong Marangoni stress across the horizontal direction of tiny bubbles. The thermal plume in this stage is highly turbulent such that the light distortion noticeably affects the micro high-speed recording. Finally, in Stage IV shown by Figure 2.5d, the nucleate boiling changes into the film boiling region. The wire temperature suddenly increases to 280 °C, causing the dodecane

fuel to evaporate intensely enough to form bubble wrapping around the wire. The high voltage and temperature bend the wire, and the wire starts to glow red. The bubble departure is so intense that large bubble columns are observed lining up along the wire. Shortly burnout is observed and the wire breaks terminating the experiment.
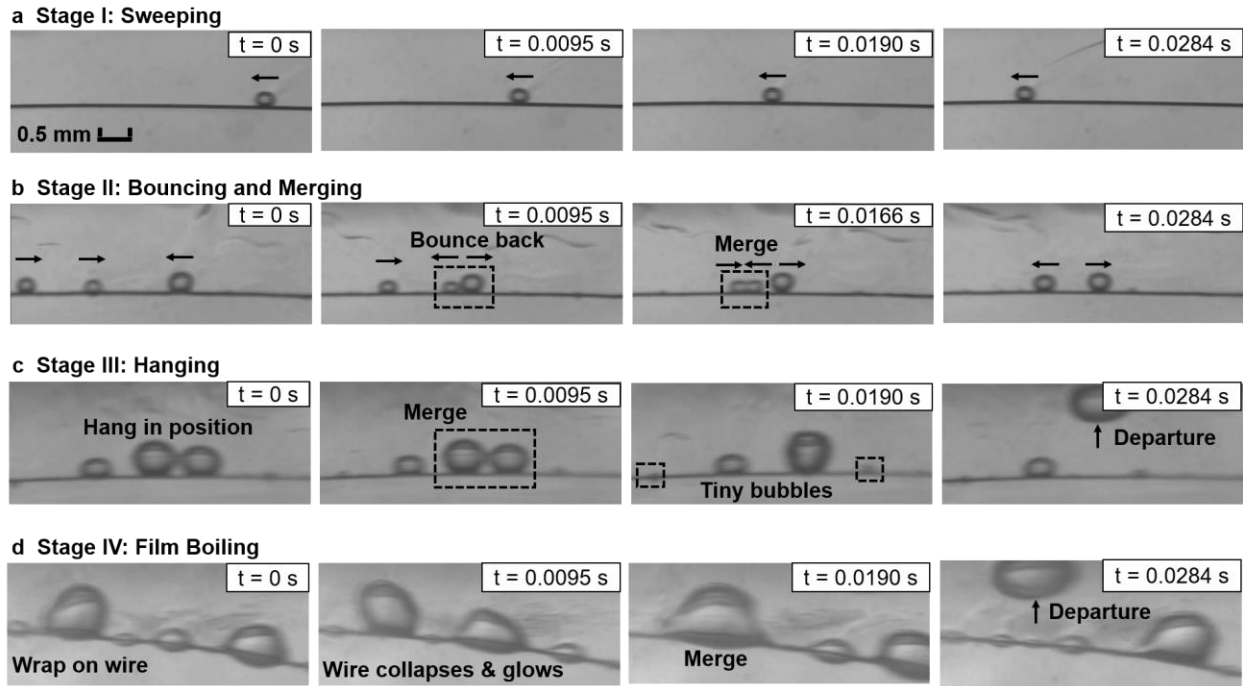
Figure 2. 5: Four stages of bubble behaviors with increasing heat flux without turbulence. (a) Stage I: single small bubble sweeping smoothly at a constant speed; (b) Stage II: multiple small bubbles bouncing and merging; (c) Stage III: a large number of tiny bubbles forming large bubbles by coalescing; (d) Stage IV: vapor film wrapping around the wire leading to burnout.

The influence of bubble movement on the generated turbulence microscale is negligible in this study. Compared with the turbulence integral length scale of about 38 mm, the observed bubble size is 10 times smaller, implying that the influence of bubble movement on the measured turbulence is negligible. The wire has a diameter of 0.127 mm which is much smaller than the integral length scale. Therefore, the measured turbulence results stay valid in nucleate boiling experiment analysis. Duchesne et al. [50] reported the influence of wire diameter on subcooled nucleate boiling experiments in still liquid bath: (1) with the increase of wire diameter, the heat flux required to reach each boiling stage is increased; (2) when the wire is thicker than 0.3 mm in diameter, the bubble film in Stage IV becomes more uniform in thickness.

2.3.2 Subcooled nucleate boiling on a wire with turbulence

Figure 2. 6 shows the variation of heat flux, $\dot{q}''$ as a function of wire superheat temperature with different turbulence levels. Overall, the enhancement of heat transfer is achieved with an increase in turbulence strength. In the convection dominating region (before ONB), it is observed that the slope increases with u_{rms}. This is because of the convective cooling effect by turbulence, which increases the convective heat transfer coefficient. Both ONB and CHF increase to higher values with larger u_{rms}.
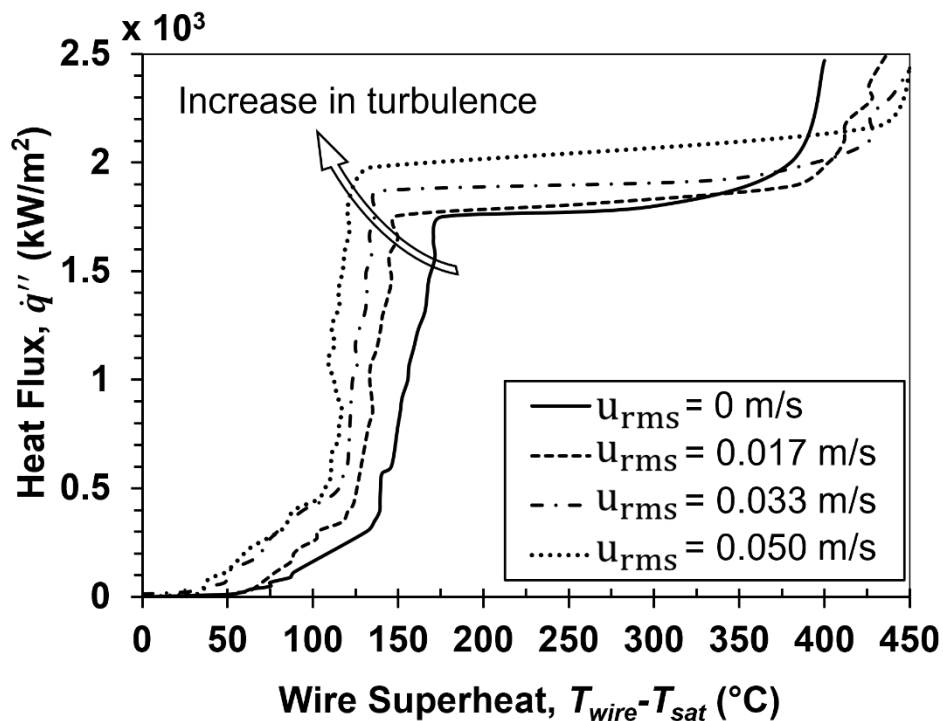
Figure 2. 6: Nucleate boiling curves under different turbulence strengths. Enhancement of heat transfer is achieved with stronger turbulence, resulting in both ONB and CHF raising in value. is achieved with stronger turbulence, resulting in both ONB and CHF raising in value.

CHF values are plotted in Figure 2.7, along with bubble departure frequency (BDF) as a function of u_{rms}. The heat flux on the wire surface is constant at $\dot{q}'' = 0.6 \times 10^3 \ kW/m^2$ under each u_{rms}, where just surpassing ONB so that bubble departure is not too chaotic to be measured. Figure 2.7 shows that BDF increases nonlinearly while CHF increases nearly in a linear fashion as a function of u_{rms}. The bubble departure frequency (BDF) is determined by the number of nucleation sites

35

and fluctuating eddies bombarding the surface of the bubbles induce oscillations of the bubbles. The number of nucleation sites increases as heat flux increases [66]. Since the heat fluxes were set to the same value for all the BDF measurements, the energy level of the arriving eddy plays the main role that causes the BDF to increase with the turbulence. The bubbles are affected by the eddies such that once eddies of sufficiently high energy and frequency arrive, the bubbles will oscillate and might eventually lift off [81]. The arrival frequency of eddies, f_e is determined by the reciprocal of the turbulence characteristic time, τ. In stronger turbulence cases, the turbulence characteristic time decreases, causing larger eddy arrival frequency (Table 2). With increases on both eddy energy and arrival frequency, the bubble departure frequency is therefore increased.
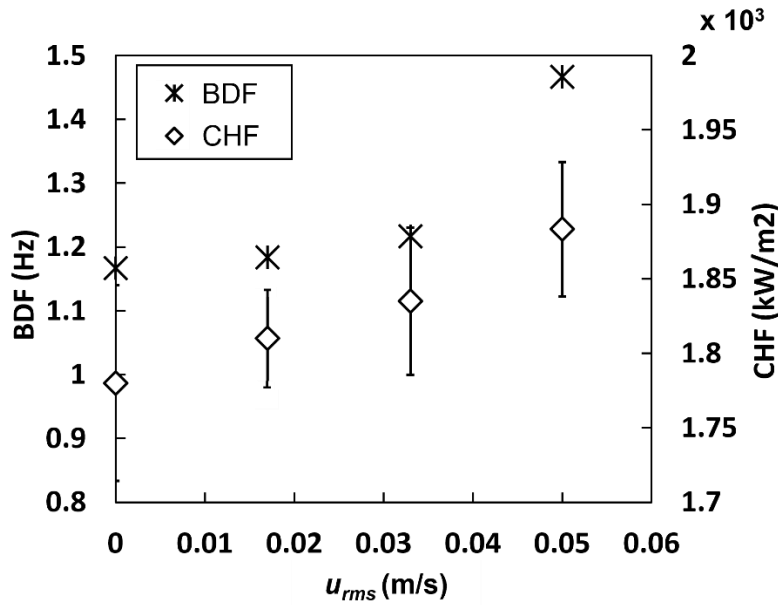
Figure 2. 7: Bubble departure frequency (BDF) and critical heat flux (CHF) as a function of turbulence strength indicated by u_{rms}. CHF increases linearly with u_{rms}. BDF increases exponentially with urms. Heat flux, $\dot{q}'' = 0.6 \times 10^3$ kW/m^2 for all cases where BDF was measured.

The bubble departure size, D_B as a function of u_{rms} is shown in Figure 2.8, which is measured based on an averaged value of 100 successive bubbles at departure under each turbulence condition. The heat flux is set at $\dot{q}'' = 0.6 \times 10^3$ kW/m^2, which is identical to BDF and CHF measurements. The bubble size shows a nonlinear decline with u_{rms}. The smaller departure bubble volume means a smaller buoyant force is required to overcome the surface stress that holds the bubble to the wire.
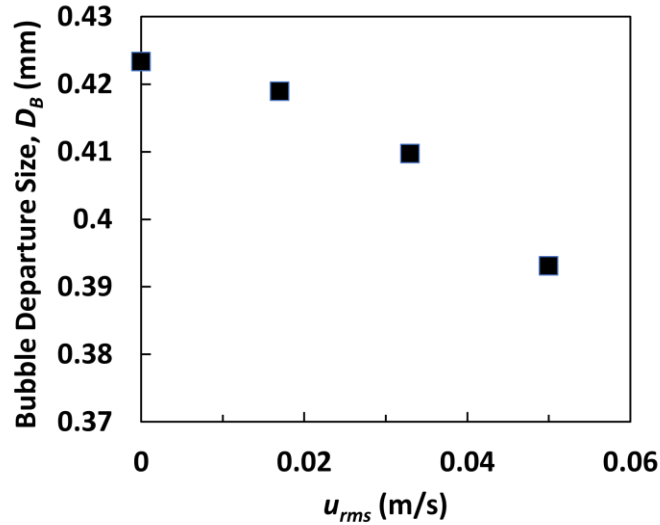
Figure 2. 8: Bubble departure size as a function of turbulence velocity component u_rms with wire surface heat flux, $\dot{q}'' = 0.6 \times 10^3$ kW/m². The bubble size at departure decreases with the increase of u_rms, meaning the buoyance force to overcome Marangoni stress is decreasing. The standard variation in reported measurements is 1.7%.

The force balance analysis and the surrounding thermocapillary convection of a single bubble are shown in Figure 2.9. The horizontal component of the Marangoni force, $F_{ma,x}$ propels the bubble sweeping along the wire and its vertical component, $F_{ma,y}$ prevents the bubble from rising against the buoyancy force. The thermocapillary convection is observed around the bubble side region, which circulates the hot liquid from the wire surface micro-layer to the colder upper liquid region around the bubble. With turbulent flow impacts on the bubble and its vicinity, the additional turbulent drag force facilitates the bubble's instability. However, Koumoutsos et al. [59] showed the drag force was considerably smaller than the buoyant and surface forces using a force balance on the bubble at the instant of departure in low flow conditions. Therefore, the change of the Marangoni force in the vertical direction, $F_{ma,y}$ is postulated to be the reason that causes the reduction in the bubble departure size with turbulence. $F_{ma,y}$ is reduced by the combined effects of increasing condensation rate on the dodecane bubble top region and the enhanced thermocapillary convection.
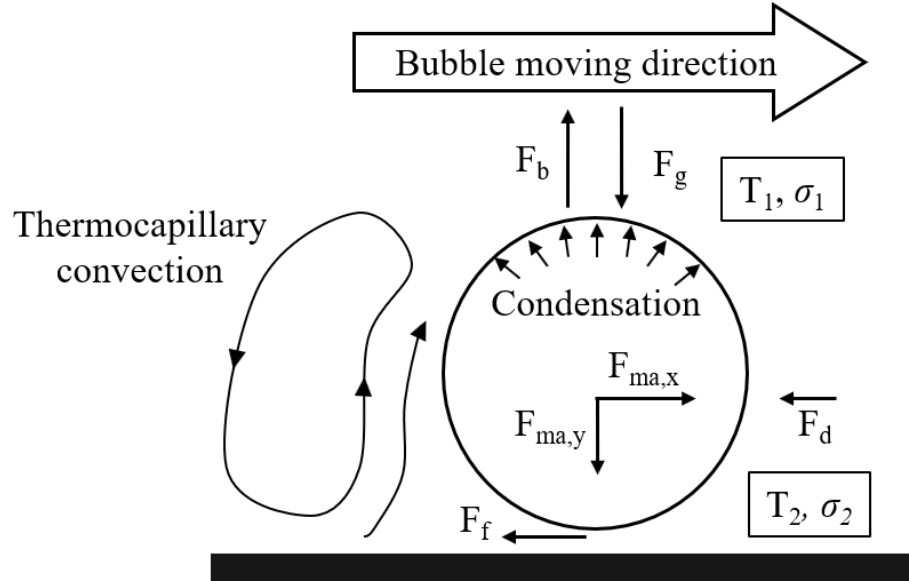
Figure 2. 9: Force balance on a bubble attaching to the wire in subcooled nucleate pool boiling (F_b = Buoyancy force, F_g = Gravitational force, F_{ma} = Marangoni force, F_f = Friction force, F_d = Drag force). T is liquid temperature, and σ is liquid surface tension at T. Condensation occurs at the bubble top interface. Thermocapillary convection is formed around the bubble because of the temperature gradient.

The Marangoni force, $F_{ma,y}$ keeping the bubble attached to the wire is because of the surface tension difference ($\Delta\sigma = \sigma_1 - \sigma_2$). Marek et al. [82] showed the non-condensed gas would accumulate at the upper interface of the bubble and increase the diffusion resistance by impeding the motion of vapor. With turbulent eddies around the bubble interface, the gas condensation rate increases [38,39], which drives the vapor motion through the upper bubble wall and dissipates heat into this vapor-liquid interface. As a result, the dodecane surface tension at the top bubble region, σ_1 drops with the increase of temperature, T_1 [83], which eventually reduces the Marangoni force, $F_{ma,y}$ and facilitates the departure of bubbles at smaller sizes. Additionally, the turbulence intensifies the thermocapillary convection because of the mixing effect, pumping more hot liquid towards the bubble upper region that further reduces the temperature gradient ($\Delta T = T_2 - T_1$), so is the surface tension difference, $\Delta\sigma$. Simulations have shown that temperatures at the liquid layer adjacent to the wire where the bubble sweeps are much higher than the bulk liquid region which is further away from the wire [84]. The pumping effect by the thermocapillary convection dominates over the turbulence cooling effect on T_1 at this microlayer. Therefore, $F_{ma,y}$ is reduced by the two collective effects of condensation and thermocapillary convection. Also, the increased

eddy arrival frequency might cause perturbance on the heating wire and bubbles, increasing the instability and shaking the bubble off the wire.

Figure 2.10a-c shows the bubble behaviors of Stage I to Stage III under turbulence strength $u_{rms} =$ 0.050 m/s. The film boiling Stage IV is neglected because no evident difference in bubble behaviors is, and this region has passed CHF where burnout will shortly occur leading to structural failure. $u_{rms} = 0.050$ m/s is chosen because of its distinctive differences from the no turbulence case.

Figure 2.10a shows that in Stage I, the single bubble changes direction occasionally instead of sweeping smoothly along the whole wire as observed in the no turbulence case shown in Figure 5a. This may be because of interaction with intermittent turbulent eddies. The thermal plume attaching to the top of the bubble disappears under the mixing effect in a turbulence environment, indicating the breakup of the thermal boundary layer around the heating wire. The mixing causes an enhancement in the heat transfer coefficient induced by forced convection, which agrees with the nucleate boiling curves shown in Figure 2.6.

Figure 2.10b shows in Stage II, bubbles bounce back or merge into each other upon contact, which is similar to Stage I. However, bubble movements are observed to be sensitive to turbulence. The temperature-induced Marangoni stress and turbulence compete against each other, and the bubble propulsion mechanism is more likely dominated by the turbulent flow other than Marangoni stress. Bubbles along the wire change sweeping direction as the turbulent flow changes direction. The Marangoni stress is not strong enough to hold against the turbulent flow, and all bubbles are observed to move in the same direction even after bouncing back and merging.

Figure 2.10c shows in Stage III, the large bubble cluster no longer stays in position despite the tiny bubbles are still constantly pushing against the large bubbles on the two sides. The cluster of hanging bubbles is carried by the turbulent flow, moving towards the same direction. This phenomenon keeps the wire surface wetted with a surrounding liquid, to some extent manage to avoid over-heating at those nucleation sites where large bubbles hang in no turbulence case. When large bubbles staying stationary at nucleation sites, heat tends to build up rapidly without mixing with the cool surrounding liquid. The contacting area at the bubble bottom against the wire is a

very thin layer of liquid fuel and the bubble itself is low-thermal conductivity vapor, which traps heat within the wire and causes heat flux to reach CHF. The bubble behaviors in a turbulent environment agree with the nucleate boiling curves result, that the heat transfers in both convective and nucleate boiling regions are improved, and CHF occurs at higher heat flux.
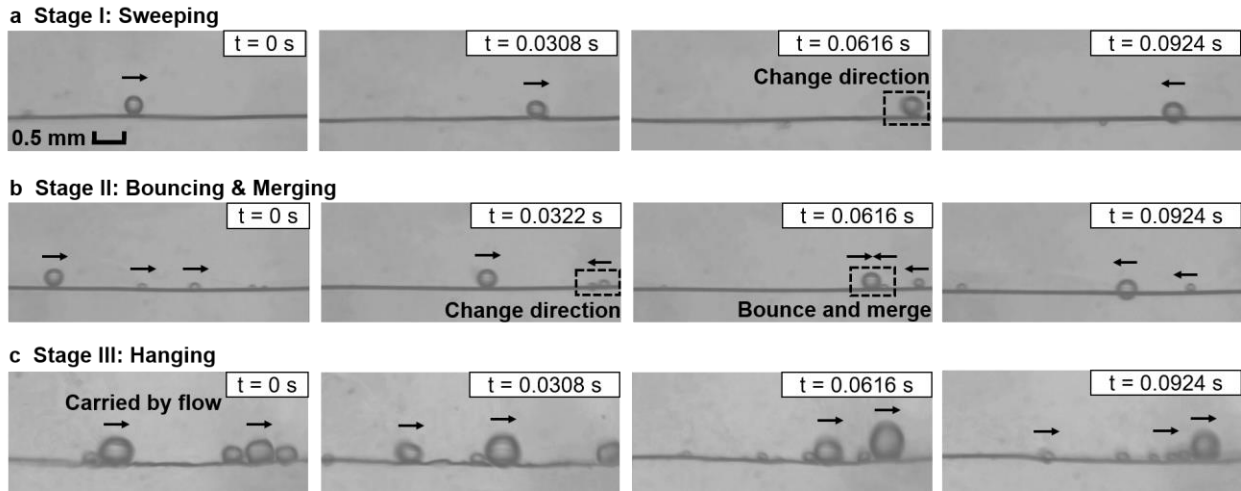
Figure 2. 10: Bubble behaviors with increment in heat flux on the wire surface under $u_{rms} =$ 0.050 m/s. (a) Stage I: single bubble changing direction occasionally; (b) Stage II: turbulent flow dominating as bubble propulsion mechanism; (c) Stage III: large bubble cluster carried by the turbulent flow.

Figure 2.11 shows the schematics of bubble movements and plume shapes at different heat fluxes corresponding to stage I, II, and III under no turbulence case and turbulence case. Schematics are drawn by closely observing the high-speed videos in experiments without and with turbulence. In no turbulence case, bubbles only change direction when interacting with another bubble, otherwise, there are no other forces to steer the bubbles. While in turbulence cases, the bubbles change direction randomly. Two sizes of bubbles are observed on the wire: tiny bubbles with diameters of 0.05 – 0.1 mm sweeping rapidly along the wire; large bubbles with diameters of 0.5 – 1 mm moving at a much slower speed. As the strength of the turbulence is increased, the bubble movement along the wire and consequent direction change become more chaotic.

The thermal plumes in the no turbulence case are uniform in profile and longer compared to the turbulence case as shown in Figure 2.11. Since the turbulence breaks the thermal boundary layers near the wire region, the plume intensity is observed to be weaker than the no turbulence case. As

a result of the turbulent mixing effect, the instability of bubbles increases, which causes plumes to be irregular and fluctuating. The turbulent mixing effect dissipates heat downwards to the sub-water layer, so the plume under the wire is more obvious because of the larger temperature difference between the wire and the lower dodecane layer.
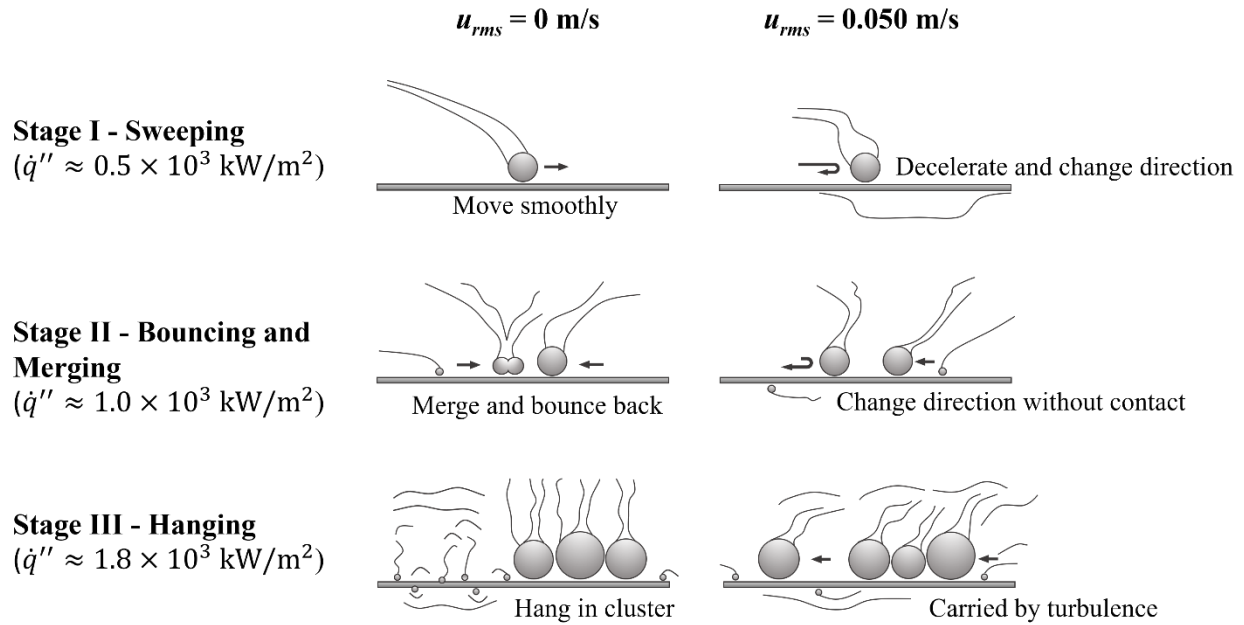
Figure 2. 11: Schematics of bubble movements and plume shapes at heat flux, $\dot{q}''(0.5 \times 10^3 \text{ kW/m}^2, 1.0 \times 10^3 \text{ kW/m}^2, \text{ and } 1.8 \times 10^3 \text{ kW/m}^2)$) in Stages I – III during subcooled nucleate boiling experiments under no turbulence case (u_{rms} = 0 m/s) and turbulence case (u_{rms} = 0.050 m/s).

Nucleate boiling is highly sensitive to the presence of turbulence. Even the weakest turbulence like those found in natural water resources can alter the bubble behavior and corresponding heat flux. The current study only operates at the range of low turbulence strength, because the measurement difficulties and uncertainties of nucleate boiling experiments using such a thin wire are very challenging. Future work with stronger turbulence strength is needed to be studied.

2.4 Conclusions

The heat transfer mechanism and bubble behaviors of subcooled nucleate pool boiling using 0.127 mm diameter nichrome wire are experimentally studied in a 4 cm thick isotropic turbulent

dodecane layer, which is made by a confined jet system. The heat transfer is closely interrelated with bubble behaviors, and the four stages of bubble behaviors characterize different corresponding regions of the nucleate boiling curve. They are, respectively: sweeping stage, bouncing and merging stage, hanging stage, and film boiling stage. The heat transfer shows improvement under turbulent cases. Bubble departure frequency (BDF) and critical heat flux (CHF) increase as a function of turbulence strength represented by root-mean-square (RMS) velocity. Bubble departure size decreases as a function of turbulence RMS velocity. The bubble propulsion mechanism is dominated by two competing factors: Marangoni force and thermocapillary convection. Both are subject to the impact of turbulent eddies, which facilitates the bubble lift-off, and improves the heat transfer performance compared with the baseline case.

Chapter 3: Crude oil slick burning

3.1 Introduction

The burning of a liquid fuel layer floating on water has been studied extensively because of the interest in fuel spill accident clean-up technics in open waters, which is called *in-situ* burning (ISB). This cleaning method requires collecting oil slick using a "fire boom" and igniting the collected oil as a pool fire [2,3,17]. ISB related studies have gained increasing attention because of their relatively low cost and easy applicability to remove a large amount of oil on a wide area [4].

The investigation on the burning of floating oil on water is theoretically based on the understanding of pool fires, where earlier effort has been devoted to [6,16,85]. The attention to the fuel burning upon water comes later due to the complexity of the burning configuration and increasing demand for oil spill clean-up approaching the millennium. The pioneer studies of this specific burning condition mostly relate to boilover phenomena [18,86] and ignition [9,87–89], where thin fuel layer boilover becomes an important concern. The occurrence of boilover positively affects the burning rate because the on-set of boiling nucleation at the fuel/water interface results in the ejection of oil droplets into the flaming zone [19]. The boilover happens after a long period of quiescent burning, and the time to the onset of boilover correlates well with the thermal penetration time to reach the water layer super-heated condition [20]. The effect of fuel thickness, pool diameter, and fuel boiling point has also been studied by Garo et al. [19,20,90]. They observe that the burning rate does not depend on the initial fuel layer thickness when it is thicker than 10 mm and that decreases for thinner layers. The self-sustain burning of oil is no longer possible with a typical minimum thickness of 0.5 mm. The burning behavior matches the investigations by Alramadhan et al. [14] and Koseki et al. [91] that only a thick fuel layer is able to form a sufficient hot zone for explosive boilover to occur. Based on those preceding studies, Torero et al. [21] completes a simple heat conduction model to describe the pre-boilover ignition and burning rate of crude oil. They apply a combined thermal diffusivity to account for the different thermal properties of oil and water layers, then use it to obtain an analytical solution for the burning rate under certain pool diameter and initial fuel thickness.

While the real-world application of ISB demands a further reach into more complex burning environments, the previous bench-scale studies have been well-applied to serve such needs. For example, Shi et al. [92] and Farahani et al. [93] conduct the crude oil pool fire experiments with an adjacent ice block, where the change of ice cavity geometry and heat sink effect on the burning behavior is studied. Gelderen et al. [94] construct the Crude Oil Flammability Apparatus (COFA) which is designed with a fuel slick burning area surrounded by a large body of water. This is to simulate a burning oil/water interface that is comparable to large-scale burns. The way to experimentally set up the fuel/ambient boundary is the most important because the heat loss across that interface can largely affect the burning of the fuel layer. There are only a few studies that address the dynamic nature of the ocean surface [17,95], and the most used method is to conduct the oil layer burning experiments in a wave tank [88,96]. However, the wave tank is costly to operate and the wave profile is difficult to be controlled to the precision for burning rate modeling. There is no bench-scale experimental platform dedicated to simulate dynamic ocean conditions in a fine-controlled fashion. Studies on turbulence in natural water resources [34] indicate that the water surface shows turbulent characteristics because of the wind-driven mechanism, under-surface current, and the confinement of geographic terrains. Large eddies gradually deform into smaller eddies and eventually dissipate in the environment as heat [33]. A turbulence water surface can represent the ocean surface dynamic and can be accurate to simulate the fuel/water interface during the burning process. While the complexity of the turbulence might easily defy the experiment analysis, a structural simplified type of turbulence is created in lab-scale to deal with this issue, which is referred to as isotropic turbulence. The water surface of isotropic turbulence is an ideal experimental platform to analyze the role of turbulence on oil slick pool fires. The current isotropic turbulence generation using a confined jet is inspired by the earlier works of Sonin et al. [38], where vapor condensation onto a turbulent liquid surface was investigated. They reported that the condensation rate is proportional to the RMS turbulence velocity at the surface. Using the similar experimental setup, Morse et al. [37] reported that the evaporation rate of the liquified natural gas has strong dependence on the turbulent liquid surface. However, the previous works were conducted under ambient temperature where the liquid surface temperature was much lower compared to a burning pool surface. From the standpoint of surface equilibrium, the evaporation rate of the floating fuel is dominantly affected by the burning condition when the pool fire is introduced. Therefore, the evaporation rate changes due to surface turbulence is neglected in this

study and only subject to changes due to the burning characteristics. The turbulence is only considered to alter the heat transfer mechanisms in the liquid layers which eventually causes impacts on the fuel burning rate.

In this study, the oil slick elevation is maintained at 3.5 times the confinement tube diameter, and the turbulence root-mean-square (RMS) velocities in both vertical and horizontal directions are measured and compared with the reported turbulence velocity from the open water resources. Simple 1-D heat conduction models are used to describe the fuel layer temperature profile and to obtain the convection boundary condition under different surface RMS velocities. The heat release rate by the flame is determined from an existing correlation for pool fires [97–99], and the net heat flux feedback per unit area to the fuel represents a small fraction (χ) of the total flame heat release rate. This fraction is found using energy balance at the fuel surface.

3.2 Experimental Setup

Figure 3.1 shows the oil slick burning facility with the turbulence generation system. The oil slick burning experiments were performed in a cylindrical Pyrex glass tube with an inner diameter $D = 100$ mm, and a height that maintains the water surface at $H = 350$ mm from the nozzle (Fig. 3.1). The glass tube was then placed inside a 180 mm x 180 mm rectangular acrylic tank filled with fresh water, which mitigated the heat transfer issues in a small-scale burning tank [94]. A cylindrical jet nozzle with diameter $d = 12.7$ mm was located at the center bottom of the cylindrical tube, from which a centrifugal pump drove water jet upwards. Two suction ports were placed symmetrically beside the jet nozzle to feed water into the pump and ensure the jet profile was symmetric. A turbine flowmeter and a control valve were installed in the pipeline controlled the flow rate. Particle Image Velocimetry (PIV) was used to measure the turbulence velocity near the surface. The turbulence generation platform was inherited from the works by Chang et al. [100] and PIV measurement accuracy was improved by using more data sets to 3000 for each RMS velocity output.
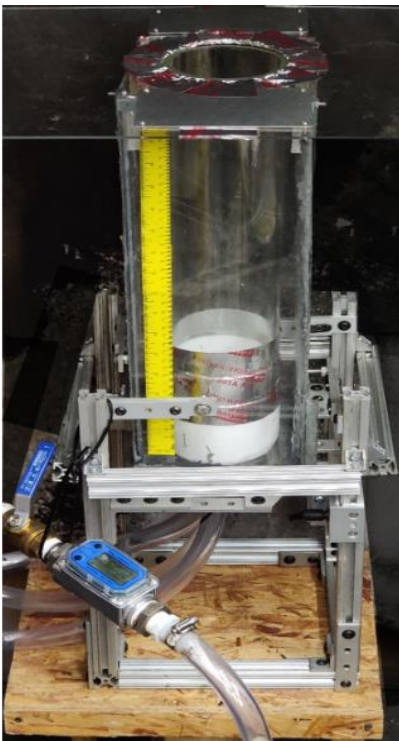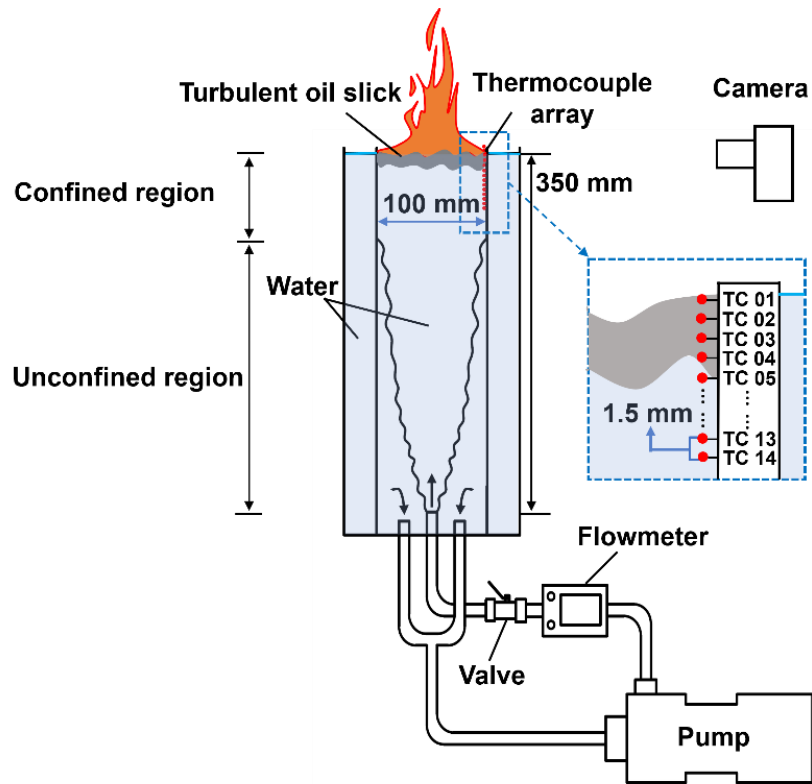
Figure 3. 1: Schematic and photograph of the experimental setup. A water jet is directed upwards, generating isotropic turbulence at the water surface in the confined region. 5 mm

thick crude oil poured on top. An array of 14 thermocouples spacing at 1.5 mm measuring a total depth of 21 mm.

5 mm thick Alaska North Slope (ANS) crude oil slick was used in all experiments in this study. As shown in Fig. 3.1, a thermocouple array with 14 numbers of K-type 36-gauge thermocouples attached to the inner cylindrical tube was used to measure the temperature profile in the oil and water layers. Each thermocouple had a spacing of 1.5 mm. TC 01 was positioned at the surface of the crude oil layer, achieving a total measurement depth was 21 mm. The thermocouples were set to a data acquisition frequency of 1 Hz and each measurement was averaged within a 10-second interval for modeling analysis. A butane torch was used to ignite the oil slick. The mass of initial oil slick and burnt residue were weighed for a global average mass loss rate (MLR). The oil residue was collected by a 3M petroleum sorbent pad. The average MLR was calculated by the difference of oil slick weight divided by recorded burning duration. Each experiment was performed three times.

To determine the flame height, a video camera was positioned on a tripod facing the flame horizontally, with a light-absorbing blackboard placed in the background. A tape ruler on the water tank side wall was used as a scale reference. Videos of flames were converted to pictures with an interval of 1 second. Finally, to reduce the data fluctuation caused by flame puffing, the flame height value of every 10 data points was averaged, resulting in plotted data of 10 seconds intervals.

The operation turbulence intensities for burning experiments are chosen as $u' = 0.017, 0.025,$ and 0.033 m/s (corresponding to flow rates of 1, 1.5, and 2 GPM). Figure 3.2 shows the snapshots of the maximum vertical variation in height, Δh of 5 mm crude oil slick sitting on the water surface under operation turbulence intensity for burning experiments. Morse et al. [37] used the surface height variance as a measure of the turbulence intensity in a confined jet cylindrical tank. They estimated the magnitude of velocity fluctuation by balancing kinetic and potential energy change using: $(u')^2 = 2g\sqrt{\Delta h^2}$, where g is the gravitational acceleration. The u' measured by PIV in this study match well with the energy balance equation based on the observed Δh.
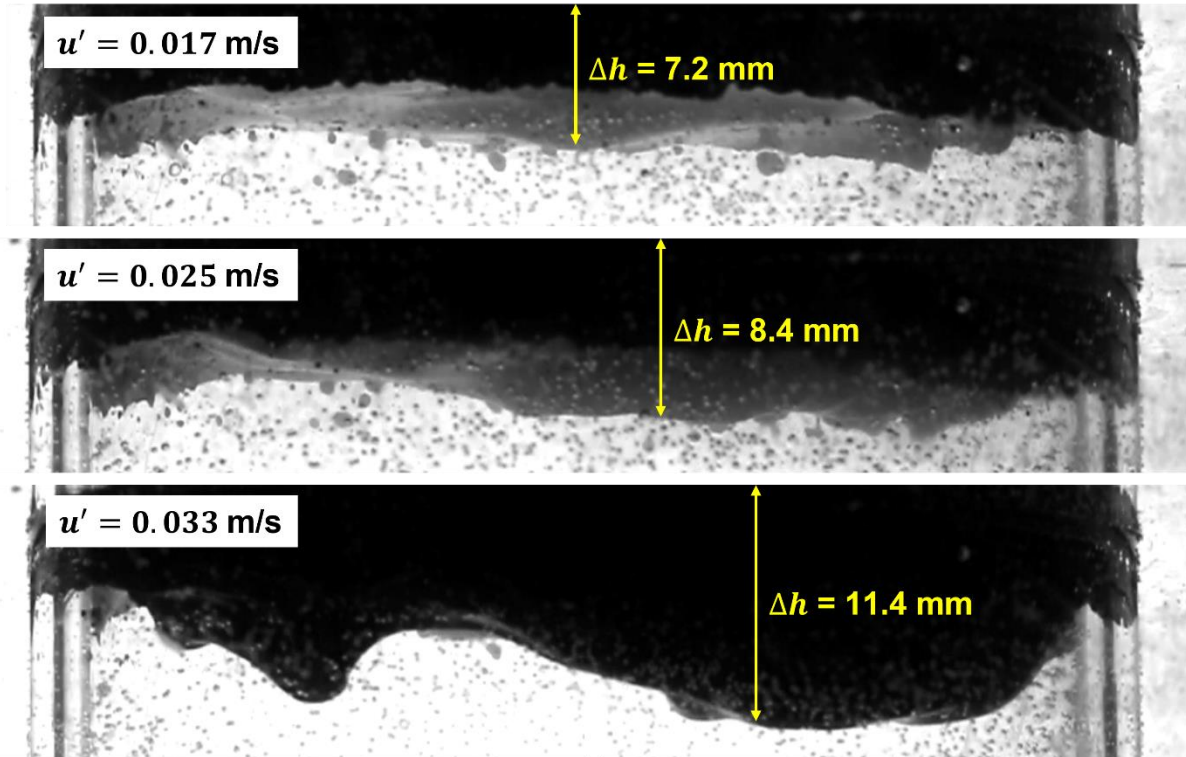
Figure 3. 2: Snapshots of oil slick under operational u'. Δh is the maximum vertical variation, which indicates the magnitude of fluctuation.

Turbulent velocities in various natural water resources have been measured in the range of 0.02 – 0.60 m/s [76] (Table 2.1). To ensure the data accuracy and feasibility of the experiments, the turbulence in the current study is controlled at the range of 0 – 0.033 m/s, which sits at the lower side of ocean turbulence intensity.

3.3 Experimental Results

3.3.1 Mass loss rate

Figure 3.3 shows the crude oil burning average MLR for the no turbulence baseline and 3 turbulent cases. For the baseline case, the oil slick burns in a quiescent surface condition without any disturbance from the water sublayer. The oil slick surface remains stationary for the most burning time until reaching boilover towards the end of the experiment (Fig. 3.4). Compared with the inactiveness of the water sublayer, The turbulent water layer removes heat from the oil slick much

more quickly creating a stronger heat sink effect. This results in a high-level global average mass consumption rate of 4.8 g/min for the baseline case. At the turbulent intensity of 0.017 m/s, the surface only has a mild fluctuation, while the corresponding MLR decreases by 20% from the baseline case to 4.0 g/min. This indicates even with weak turbulence, the dynamic water sublayer can cause a notable negative impact on the oil burning rate. As shown in Figure 3.3, when increasing the turbulence level to 0.033 m/s, the MLR decreases further to 34.2% at 3.6 g/min compared with the baseline.
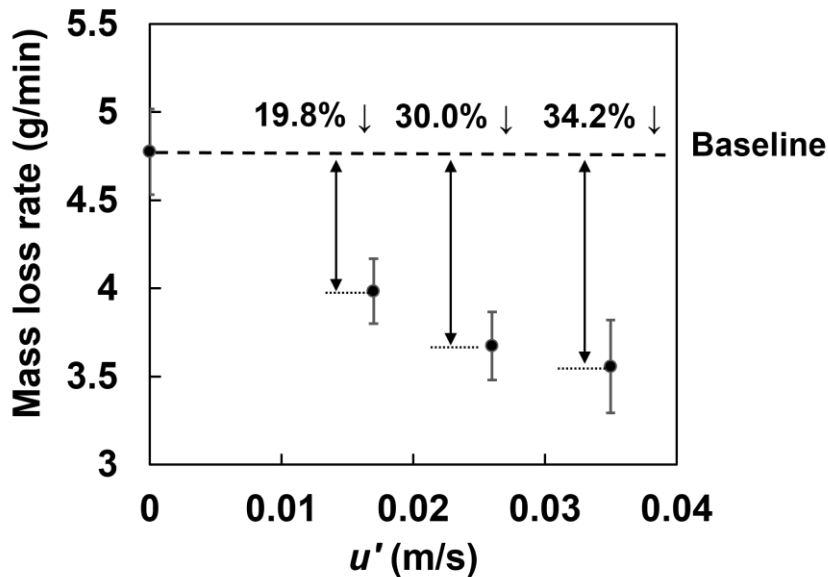
Figure 3. 3: Average MLR as a function of u'. The baseline case has an MLR of 4.8 g/min. $u' = 0.017$ m/s, MLR has a 19.8% decrease from baseline case; $u' = 0.025$ m/s, MLR has a 30% decrease from baseline case; $u' = 0.033$ m/s, MLR has a 34.2% decrease from the baseline case. The error bars represent the standard deviation based on experimental data from three repeated experiments.

3.3.2 Flame height and boilover

Figure 3.4 shows the flame heights recorded during the crude oil burning experiments under each turbulence intensity condition. The flame height overall matches decreasing trend as the MLR as the turbulence goes more intensive. The increased heat loss of the burning oil slick due to the cooling water mixing makes it difficult for the oil surface to sustain the baseline evaporation rate, which causes a reduction in the amount of combustible volatile reaching into the flame zone.

Therefore, the flame height becomes lower as the turbulence level is tuned up. The quenching stages after the end of boilover are observed to have different behaviors between baseline and turbulence cases. In the baseline case, the oil slick can sustain burning with a low flame height of approximately 12 cm following the boilover, while the oil slick burning stops almost instantly after the boilover (Fig. 3.4). The typical value of minimum oil spill thickness for self-sustained burning is of the order of 0.5 mm [19]. In turbulent conditions, it requires a larger critical thickness for self-sustain burning because of the enhanced heat loss through the oil layer.
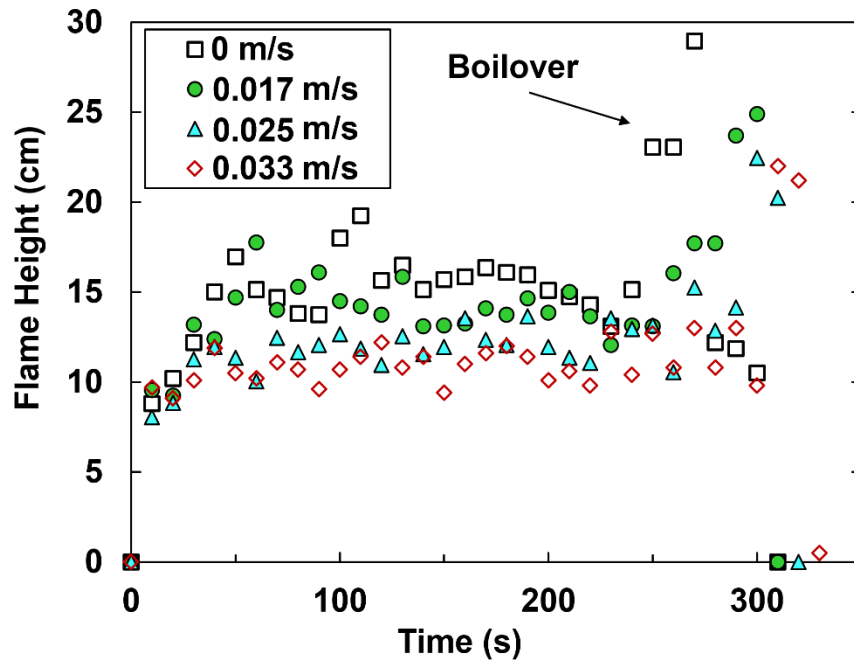
Figure 3. 4: Flame height during oil slick burning under different water turbulence intensities. Each presented dot is a 10-second average. The flame height decreases as turbulence in the water sublayer becomes stronger, and the on-set of boilover comes late with reduced intensity.

Figure 3.5a – b illustrates a series of video snapshots of flame conditions at different timestamps (20, 100, 200, 300 seconds) and on-set of boilover for all cases. The boilover intensity peaks at the baseline burning case, with the shortest time to reach the onset of boilover. During the baseline boilover at 270 s (Fig. 3.5a), the ejection of the oil droplets is so intensive that the flame is thrown up to reach a maximum flame height of 30 cm. The self-quench quickly follows the boilover where flame height suddenly reduces to a low level of 13 cm at 300 s. The turbulent cases share the same

transition between the quiescent burning of the oil/water heating stage and the onset of boilover (Fig. 3.5b – d), but the flame heights and boilover intensities both are subject to a certain degree of reductions. As shown in Figure 3.5d, when $u' = 0.033$ m/s, the onset of boilover has delayed to 310 s and only a limited number of droplets are ejected into the flame, where the boilover flame height is only 19 cm, which is not significant increase compared to the pre-boilover flame height of 14 cm at 300 s. The time to onset of boilover is increased as it becomes difficult for the heat to be accumulated at the oil/water interface to achieve the superheated condition of the water layer. The weaker boilover in turbulence cases is also responsible for the reduction in MLR as lesser oil droplets are directly consumed in the flame zone.
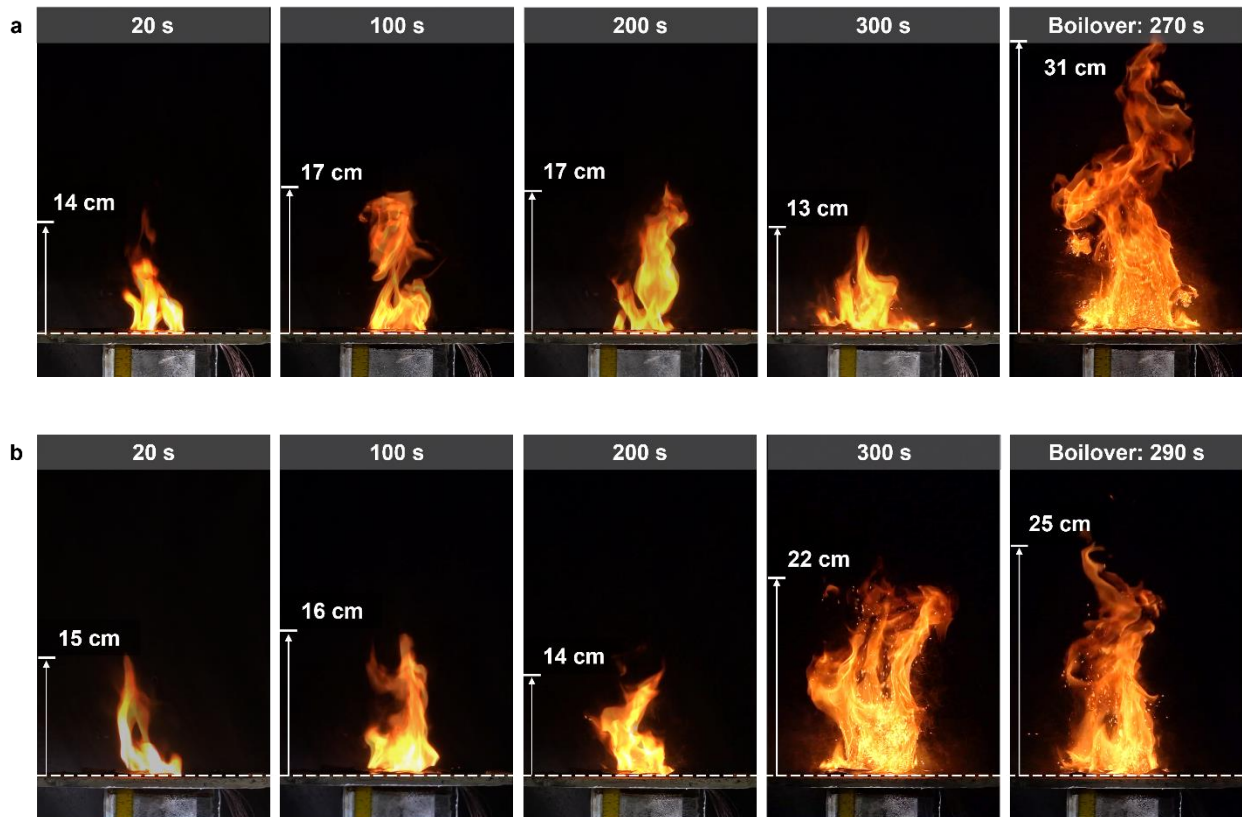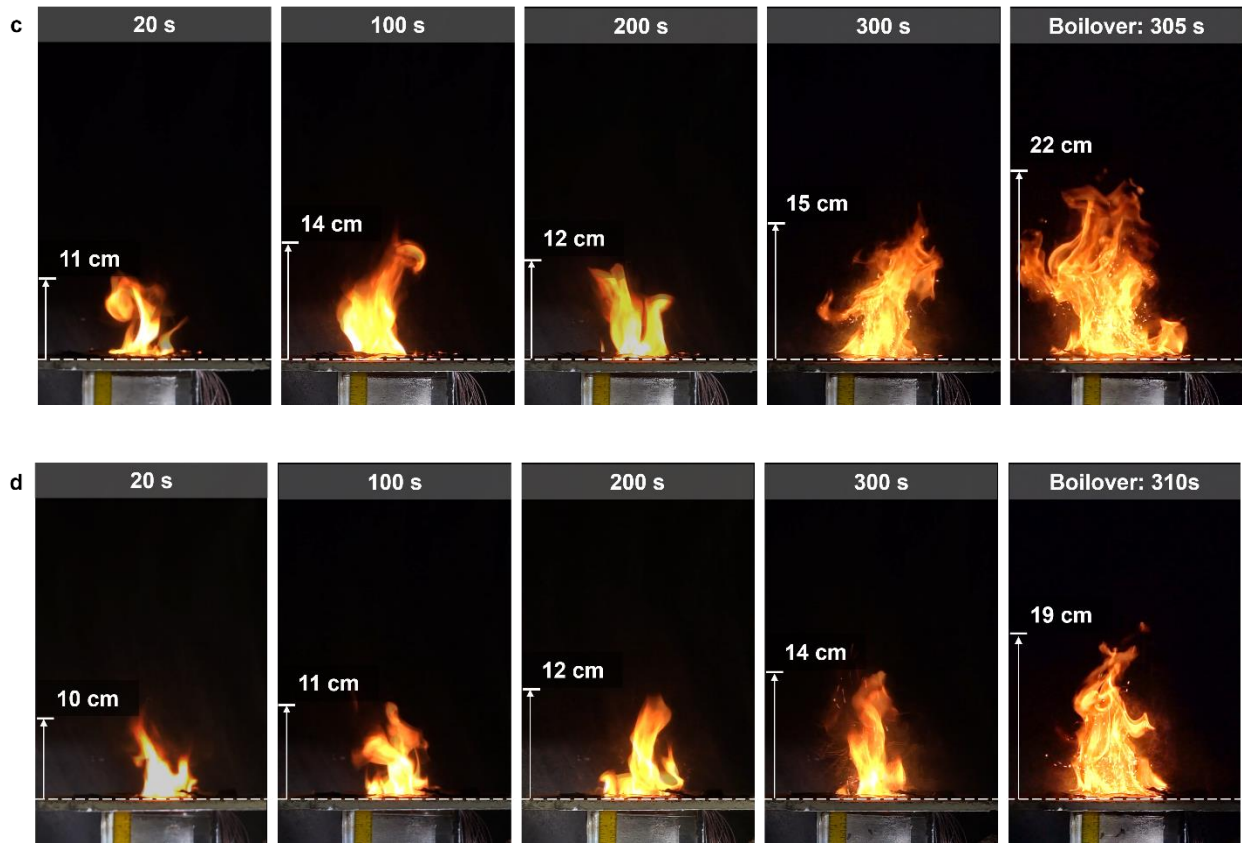
Figure 3. 5: Snapshots of the flame at a series of timestamps of 20, 100, 200, 300 s after the ignition. Flame heights are marked at each timestamp under each turbulence intensity, u'. Boilover behaviors are presented in the last column with its time to onset of boilover. (a) $u' = 0$ m/s (baseline); (b) $u' = 0.017$ m/s; (c) $u' = 0.025$ m/s; (d) $u' = 0.033$ m/s.

3.3.3 Temperature profile in oil and water layers

Figure 3.6a – d shows the temperature profiles measured by thermocouple array in oil and water layers in time series for baseline and turbulence cases. Each dot is averaged within 10 seconds (1 Hz data acquisition rate) for 20, 100, 200, 300 s timestamps. The grey areas indicate the initial oil slick and the blue regions represent the water sublayer. The turbulence causes temperature profiles to develop distinctively compared to the baseline temperature profile, such that the gradient temperature distribution in the water sublayer in baseline (Fig. 3.6a) disappears in all the turbulence cases (Fig. 3.6b – d).

For the turbulence cases, the hot water sublayer adjacent to the oil/water interface is continuously cooled by fresh water because of the turbulent mixing effect. Such a mixing effect keeps the water

layer at ambient temperature at any depth and therefore facilitates the heat loss from the burning oil slick. While for the baseline case, the convection of the water sublayer is very limited because the hot layer close to the hot oil layer will stay at its initial higher position, which results in a much slower heat diffusion downwards into the cooler water layer. The oil slick, therefore, can maintain a higher average temperature, which is shown by the steeper slope of temperature in the oil layer (Fig. 3.6 a). Under no turbulence condition, the water sublayer near the oil/water interface is heated effectively and superheats at around 120 °C, which agrees with observations by Garo et al. [19,20] for boilover to occur. For turbulence cases, the temperature at the interface is measured to be lower than 50 °C, while the boilover phenomena are still present. This is because the oil/water interface is moving up and down constantly so the thermocouple at that position (-5 mm) will be exposed to both the hot oil layer and cool water sublayer during the 10 seconds averaging period. It is very difficult to track and precisely measure at the moving interface. Based on the fact that boilover is observed for all the turbulence intensity conditions, we can confirm that the thin water layer adjacent to the oil/water interface is superheated enough to create bubble nucleation.
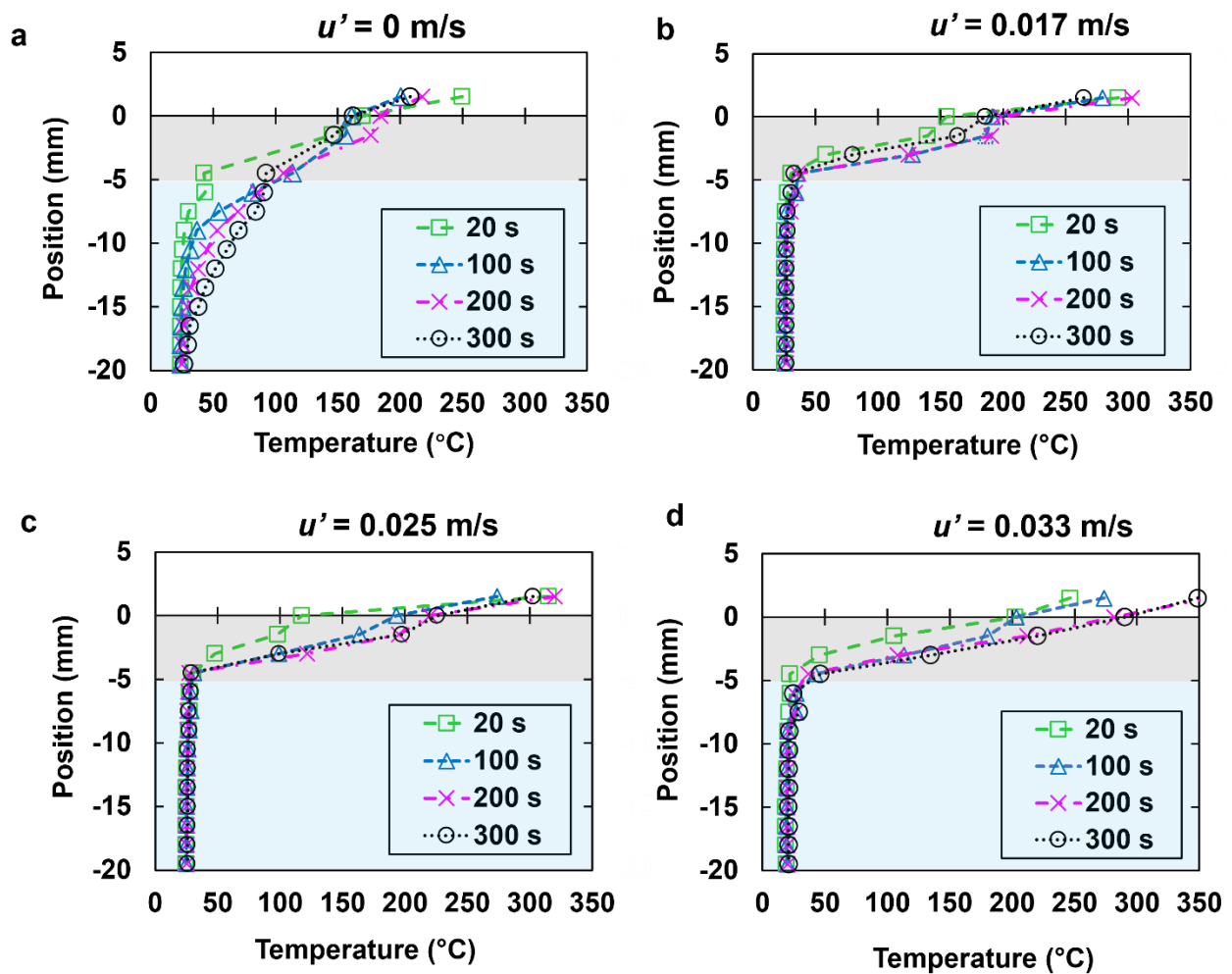
Figure 3. 6: Temperature profiles of oil and water layer measured by the thermocouple array at different timestamps of 20, 100, 200, 300 s after ignition. Each dot is 10-second averaged. (a) $u' = 0$ m/s (baseline); (b) $u' = 0.017$ m/s; (c) $u' = 0.025$ m/s; (d) $u' = 0.033$ m/s.

3.4 Burning Rate Formulation

3.4.1 General statements

Figure 3.7 shows the schematic of the problem. The convection in the thin oil layer can enhance the heat transfer close to the oil surface, but the importance of convection decreases with a viscosity [20]. It can be neglected for the crude oil relevant to this study [21]. For simplicity, this analysis will assume the radiation is fully absorbed at the surface, the following energy balance can be made at the oil surface:

$$\dot{q}_S'' = H_v \rho_F r + \dot{q}_{cond}'' \quad , \tag{3.1}$$

where $\dot{q}_{cond}'' = -k_F \left(\frac{\partial T}{\partial y}\right)_{y=0}$ is the heat conducted into the oil layer, H_v is the latent heat of vaporization, ρ_F is the density of crude oil, r is the regression rate, $\dot{q}_S''$ is the flame heat flux per unit area reaching the oil surface and it can be expressed as [21]:

$$\dot{q}_S'' = \chi \frac{4\rho_\infty c_{p,air}(T_\infty g(T_f - T_\infty))^{1/2} D^{1/2}}{\pi} \quad , \tag{3.2}$$

where ρ_∞ is the density of the air at ambient temperature, $c_{p,air}$ is the specific heat at constant pressure and ambient temperature for air, g is the acceleration of gravity ($g = 9.81$ m/s^2), T_f is the average flame temperature ($T_f \approx 1100$ K in this study [99]), D is the diameter of the pool.
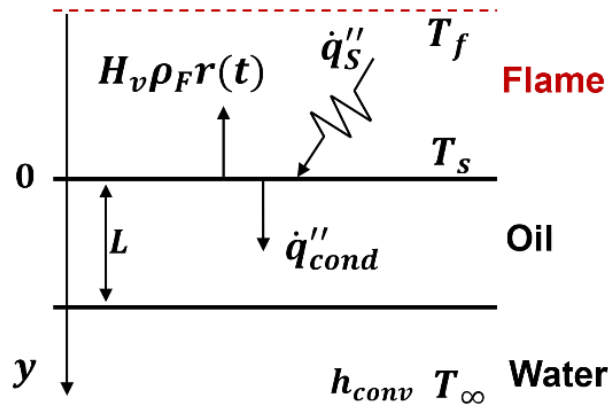
Figure 3. 7: Schematic of the problem studied. $\dot{q}_{cond}''$ **is the heat conducted into the oil layer,** $y = 0_-$ **stands for the location at the oil surface towards the oil layer,** H_v **is the latent heat of vaporization,** ρ_F **is the density of crude oil,** r **is the regression rate,** $\dot{q}_S''$ **is the flame heat flux per unit area reaching the oil surface,** T_f **is the average flame temperature,** T_s **is the boiling point of crude oil.** h_{conv} **is the convective heat transfer coefficient in the water sublayer.**

3.4.2 Burning rate model

After the ignition, the oil and water sublayer undergo a transient heat process that will eventually lead to a steady regression rate. Steckler et al. [101] and Butler [102] have shown that the short transient process is followed by an almost steady regression rate. As shown in Figure 3.6, the temperature profiles of the oil slick will become steady under 100 s after the ignition for all the

cases. The short temperature development time is because of the thin initial oil thickness, and for turbulent cases, the temperature profile becomes steady in an even shorter time is because the increased heat diffusion reduces the thermal penetration process through the oil layer. Therefore, the average regression rate can be used in the burning rate model in Equation (3) to calculate the heat flux required for fuel evaporation.

In this section, the measured regression rate by experiments will be implemented in Equation (3): $\dot{q}''_{vap} = H_v \rho_F r$, which represents the heat flux required to evaporate the regressed fuel. The conduction term $\dot{q}''_{cond}$ that goes into the oil layer can be also obtained by the experiments using thermocouple measurement data next to the oil surface. The flame heat flux $\dot{q}''_S$ is expressed in Equation (4) and should equal to the sum of $\dot{q}''_{vap}$ and $\dot{q}''_{cond}$ because of the energy balance at the oil surface. Those heat flux values in all the experimental cases are shown in Figure 3.8. As the water sublayer become turbulent, the heat sink effect is enhanced, increasing the amount of conductive heat ($\dot{q}''_{cond}$) that goes into the oil layer. In such circumstances, the increasing heat loss causes a reduction in MLR (Fig. 3.3) or regression rate. Therefore, the heat required for oil evaporation ($\dot{q}''_{vap}$) is reduced. With fewer combustible vapor being released into the flame zone, the oil slick burning rate decreases, resulting in the reduction in flame height (Fig. 3.4 and Fig. 3.5). Eventually the flame heat flux ($\dot{q}''_S$) is attenuated and such a negative cycle explains the influence of the turbulent water sublayer on the oil slick burning characteristics.
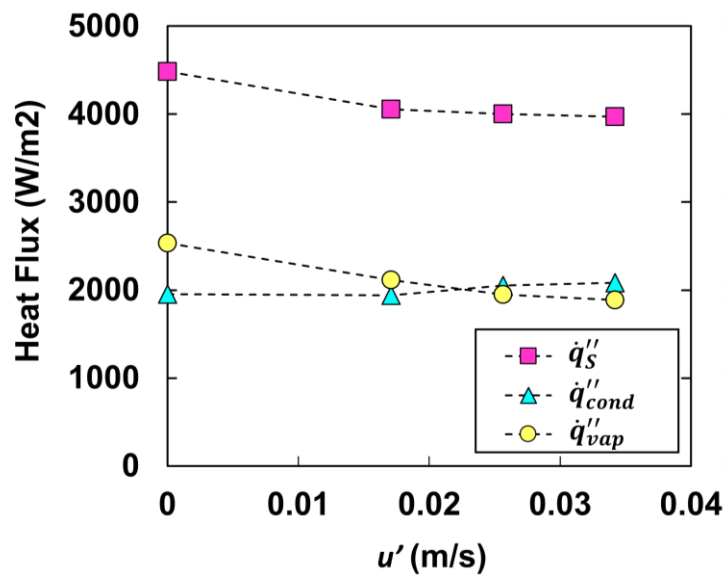
Figure 3. 8: Flame heat flux ($\dot{q}_S''$), heat flux required for oil evaporation ($\dot{q}_{vap}''$) and heat flux due to conduction into the oil layer ($\dot{q}_{cond}''$) for baseline and turbulent cases.

Finally, the only unknown χ which can be solved since the flame heat flux $\dot{q}_S''$ has already been obtained. This value is a small fraction of the total combustion heat release rate which represents the net heat fed back per unit area to the oil surface and it is independent of the pool diameter [103]. The values of χ for baseline and turbulent cases are shown in Table 1.

Table 3. 1: Specific fraction (χ) of the heat released fed back to the fuel surface under different u'.

$u'\ (m/s)$	$\chi\ (\times 10^{-3})$
0 (Baseline)	5.25
0.017	4.75
0.025	4.69
0.033	4.65

The above values of χ are comparable to data presented by Arai et al. [18] and Torero et al. [21]. Farahani et al. [93] used χ of 5×10^{-3} for Alaska North Slope crude (ANS) oil as the estimation of heat release fed back to the fuel surface, which matches well with the obtained χ in this study. As all the values except for χ in the expression for $\dot{q}_S''$ are constant, the heat source term in the burning rate model is default to have a fixed total heat release rate. However, the heat release rate of the oil layer combustion will decrease as the turbulence intensity in water sublayer increases. The fraction (χ) essentially represents such reduction in the heat source supplied onto the oil surface, therefore it decreases with the presence of turbulence and keeps going down with stronger turbulence.

3.4.3 One–dimensional oil layer conduction model

The one-dimension conduction model in this study is based on the works of Arai et al. [18] and Garo et al. [20], and the analysis interest is only within the oil layer. The heat conduction equation is given by:

$$\frac{\partial T}{\partial t} = \alpha_F \frac{\partial^2 T}{\partial y^2} \quad , \tag{3.3}$$

with the initial condition at

$$t = 0, T = T_\infty \quad , \tag{3.4}$$

and boundary conditions

$$y = 0, \quad T = T_S \quad , \tag{3.5}$$

$$y = L, \quad -k_F \left(\frac{\partial T}{\partial y}\right) = h_{conv}(T - T_\infty) \quad , \tag{3.6}$$

where α_F is the thermal diffusivity of crude oil, L is the initial oil thickness. The properties used are shown in Table 2. To account for the turbulent water sublayer, the boundary condition at the oil/water interface is set such that the conductive heat from the oil layer equaling to the convection in the water sublayer with a convective heat transfer coefficient, h_{conv}. By changing the heat transfer coefficient (h_{conv}) to match the temperature profiles of experimental measurements and numerical results. The specific h_{conv} for each experimental case can be obtained and are shown in Figure 3.9.

Table 3. 2: Properties used in the model

	T_S (K)	H_v (kJ/kg)	k (W/mK)	ρ (kg/m^3)	c_p (kJ/kgK)	α ($\times 10^7$) (m^2/s)
Crude oil	478	250	0.132	845	2.30	0.679
Air	538	377	0.026	1.16	1.00	225
Water	373	2257	0.590	998	4.18	1.414

As mentioned previously, the Reynolds number of the confined jet system is at the range of 34,000 – 68,000 for current works. The corresponding h_{conv} values from the model are given in the range of 93 – 127 W/m^2. This range agrees well with the experimental results from Sargison et al. [104],

58

where the low-speed heat transfer in their study with the Reynolds number of 36,000 is found to have the h_{conv} at the range of 65 – 100 W/m^2.
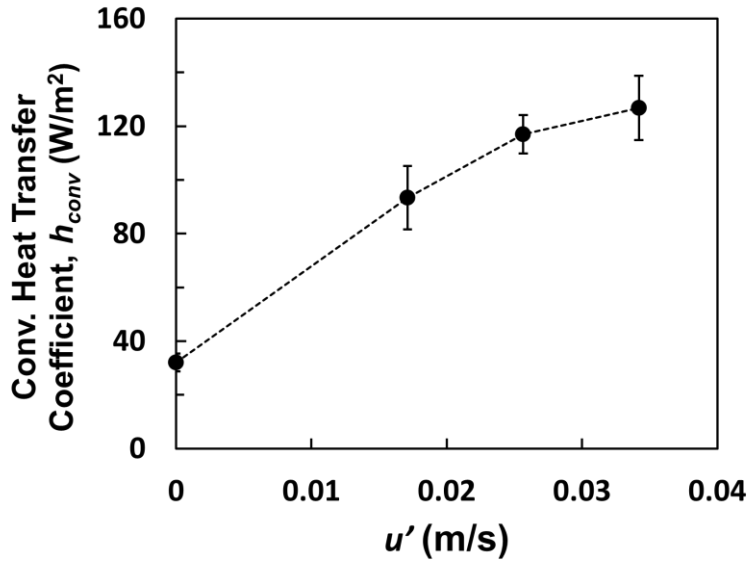
Figure 3. 9: Convective heat transfer coefficient in water sublayer as a function of the turbulence intensity u'. The error bars represent the standard deviation of three repeated experimental temperature measurements.

In the baseline case, the heat transfer coefficient stays at the lower value of 32 W/m^2, because there is no forced turbulent convection in the water sublayer. Since the natural convection has a limited intensity level during the pre-boilover burning stage, the heat transfer is dominated by conduction from the hot oil/water interface to the water sublayer (Fig. 3.6a). It is after the onset of boilover, where the violent bubble nucleation introduces perturbance at the interface, that the convection starts to impose on the heat transfer process. During the boilover stage, the hot oil droplets will not only be ejected upwards into the flame, some of which will be thrown downwards into the water sublayer. While even with such droplet dynamics, the overall convective heat transfer coefficient is still low.

For the turbulent cases, the convective heat transfer coefficient has a distinctive increase to 93 W/m^2 at turbulence intensity $u' = 0.017$ m/s. As the turbulence intensity increases, the increase of convective heat transfer coefficient slows down. When u' is doubled to 0.033 m/s, the h_{conv} only increases to 127 W/m^2. The sudden rise of the convection heat transfer is because even under

the weakest water layer turbulence, the turbulence mixing can maintain the water sublayer at ambient temperature (Fig. 3.6b). The sublayer movement will constantly replace the hot water with cool water from the bulk water ambient. The convective heat transfer has become the more dominant means for heat loss compared to the baseline case having conduction as major means of heat loss. Therefore, the convective coefficient increasement from $u' = 0$ m/s to $u' = 0.017$ m/s is quite considerable. As the turbulence further increases, the mixing effect becomes more intensive, and the replacement rate of the hot water is higher. While such heat transfer enhancement has slowed down.

3.4 Conclusions

A series of experiments are conducted to understand the influence of surface turbulence on the oil slick burning on a water bath. Crude oil slick with an initial thickness of 5 mm has been used and the mass loss rate decreases when the water sublayer is made turbulent. A weaker burning process with smaller flame height and boilover behavior is observed as the turbulence intensity becomes stronger. The thermocouple array measurements indicate that the water sublayer cannot develop temperature gradients even at the low level of turbulence intensity at $u' = 0.017$ m/s. The heat reaching the water will be instantly taken away because of the turbulent mixing thus facilitating the heat loss of the oil slick, which causes a reduction in MLR up to 34% at $u' = 0.033$ m/s compared to baseline. The convective heat transfer coefficient in the water sublayer is obtained by matching the one-dimensional conduction model to the measurement data and has the value of $h_{conv} = 78$, 93, 125 W/m^2 corresponding to $u' = 0.017$, 0.025, 0.033 m/s. The values of χ indicate the fraction of the total combustion heat release rate being absorbed onto the fuel surface, and it decreases with the turbulence intensity which is a result of weakened flame causing heat flux changes in the mass burning rate model. The heat and mass transfer characteristics during the oil slick burning are highly related and both are subject to the impact of the presence of turbulence in the water sublayer. The results in this study reveal the challenge of in-situ burning in the ocean environment in detail and can potentially lead to improve oil removal efficiency in the following chapter.

Chapter 4: Heptane and dodecane fuel slick burning with an immersed copper rod

4.1 Problem Statement

In this Chapter, a more complicated burning configuration is studied, where a copper rod (Flame Refluxer) is introduced to the floating fuel slick region. The rod placement location has a specific design such that the lower rod section is immersed in the fuel and water layer and the upper section is exposed to the flame. Under this burning condition, the copper rod has two major heat transfer behaviors. The first is heat collection in the gas phase, where the combustion heat released in the reaction zone is collected by the copper rod surface. Some amount of this collected heat will be transferred through the rod body to the liquid layer in the immersed section, where the second behavior as the liquids heating element occurs. The fuel slick thus has two ways of receiving heat, of which one is thorough the gas phase directly and the second is through the copper rod that collects the heat from the flame and transmits it to the fuel slick. Because of the additional heat transfer terms introduced with the copper rod, the burning problem becomes more involved with heat source and heat loss terms interacting among the rod body, fuel slick, and turbulent water sublayer.

Figure 4.1a shows the fuel slick burning with no immersed rod. The regression rate of a floating fuel slick can be modeled by an energy balance equation at the fuel surface [21], such that the heat used for fuel evaporation ($\dot{m}_F L_F$) equals the difference of surface heat input from the flame ($\dot{q}_s$) and the conduction heat loss into the fuel layer at the gas/fuel interface ($\dot{q}_{cond}$). The equation can be written as:

$$\dot{m}_F L_F = \dot{q}_s - \dot{q}_{cond} \quad , \qquad (4.1)$$

where L_F is the heat of gasification of the fuel, and it can be expressed as: $L_F = \Delta H_F + c_{p,l}(T_b - T_\infty)$. ΔH_F is the energy required to vaporize a unit mass of liquid at boiling temperature, T_b. $c_{p,l}(T_b - T_\infty)$ is the energy needs to raise a unit mass of liquid from original temperature to T_b. The mass burning rate $\dot{m}_F$ is:

$$\dot{m}_F = \rho_F r(t) \quad , \tag{4.2}$$

where ρ_F is the fuel density, and $r(t)$ is the regression rate of burning fuel. The convection in the thin fuel layer can enhance the heat transfer close to the fuel surface, but the importance of convection decreases with an increase in viscosity [20]. For the turbulent cases in this study, the convection in the water sublayer will be considered as a means of heat loss from the fuel layer. When the water sublayer is made turbulent, the temperature profile will be affected because of the mixing and cooling in the water bath. The overall temperature of the fuel layer will decrease as the heat loss through the fuel/water interface is enhanced by convection, which leads to a lower interface temperature (Fig 4.1). This temperature profile has a distinctive difference compared to conventional no turbulence burning conditions, where the continuous temperature change is formed in the fuel and water layers. While in the turbulent condition, there will be a sudden temperature drop at the lower side of the interface as the hot water at this level is constantly replaced by the cool water carried by the turbulence. This change of heat transfer behavior at the interface will have an impact on the in-depth conduction term, $\dot{q}_{cond}$ at the fuel surface. Given that the burning fuel surface temperature is maintained at the boiling temperature T_b, and $\dot{q}_{cond}$ is dependent on the temperature profile within the fuel layer, the boundary condition at the fuel/water interface thus becomes a crucial subject to analyze. Note that in reality, the burning surface temperature, T_s is slightly less than T_b and can be obtained by the thermodynamic equilibrium condition with the Clausius – Clapeyron equation. However, for practical purpose the T_s and T_b can be comparable with an error less than 2% [105]. As the water sublayer becomes turbulent, the boundary condition changes into convection form other than conduction in no turbulence condition. Such convective heat transfer in the water layer relates to and increases with the turbulence intensity, u', which has also been discussed in Chapter 3.
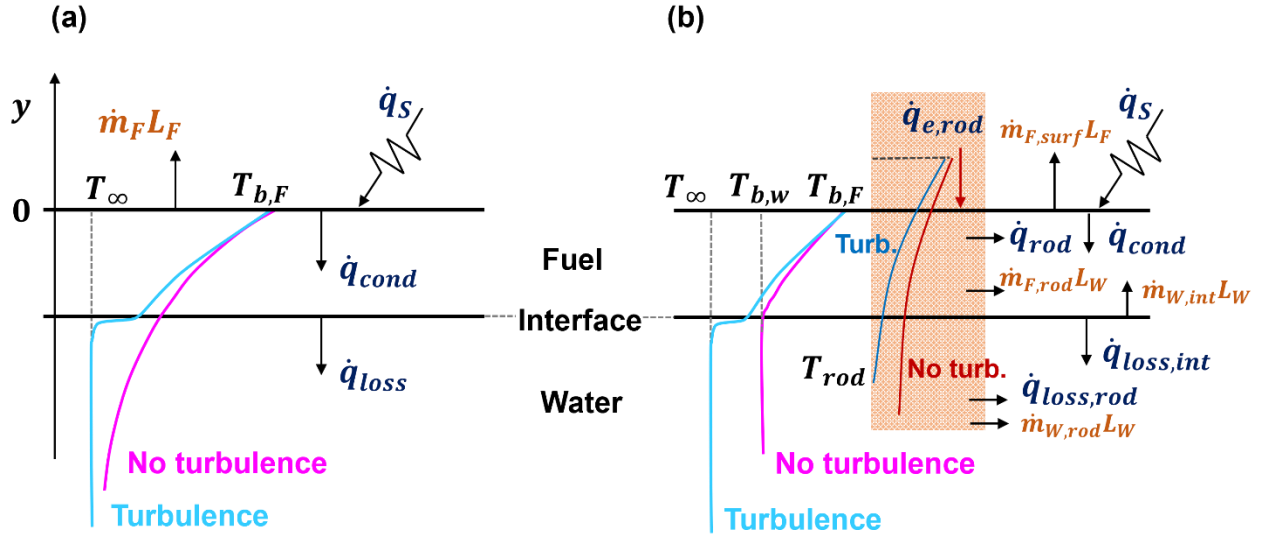
Figure 4. 1: Schematics of the heat transfer energy terms and temperature profiles. (a) Fuel slick burning without copper rod. (b) Fuel slick burning with the immersed copper rod. Assume the temperature profiles are in steady burning stage, and the heat loss laterally through the cylinder wall is neglected.

Figure 4.1:

Figure 4.1b shows the energy balance at the fuel surface in a more complicated burning condition with an immersed copper rod. The energy input, $\dot{q}_s$ and loss, $\dot{q}_{loss}$ at the liquid layers are still present in this case, and the extra energy components introduced by the copper rod will change the energy balance formulation as,

$$\left(\dot{m}_{F,rod} + \dot{m}_{F,surf}\right)L_F + \left(\dot{m}_{W,rod} + \dot{m}_{W,int}\right)L_W = \dot{q}_s + \dot{q}_{e,rod} - \dot{q}_{loss.int} - \dot{q}_{loss.rod} \quad ,(4.3)$$

where $\dot{q}_{e,rod}$ is the external heat input coming through the rod's cross-section area. The heat loss term now includes two components. One is $\dot{q}_{loss.int}$ at the fuel/water interface, and the other one is $\dot{q}_{loss.rod}$ on the rod bottom area in the water sublayer. The surface energy input terms $\dot{q}_s$ and the energy used for fuel evaporation at the surface $\dot{m}_{F,surf}L_F$ are the same as no rod condition.

For both burning conditions (Fig. 4.1), the regression rate is therefore determined based on the net energy input within the fuel layer, which is consumed by fuel evaporation at the surface ($\dot{m}_F L_F$). $\dot{m}_{F,rod}$ and $\dot{m}_{W,rod}$ are the mass of fuel and water bubble generation on the rod respectively. $\dot{m}_{W,int}$ represents the water bubble generated on the fuel/water interface due to boilover. Those terms cause latent energy transfer because of the placement of the copper rod. Note that it is not

necessary for all the terms to appear all at once. Under each burning condition, the bubble behaviors are different, and the energy balance equation will be modified to accommodate that. The total energy input through the rod, $\dot{q}_{e,rod}$ dissipates into both liquid layers. However, in difference liquid layers, the heat transfer intensities can have huge difference depending on whether nucleate boiling will occur. Figure 4.2 shows the areas where heat transfer takes place in the rod's immersed section. A_1 is the rod's cross-section area at the fuel/air interface through which $\dot{q}_{e,rod}$ is transferred to the liquids. In addition, A_1 is the original fuel surface area that is taken away because of the rod. A_2 is the rod's side area within the fuel layer where the energy from the rod works to facilitate the burning rate. A_2 can be considered as a new fuel surface area that can provide: (1) heat transfer to the fuel layer if no boiling enhancement on $\dot{m}_F$; (2) heat and mass transfer when boiling occurs. In the second situation, there will be an enhancement on $\dot{m}_F$ because of more heat being supplied to the fuel layer as boiling heat transfer is strong and the fuel is vaporized directly into escaping bubbles. A_3 is the rod's area in water, which provides: (1) heat loss to the water sublayer if no boiling occurs; (2) heat loss to the water layer plus heat loss to water vapor if boiling occurs. The decisive factor of the boiling location is the boiling temperature of the fuel, $T_{b,F}$. When the fuel boiling point is higher than water boiling point ($T_{b,F} > T_{b,W}$), the nucleate boiling will happen only in water on A_3. In this case, the generated bubbles become water vapor instead of fuel vapor, and the burning will be suppressed rather than being facilitated. If the fuel boiling point is lower than water boiling point ($T_{b,F} < T_{b,W}$), the nucleate boiling area will be A_2 within the fuel layer (Fig 4.2). In this case, generated bubbles of fuel vapor rise to the surface, burst and enhance mass burning rate, which causes a positive heat feedback loop and further facilities the burning.

Figure 4. 2: Schematics of rod areas and nucleate boiling conditions in the immersed section. A_1 is the rod's cross-section area at the fuel/air interface. A_2 is the rod's side area within the fuel layer. A_3 is the rod's side wall plus bottom area immersed in the water sublayer.
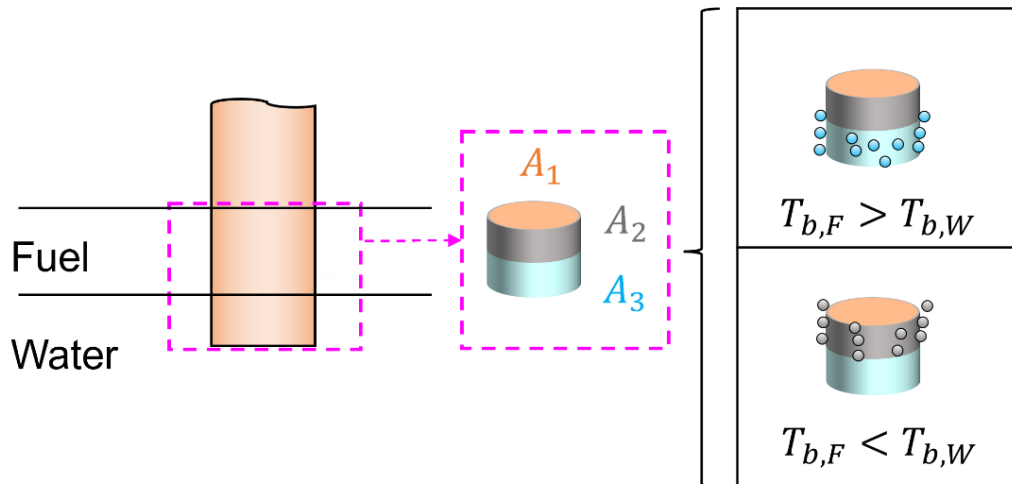
Rod dia. (mm)	A_1 (m^2)	A_2 (initial) (m^2)	A_3 (m^2)
10	7.85×10^{-5}	1.57×10^{-3}	3.93×10^{-4}
20	3.14×10^{-4}	3.14×10^{-3}	9.42×10^{-4}

The temperature profiles of the rod case shown in Figure 4.1 (b) reveal important aspects to set up the heat transfer boundary condition at the water sublayer. Under turbulence conditions, the sudden temperature drop can be described by a convection boundary condition. While for zero turbulence conditions, the temperature profiles for both rod and no rod cases have no discontinuity at the fuel/water interface since the heat transfer is by conductive heat diffusion from the hot fuel layer to the water underneath. For that reason, the boundary condition can be described in a conduction form. Also note that the water sublayer with the immersed rod condition can reach the boiling temperature, where there will be no temperature gradient in the water sublayer when such a temperature profile is developed. The temperature gradient will also be formed within the copper rod (Fig. 4.1 (b)). Despite the high thermal conductivity of copper, the temperature profile at the gas/fuel interface still sees a noticeable decrease. Such temperature difference drives the energy from the hot heat-collecting section into the immersed section in the liquids and can be measured to obtain the external heat input, $\dot{q}_{e,rod}$. When the water layer becomes turbulent, the overall

temperature in the immersed rod section is lower than no turbulence condition as the rod bottom area will be exposed to a much cooler water bath.

4.2 Experimental Setup

Figure 4.3 shows the experimental setup schematic and photograph. The turbulence generation platform introduced previously was used to create the isotropic turbulence at the water layer. The turbulence intensity in this chapter was set to the range of $u' = 0$ (baseline), 0.017, and 0.033 m/s. As discussed in Chapter 3, a desired u', can be easily set in the current experimental platform by adjusting the flow rate of the water jet. Further, the turbulence is isotropic and therefore an idealized turbulent boundary condition can be imposed in the water sublayer to analyze the influence of wave generated turbulence during fuel layer burning. A thermocouple array consisting of 13 K-type 36 Gauge thermocouples was placed vertically at the cylinder inner wall. The total measurement depth was 21 mm (Fig. 4.3a), which created a 1.2 mm spacing between thermocouples. Two sizes of copper rods were used in the experiment with diameters of 10 and 20 mm. The total length of each rod was 150 mm, and it was placed at the top of the platform using a holding structure shown in Figure 4.3b. The structure had a quick release sliding mechanism to adjust the vertical position of the copper rod. The bottom of the rod was immersed at 10 mm lower than the fuel/water interface before each experiment, which was 15 mm below the fuel surface. The rod top section with a length of 35 mm was clamped on the holding structure, which allowed a 100 mm length of the rod surface exposed to the fire as the heat collection area. The ceramic fiber was used as insulation between clamping surfaces to prevent heat loss to the holding structure. Each copper rod was polished with 2000 Grit sandpaper before experiments for constant surface finish.
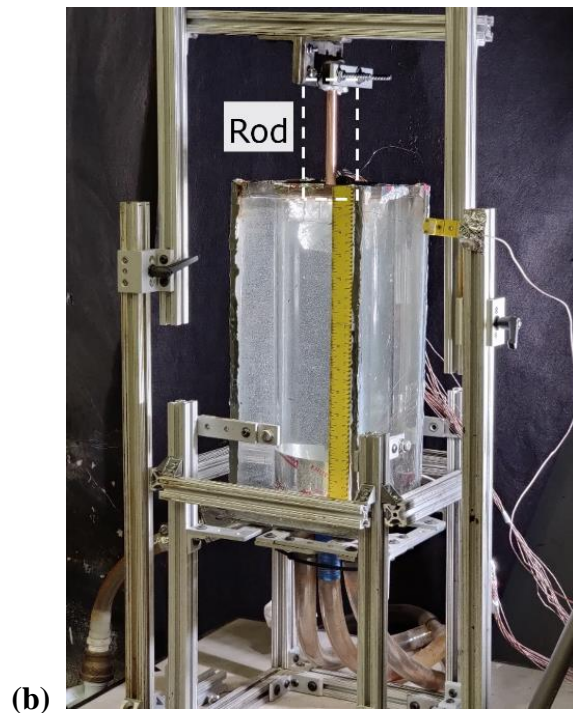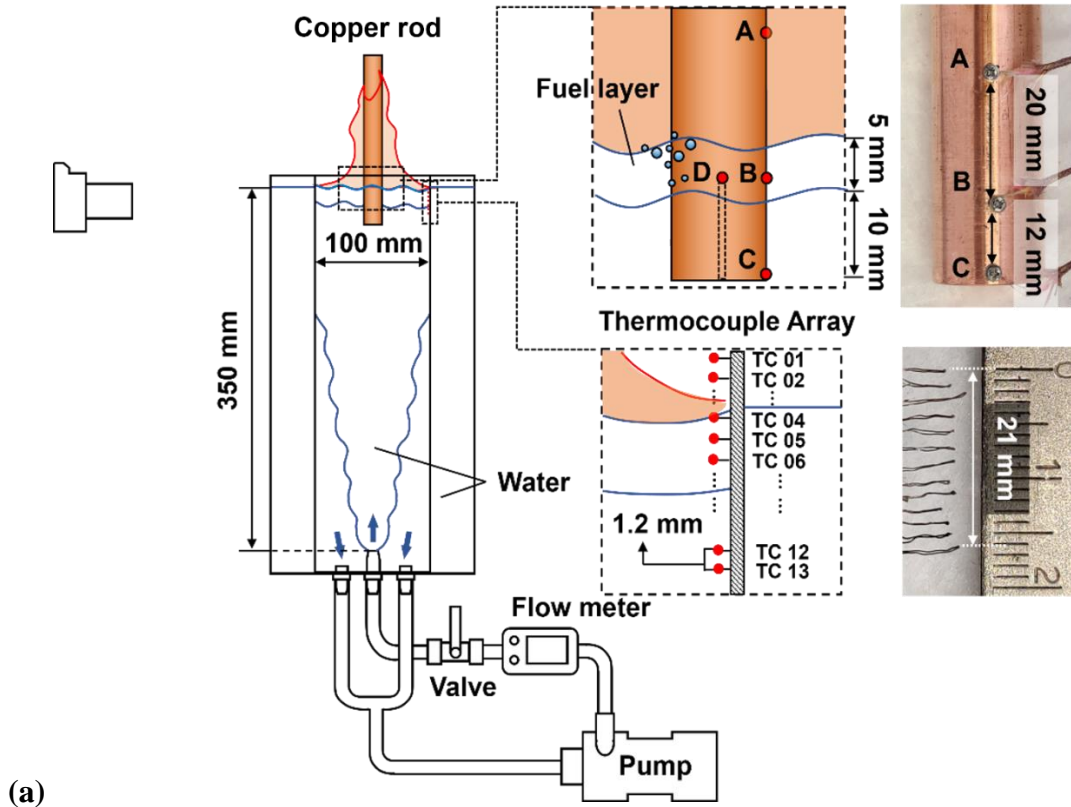
Figure 4. 3: (a) Schematic of the experimental setup with photographs of the rod thermocouple positions and thermocouple array. (b) Photograph of the experimental setup, including the turbulence generation system, the fuel slick burning platform, and the rod holding structure.

Four K-type thermocouples were implemented in each copper rod, where three were fixed on the surface (A, B, and C) and one was embedded at the center axis inside of the rod (D). Thermocouple A was fixed above the fuel surface in the gas phase. Thermocouple B was located within the fuel layer and thermocouple C was fixed at the bottom of the rod in the water sublayer. The spacing between A and B was 20 mm. The spacing between B and C was 12 mm (Fig. 4.3a). The sampling rate for all the thermocouples was set to 1 Hz.

Dodecane and heptane were selected as the fuel types and the initial fuel thickness was 5 mm for all the experiments. The choice of dodecane and heptane as fuels was because of different boiling behaviors at the rod' surface because of their boiling points of 216 °C ($T_{b,F} > T_{b,W}$) and 98 °C ($T_{b,F} < T_{b,W}$). For dodecane layer burning on a still water surface with a rod immersed in fuel and water layers, the bubble nucleation would only occur on the rod's surface in the water layer, which yielded additional water vapor mass generation, $\dot{m}_{W,rod}$, causing suppression effects on burning compared with the no rod case. The high heat flux coming from the rod was lost to the water layer due to water bubble vaporization instead of supplying heat to the dodecane layer. While for heptane layer burning, since the boiling temperature of the fuel was lower than water, the nucleation sites were only observed within the heptane layer on the rod's surface, yielding additional fuel vapor mass generation, $\dot{m}_{F,rod}$. In this case, the combustion was enhanced because of additional heptane vapor. Each boiling mode will be discussed in detail in this chapter.
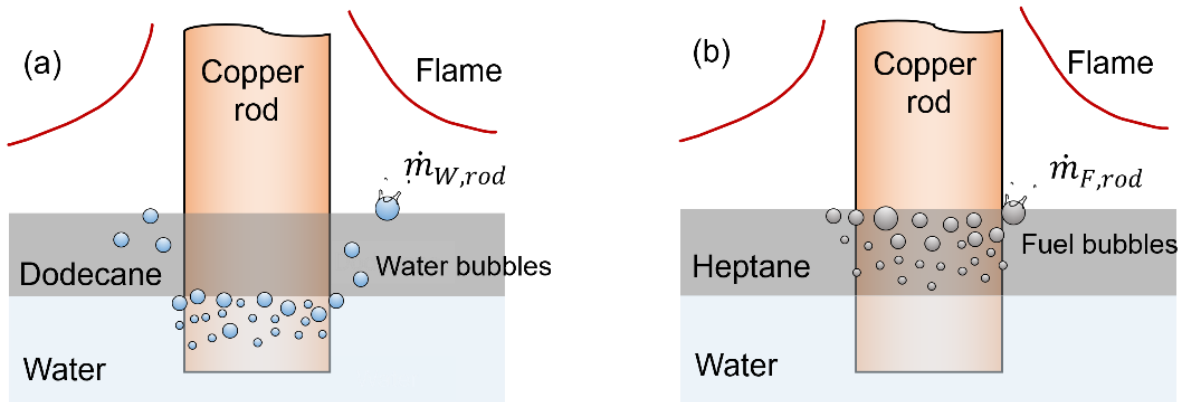
Figure 4. 4: Schematic of nucleate boiling modes in still water condition. (a) Dodecane layer burning. Nucleation sites in the water layer. (b) Heptane layer burning. Nucleation sites in the heptane layer.

Two Chronos 1.4 highspeed cameras with macro lenses were used to record the bubble departure size and frequency at the nucleation sites, of which one camera was set to focus on the immersed rod surface at 2873 frames per second (FPS) with a resolution of 800×600. Another one looked down on the fuel surface at 1057 FPS with a resolution of 1280×1026 to capture water bubbles generated by boilover. The different camera settings were to ensure the capture of the entire development and departure process of each bubble. The bubble departure rate on the rod's surface was much faster with smaller departure size compared with the boilover water bubbling at the fuel surface. The departure size and frequency data were used to calculate the amount of energy for different liquid vaporization. For the flame height recording, a DSLR camera was used with the setting of 60 FPS at 1920×1080 resolution. This camera also was used to record the burning time, which yielded the average regression rate or mass loss rate (MLR) by dividing the initial fuel thickness or initial fuel mass. The experiment matrix is shown in Table 4.1 and each experiment was repeated three times.

Table 4. 1: Experiment matrix.

Parameters	Values
Fuel Type	Dodecane, heptane
Fuel Initial Thickness	5 mm
Rod Length	150 mm
Rod Diameter	0, 10, 20 mm
Turbulence Intensity	0, 0.017, 0.033 m/s

4.3 General Statements for the Burning Rate Formulation

The introduction of a copper rod complicates the energy terms during the fuel-burning process. For this reason, Equation 4.1 can only be applied to no rod cases. After the ignition of the fuel layer, the copper rod section exposed to the flame begins to absorb heat. Since the top section is insulated by ceramic fiber, and the bottom section is immersed in the fuel and water sublayer, the heat will find its way downwards, dissipating into the liquid layers. The temperature difference between the hot copper surface and ambient liquid boiling temperature will eventually reach the onset of the nucleate boiling. As the nucleate boiling occurs at the rod surface, this amount of latent

energy loss can no longer be described using a surface energy balance equation, because the boiling heat transfer takes place within the liquid layer. The rod also provides an external heat source to the liquid layers. Therefore, the energy input term is not only from the gas phase but the vertical conduction within the copper rod should be included. At this point, a control volume should be identified to account for all the energy terms.

Figure 4.5 shows the schematic of the control volume used for the burning rate model. The cylindrical volume includes the fuel surface as the upper boundary. The bottom of the control volume is at the same level as the copper rod bottom surface. In such configuration, the control volume covers the entire sidewall surface of the immersed copper rod, so that the heat transfer from the hot copper rod surface to the cylindrical liquid body does not need to be experimentally measured for the control volume energy balance. The energy loss, $\dot{q}_{loss}$ at the lower control volume boundary to water bath can be categorized into two parts: heat loss at the rod bottom surface to contacting water layer and heat loss through the remaining water layer at this bottom boundary. Both can be obtained by thermocouple measurements. On the upper boundary, the energy input has two terms: surface heat term from the flame, $\dot{q}_s$ and heat conduction term through the copper rod cross-section area, $\dot{q}_{e,rod}$. The energy loss at the upper surface comes from the fuel regression term, $\dot{m}_F L_F$, which is used to evaporate the fuel.
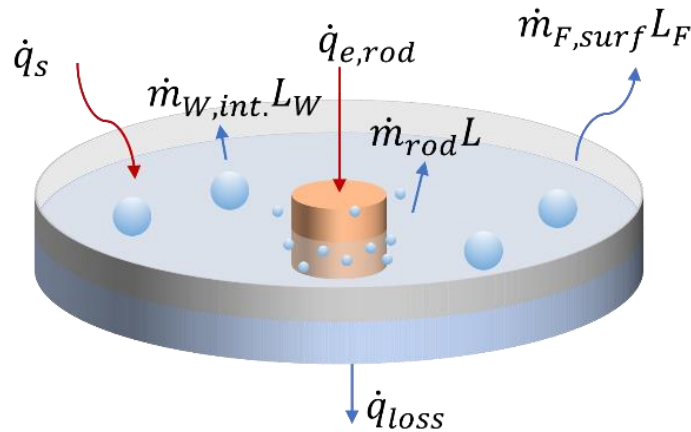
Figure 4. 5: Schematic of the energy balance on the control volume.

The general energy balance equation of the control volume can be written as:

$$\dot{m}_{rod}L = \dot{q}_s + \dot{q}_{e,rod} - \dot{q}_{loss} - \dot{m}_{F,surf}L_F - \dot{m}_{W,int}L_W \quad , \qquad (4.4)$$

where, $\dot{m}_{rod}L$ is the heat used for liquid evaporation on the rod's surface. For dodecane, this term can be expressed as: $\dot{m}_{rod}L = \dot{m}_{W,rod}L_W$, $L_W = \Delta h_{fg,W} + c_{p,W}(T_{b,W} - T_\infty)$. For heptane, $\dot{m}_{rod}L = \dot{m}_{F,rod}L_F$, $L_F = \Delta h_{fg,F} + c_{p,F}(T_{b,F} - T_\infty)$. Δh_{fg} and c_p are the latent heat of gasification and the specific heat of the liquids respectively. $\dot{q}_s$ is the energy input from the gas phase onto the fuel surface, and it can be obtained by thermocouple measurements in the gas phase near the fuel surface [106]:

$$\dot{q}_s = \dot{q}_r + A_F k_{air} \left(\frac{dT}{dy}\right)_{y=0+} \quad , \qquad (4.5)$$

where $\dot{q}_r$ is the radiant heat absorbed on the fuel surface. Radiation through the fuel layer can be of importance [14] but for the fuel of interest it has been demonstrated that most of the radiative heat flux is absorbed very close to the surface [20]. The ratio of the radiative heat flux to the total heat flux is very limited for the small size pool fire. For a 6 cm diameter pool, the average radiant heat flux is roughly estimated to be between $0.3 – 0.5$ W/m^2 [18]. It would of course be ideal to measure the radiant flux at the surface, but a large disturbance to the fuel evaporation would occur for such a small pool fire when a radiometer is placed at the fuel surface. Therefore, we only consider the heating received from the gas phase measured by $A_F k_{air} \left(\frac{dT}{dy}\right)_{y=0+}$. A_F is the fuel surface area, which can be expressed as: $A_F = A_{pool} - A_{rod} = \pi(\frac{D^2}{4} - \frac{d_r^2}{4})$. d_r is the diameter of the rod. k_{air} is the thermal conductivity of the vapor space immediately above the surface at the average temperature in this space. $(dT/dy)_{y=0+}$ represents the temperature slope at the fuel surface and the subscript "+" identifies conditions on the gas side of the surface. $\dot{q}_{e,rod}$ is the external heat addition through the rod into the control volume. It can be obtained by the thermocouple A and B shown in Figure 4.3 (a). $\dot{q}_{loss}$ is the heat loss to the bottom boundary of the control volume. For no turbulence cases, $\dot{q}_{loss} = A_F k_W (dT/dy)_{F/W-}$ where k_W is the thermal conductivity of water and "$F/W -$" denotes the fuel/water interface at the water sublayer side. For turbulence cases, $\dot{q}_{loss} = A_F h_{int}(T_{int} - T_\infty)$ and h_{int} is the convective heat transfer coefficient at the water sublayer. T_{int} is the fuel/water interface temperature. $\dot{m}_{F,surf}L_F$ is the heat used for fuel evaporation at the pool surface. $\dot{m}_{W,int}L_F$ represents the heat used to generate water bubbles at the fuel/water interface during boilover.

The energy terms mentioned above indicate all the heat sources and heat losses in the unit of Watts. Among those, there are obtained experimentally by direct thermocouple measurements such as $\dot{q}_s$, $\dot{q}_{e,rod}$ and $\dot{q}_{loss}$. Some energy terms are obtained by analyzing bubble departure size and frequency via highspeed videography such as $\dot{m}_{rod}L$ and $\dot{m}_{W,int}L_F$. Finally, the remaining term $\dot{m}_{F,surf}L_F$ can be calculated by the energy balance equation.

Experimental results of dodecane burning configurations shown in Table 4.1 will be illustrated and discussed in the following sections, which includes burning regression rates, flame heights, and temperature profiles, and burning rate formulations for dodecane and layer burning. According to the results of Chapter 3, it is known that for fuel slick burning on a turbulent water surface, the burning intensity will decrease as the turbulence gets stronger. The issue occurs because of the increasing convective heat loss in the water sublayer. Based on that, the copper rod is introduced to increase the amount of heat dissipated into the fuel layer, acting against the negative impact of the wavy water sublayer.

Interestingly, the copper rod will not always facilitate the burning rate of the fuel layer. The unexpected reduction in burning rate occurs at the dodecane layer burning with no turbulence cases, where the nucleate boiling was only observed on the rod's surface in the water sublayer because of the lower boiling point of water compared with dodecane. Therefore, the collected heat coming through the copper rod is mostly transferred to the water layer, consumed by the water evaporation process. Also, the water sublayer temperature will quickly rise to the boiling point because of the heat transfer enhancement, which leads to the onset of boilover at the dodecane/water interface. On the contrary, when the heptane layer is burnt, the nucleation sites appear on the copper rod surface within the heptane layer, which facilitates the burning rate. The boilover will not occur at the heptane/water interface because the heptane boiling point is lower than 100 °C, which is not sufficient to bring the water sublayer to superheated condition. For all turbulence cases, no nucleate boiling is observed for either dodecane or heptane burning process. Therefore, the presence of the copper rod will have both positive and negative influence on the burning rate depending on the water sublayer condition.

Given the complexity of the rod and turbulence combinations, the following sections will demonstrate the effect of different sizes of copper rods on dodecane and heptane with/without turbulence in the water sublayer respectively.

4.4 Rod Effects on Dodecane Burning

4.4.1 Regression Rate of Dodecane

Regression rate is defined as the fuel consumption speed during burning and is an important parameter of floating fuel slick burning. Figure 4.6 shows the dodecane layer regression rates for 0, 10, 20 mm copper rods as a function of turbulence intensity.

For the no rod ($d_r = 0$ mm) and no turbulence ($u' = 0$ m/s) baseline case, the average regression rate is 0.6 mm/min, which appears to be the highest value among all the cases. Under this burning condition, the net energy input onto the fuel surface is represented by the heat flux, $\dot{q}_s''$ (Fig. 4.5). This term can be estimated based on the flame temperature, T_f using the following expression [18,21]:

$$\dot{q}_s'' = \chi \frac{4\rho_\infty c_{p,air}(T_\infty g(T_f - T_\infty))^{1/2} D^{1/2}}{\pi} \quad , \tag{4.6}$$

where ρ_∞ is the density of the air at ambient temperature, $c_{p,air}$ is the specific heat at constant pressure and ambient temperature for air, g is the acceleration of gravity ($g = 9.81$ m/s^2), T_f is the average flame temperature ($T_f \approx 1100$ K [99]), D is the diameter of the pool. Importantly, χ represents the fraction of the total heat release that is fed back to the fuel surface, which has a small value in the order of 10^{-3}. By placing a copper rod between the flame and liquid layers, the expectation was to observe an enhancement to the total energy input $\dot{q}_s''$. However, when a 10 mm diameter copper rod is immersed into the dodecane and water layers, the regression rate reduces to 0.47 mm/min, which is a 22% reduction to the baseline no rod condition. As the rod diameter increases to 20 mm, the regression rate continues to fall to 0.43 mm/min, which is a 28% reduction from the baseline. Although thermal energy is transferred from the immersed rod surface into the dodecane layer, most of the energy is lost into the water layer. From a heat transfer standpoint, the boiling heat transfer coefficient (> 1000 W/m^{2}K) is much larger than that of natural convection

($\sim$100 W/m^{2}K) in water [107]. Consequently, the heat transfer into the fuel layer is an order of magnitude lower compared to the heat transfer to the water layer where boiling is observed on the copper rod section immersed in water. Nucleate boiling is observed at the dodecane/water interface for all the no turbulence cases ($u' = 0$ m/s). The water vapor bubbles generated within the control volume rise to the surface and burst, thereby releasing steam into the gas phase, which induces a suppression by water vapor in the flame. This effect is modeled using Quintiere's burning rate model with the inclusion of a suppressant [108]. Note that the water evaporation occurs within the liquid control volume in this study (Fig. 4.5). In Quintiere's model, the water is supplied directly on the surface of the burning material such as water droplets from sprinkler sprays. The water droplets travel through the flame sheet absorbing heat and finally evaporate on the material surface. During such process, the heat of combustion is partially consumed by the latent heat used for water evaporation, which eventually causes the suppression effect on the burning rate. In this study, the water bubble bursting on the pool surface not only releases steam to the gas phase, but also eject micro droplets of fuel into the flame [109,110]. By highspeed observations of the bursting dynamics at the dodecane surface, the micro sprays caused by the bubble bursting occasionally burn in the gas phase, which indicates that the droplets can be either dodecane or water. Compared with the intensive water bubble generation, the micro sprays do not have a noticeable involvement in terms of the enhancement nor suppression of the flame with only one immersed rod. Therefore, the effect of the bursting sprays will not be considered in this study.
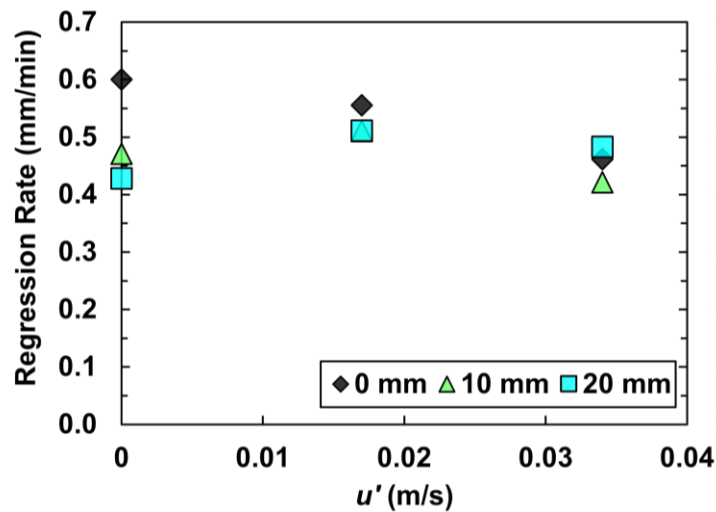
Figure 4. 6: Dodecane layer burning regression rates with 0, 10, 20 mm diameter copper rods as a function of turbulence intensity.

When water layer turbulence intensity increases to $u' = 0.017$ m/s, the dodecane burning regression rate of no rod case ($d_r = 0$ mm) slightly decreases to 0.58 mm/min, which is a 3% reduction from the baseline ($u' = 0$ m/s). It is because the turbulence at the water sublayer continuously replaces the hot water adjacent to the dodecane/water interface with fresh water coming from the tank bottom. The hot water sublayer under the interface that is formed in the no turbulence case can no longer be sustained, therefore the dodecane layer is exposed to a much cooler water sublayer at ambient temperature. As a result, the dodecane layer has a longer burning time with stronger turbulence intensity, and the water sublayer boilover behavior disappears. When the turbulence is increased to $u' = 0.033$ m/s, the regression rate further reduces to 0.52 mm/min. The experimental results of no rod cases are similar to results shown in Chapter 3, where crude oil slicks are burned under different water sublayer turbulence conditions.

For 10 mm copper rod ($d_r = 10$ mm) at turbulence intensity of $u' = 0.017$ m/s, the regression rate decreases to 0.51 mm/min compared with no rod case (0.58 mm/min) at the same turbulence level, but has an increase compared with 10 mm rod/no turbulence case (0.47 mm/min). The reduction is because the rod bottom section will constantly be surrounded by the cool turbulent water sublayer, facilitating heat loss into the bulk water body. Such path of heat lost mechanism is similar to the rods/no turbulence cases, but since there is no nucleate boiling observed under turbulent conditions, the heat loss effect is weaker. For that reason, there is an increase in regression rate compared with the 10 mm rod/no turbulence case. For 20 mm copper rod ($d_r = 20$ mm) at turbulence intensity of $u' = 0.017$ m/s, the regression rate turns out to be identical with the 10 mm rod case. The thicker rod has a larger surface area immersed in both dodecane and water layers, so more surface area will be exposed to cold water sublayer. Despite that, the dodecane layer will receive an increasing amount of external heat from the hot rod surface to the fuel layer. The heat loss effect is counteracted because of this external heat term.

As the turbulence intensity increases at $u' = 0.033$ m/s, the regression rates of 10 mm and 20 mm rod reduce further compared with $u' = 0.017$ m/s turbulence case at 0.51 mm/min (Fig 4.6). The 10 mm rod case has a more significant decrease to 0.42 mm/min, while the 20 mm rod case only reduces to 0.48 mm/min, which indicates the heating effects to the dodecane layer is more dominant than the heat loss effect as the copper rod gets larger. In addition, the larger rod is more capable of collecting heat from the flame zone, so it is less sensitive to the negative impact of the

stronger turbulence intensity. For the no rod burning case, the regression rate decreases to 0.46 mm/min which becomes lower than the 20 mm rod case (0.48 mm/min). This indicates that the thicker rod is acting positively in terms of the burning speed under the high turbulence condition, and it can effectively sustain the temperature of the fuel layer despite the turbulent convective loss increases in the water sublayer.

4.4.2 Flame Height of Dodecane

Figure 4.7 shows the flame height history for all the dodecane burning conditions. During an initial heating stage, the flame height constantly increases. After a pre-heating stage, the flame height is maintained at a nearly constant value until it starts to decrease towards the end of the burning. The three stages are mark by dashed lines in Figure 4.7. For all the experiments, the fuel slick burning is a transient process because of the regressing fuel thickness. However, a steady burning stage can be reasonably assumed for all the cases between the pre-heating stage and decaying stage, which corresponds to 130 – 330 seconds for all cases. In the steady burning stage, the fuel layer temperature has established to support a nearly constant burning regression rate. Since the energy input from the flame is determined directly by the thermocouple measurements close to the surface, this steady regression period is therefore beneficial to exam the regression rate formulation.

To obtain the flame height results, a specific MATLAB algorithm is used. Before using the algorithm, the flame height videos need to be edited by adjusting the brightness and contrast, so that only the flame in the image has high light pixels while the background becomes black. This is to avoid the lighting noise that can affect the detection of the real flame height. When the videos are ready, the algorithm works in two steps to output the flame height results. Firstly, a series of images are extracted with a chosen time interval. In this case, the interval is set at 5 seconds for all the burning cases. To do that, the code reads the video and asks to setup a start time and end time for analysis which correspond to the ignition and extinction time. Then, the region of interest needs to be identified by directly dragging the window frame on the video image. The whole flaming area should be included in this region for accuracy and the bottom of the frame should be at the pool surface. The series of flame images from the time of fire start to the end with a 5-second interval will be output to be used for the next measurement part. The second part of algorithm reads each flame image and binarizes it into black and white format. Since the videos are edited

previously, after binarization, the flame area will be clear and precise for measurement. Next, the code begins to detect the flame tip starting from the top of the interests of region. The conventional way is to measure from the bottom of the frame. However, the horizontal parts of the copper rod's holding structure will cover up the flame area and cause a breakage of the flame area, which leads to the inaccurate detection of the real flame height. To avoid this, the flame height detection now begins from the top. Each pixel distance is calibrated using the measuring tape attached to the front of the water tank. Each extracted flame image will go through this process to yield the flame height data at the corresponding timestamp. Finally, the flame height data of the series images across the burning process is obtained.
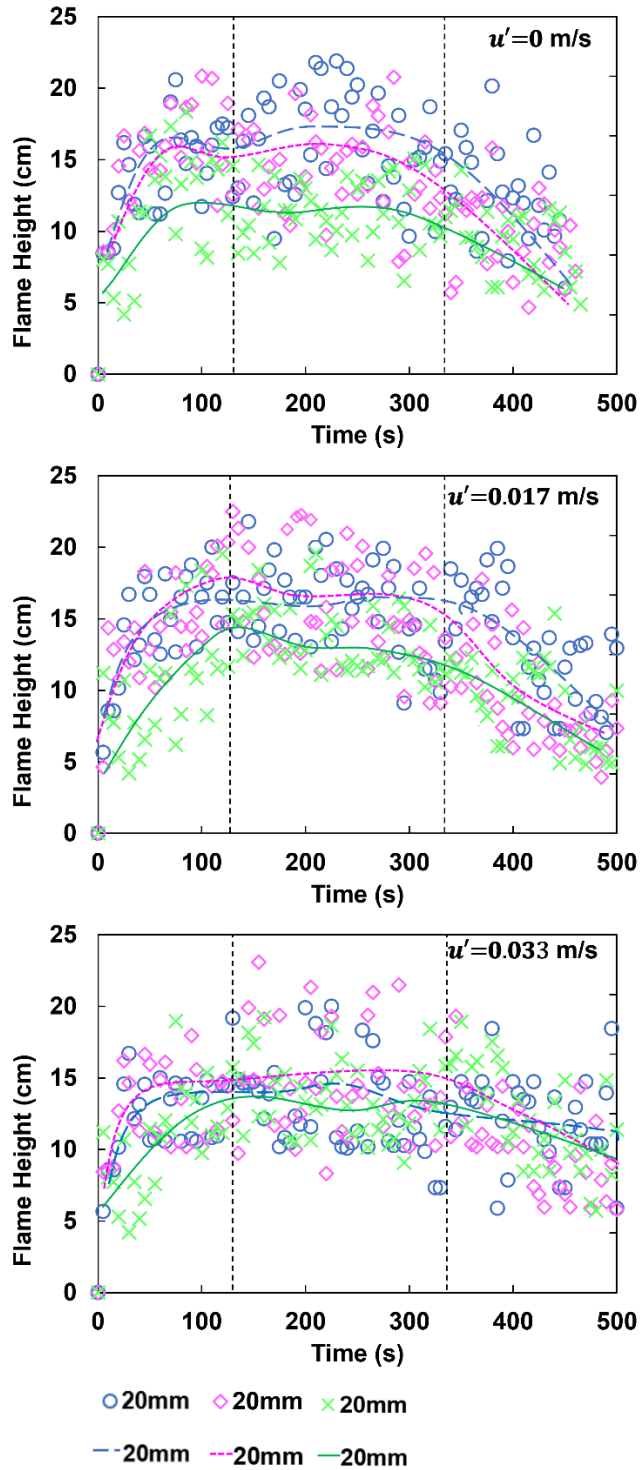
Figure 4. 7: Flame height for dodecane layer burning experiments.

When the dodecane layer is burning without any copper rod ($d = 0$ mm), the flame height decreases with higher turbulence intensity in the water sublayer. Across all the cases, the highest

turbulence conditions ($u' = 0.033$ m/s) have lower flame heights, which is caused by the increasing turbulent cooling effects at the fuel/water interface and the rod bottom section. For no turbulence cases ($u' = 0$ m/s), the flame height is higher when no rod is used compared to the flame heights with both 10 mm and 20 mm rod cases. This is also where the suppression effects are observed caused by the water bubble nucleation at the rod surface immersed in the water sublayer.

Figure 4.8 shows the snapshots of flame heights for all the experimental configurations at 250 seconds after ignition. This time is chosen because the pre-heating stages for all the experiments have ended and the dodecane layer can be assumed to be burned in a quasi-steady phase. As discussed previously, the flame heights for dodecane in 130 – 330 seconds remain steady, which corresponds to a quasi-steady fuel regression process with a duration of 200 seconds. This time will be compared with the three other characteristic times in the problem: a) thermal penetration time through the fuel layer, b) thermal penetration time through the copper rod and c) bubble departure time. The thermal penetration time can be estimated using $t_p = L^2/\alpha$ where L is the characteristic length scale of the material and α is the thermal diffusivity. For the 20 mm copper rod, the thermal penetration time is longer than the 10 mm rod and can be calculated by $t_{p,c} = \frac{(0.02\ m)^2}{1.17\times10^{-4}\ m^2/s} = 3.4$ s. The thermal diffusivity of dodecane is calculated by $\alpha = \frac{k}{\rho c_p} = \frac{0.2\ \text{W/m·K}}{750\ \text{kg/m}^3 * 2.2\ \text{J/(g·K)}} = 1.2 \times 10^{-7}\ m^2/s$, which leads to the thermal penetration time scale of the 5 mm dodecane layer as $t_{p,d} = \frac{(0.005\ m)^2}{1.2\times10^{-7}\ m^2/s} = 20$ s. Also, the bubble departure and bursting time scales are measured in the order of milliseconds. Based on the time scale analysis above, the fuel regression (~200 s) is an order of magnitude slower and can be assumed to be quasi-steady for the purposes of the energy balance model (Eqn. 4.1 and 4.4).

The no rod cases have higher flames in general (Fig 4.8a), and as the turbulence increases, the flame height keeps decreasing from 18 cm at $u' = 0$ m/s to 15 cm at $u' = 0.033$ m/s. For 10 mm and 20 mm rod cases, the flame height increases at $u' = 0.017$ m/s compared to the no turbulence condition, which is opposite of no rod case (Fig 4.8b). This is explained previously and due to water vapor generation when copper rods are used and turbulence is zero. The water vapor not only absorbs heat in the gas phase but also causes higher water concentration in the reaction zone.

This weakens the combustion reaction, and as result, the rod cases yield lower flame height when water bubbles are generated in no turbulence condition.
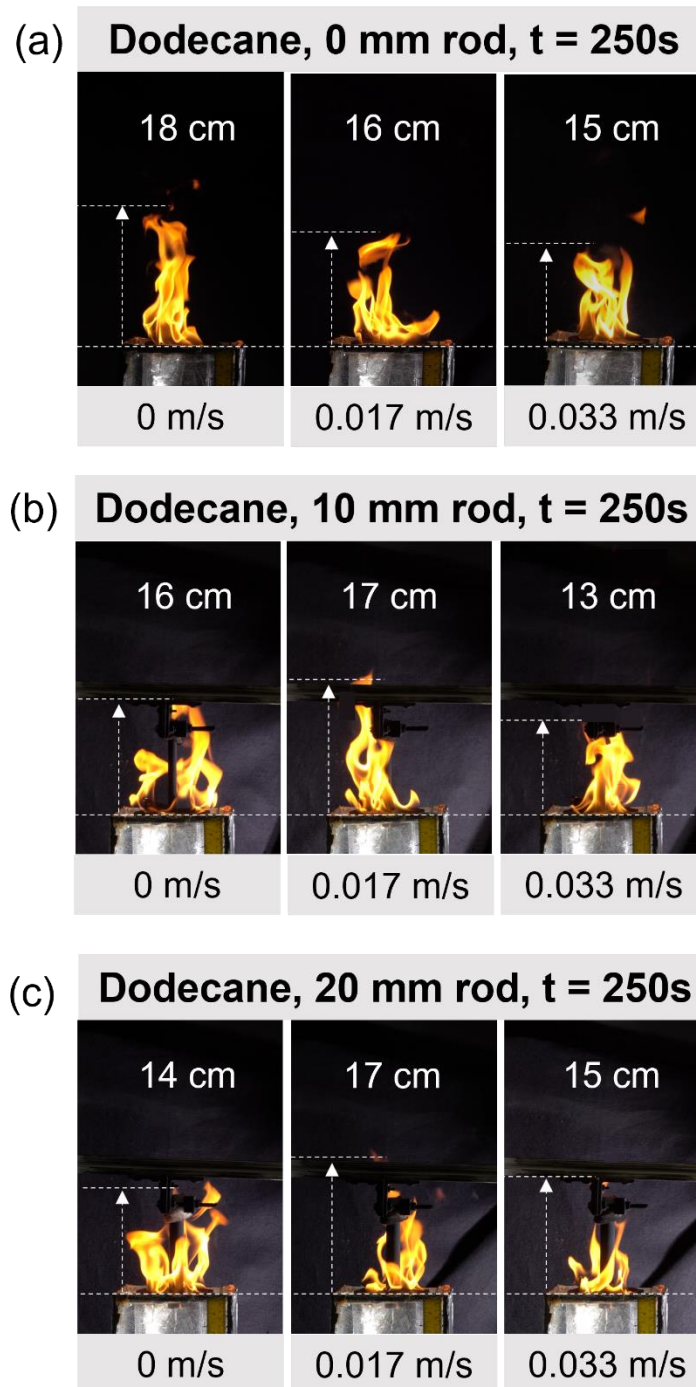
Figure 4. 8: Photographs of dodecane burning flame heights in turbulence intensity of 0, 0.017, 0.033 m/s. (a) No copper rods. (b) 10 mm diameter copper rods. (c) 20 mm diameter copper rod. All the photos are taken 250 seconds after ignition.

Furthermore, the flame shapes of rods cases under no turbulence conditions are different from the other burning configurations. As shown in Figure 4.8b and Figure 4.8c under $u' = 0$ m/s, the flame is pushed away from the rod location and becomes larger in width, while the flames are more concentrated, almost anchored to the rod under turbulent conditions. Again, this flame behavior variation is caused by the water vapor generation on the immersed rod surface. During the nucleation boiling phase, the water bubbles depart from the nucleation sites and will climb upwards along the rod's surface under the force of surface tension, as shown in Figure 4.9. Then, the water bubbles will penetrate the dodecane layer and finally burst at the fuel surface near the rod location. As water vapor being released near the rod region, the flame sheet location starts to move away. Since the flame sheet has the highest flame temperature, the heat-absorbing efficiency will be lower than the case that the flame sheet directly locates at the copper rod surface.
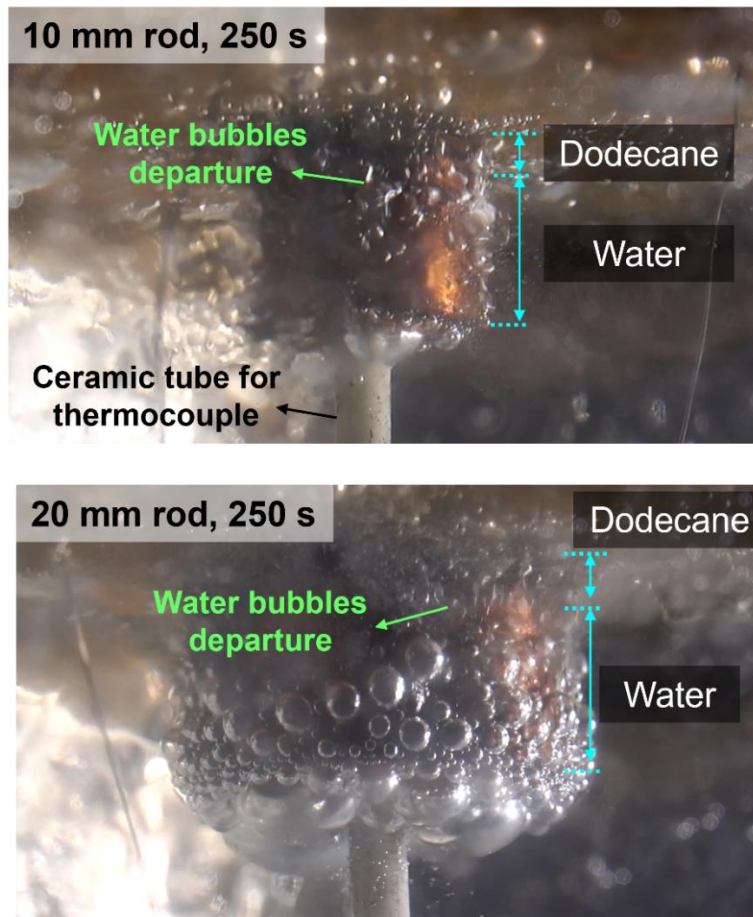
Figure 4. 9: Photograph of nucleate boiling at 250 s on 10 mm and 20 mm copper rod. The departure of water bubbles climbing upwards along the rod's surface.

4.4.3 Temperature profiles in the gas phase, fuel layer, water sublayer and rod

Chapter 3 analyzed the temperature profiles of crude oil slick burning on a turbulent water surface, which has very similar burning conditions and results as the dodecane layer burning without a copper rod. Therefore, the details of no rod cases will not be elaborated on in this section. The 10 mm rod cases share the same bubble behaviors and heat transfer mechanisms. The temperature profile differences between the two rod sizes are minor.

Figure 4.10 shows the temperature profiles of the dodecane layer burning with an immersed 20 mm copper rod immersed. For each experiment, the thermocouple sampling rate was set to 1 Hz, and thermocouple positions are shown in Figure 4.3a. The gas phase and liquid phase temperature data fluctuate because of flame puffing behaviors, bubble dynamics at the interface, and turbulence in the water sublayer. The raw data is averaged every 10 seconds to smooth the final temperature results.
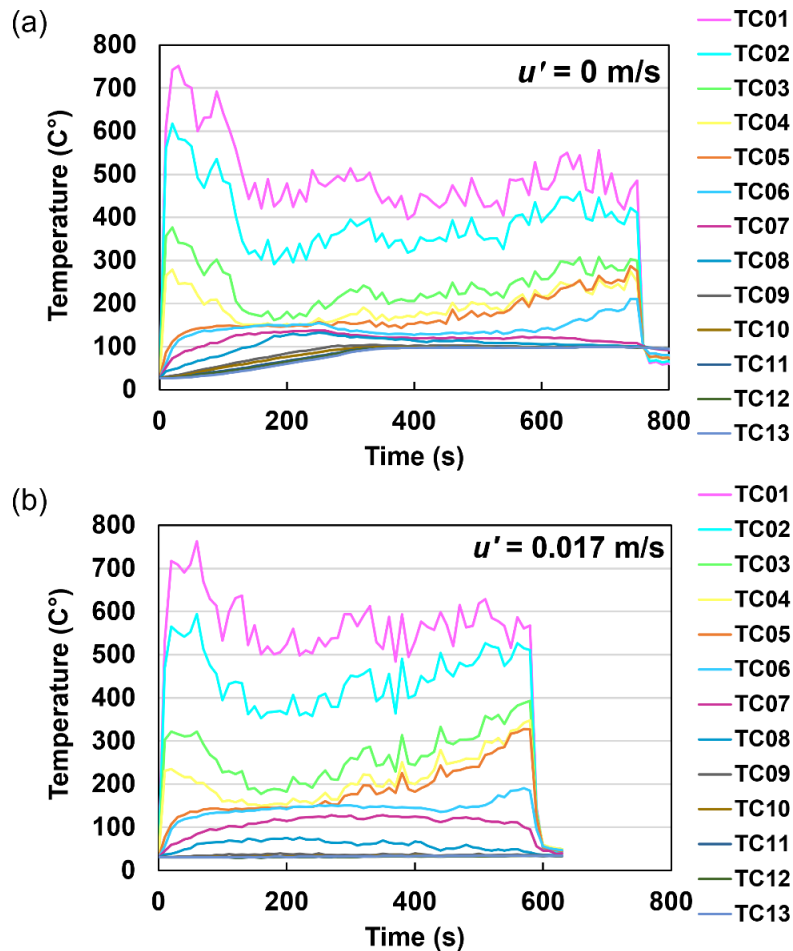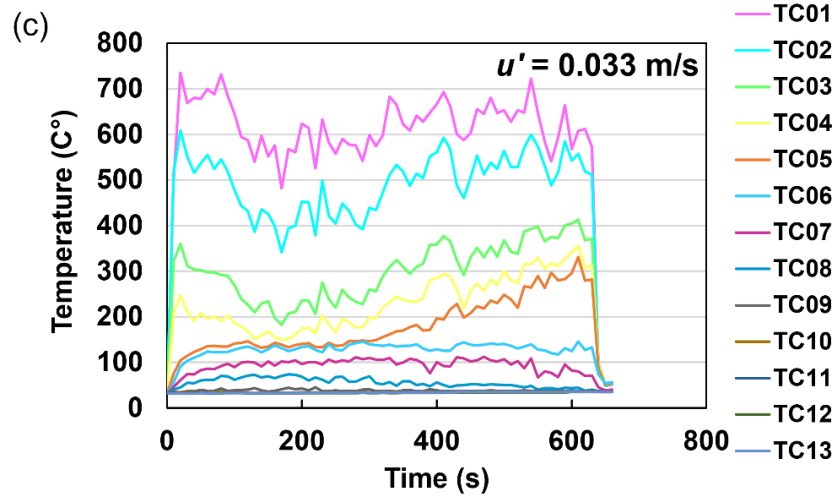
Figure 4. 10: Temperature profiles of dodecane layer burning with 20 mm rod. (a) $u' = 0$ m/s, (b) $u' = 0.017$ m/s, (c) $u' = 0.033$ m/s.

Firstly, some important thermocouple locations can be determined based on the temperature profiles. For instance, the TC05 (orange curves) measures just under the initial dodecane surface, because the reading starts from the ambient temperature and quickly increases to a steady value around 150 °C. After around 300 seconds, the fuel surface regresses to TC05 therefore the temperature begins to rise until it reaches 300 °C, where the thermocouple is in the gas phase region. The TC08 (dark blue curve) measures just above the dodecane/water interface. This can be verified based on Figure 4.10a where boilover occurs and the water sublayer is at super-heated condition just above 100 °C. As a result, TC09 – TC13 is in the water layer and have overlapping readings at 100 °C. While for turbulent cases (Fig 4.10b and 4.10c), the water layer temperature overlaps at ambient temperature (25 °C) because of turbulent mixing.

Secondly, the regression rates can be estimated based on the temperature profiles. The global average regression rate is calculated by the initial dodecane fuel thickness divided by the burning time. From the gas phase temperature profiles, the ignition and extinction time can be easily obtained, which are around 730 s, 590 s, and 620 s for $u' = 0$ m/s, 0.017 m/s, and 0.033 m/s respectively. Besides, a more precise regression rate can be obtained using the time between two adjacent thermocouples moving out of the dodecane surface. For example, according to Figure 4.10 (a), TC05 and TC06 start to be exposed to the gas phase at 390 s and 520 s. It is known that the spacing is 1.2 mm, which can yield a regional regression rate during this time region: $1.2 *$ $60/[(520 - 390)] = 0.55$ mm/min. Compared with the global average of 0.52 mm/min, this

83

regional regression rate is higher. This is because the selected time region is at the middle of the burning process, while the global average regression rate includes the pre-heating stage at the beginning, where the regression rate is low.

Lastly, there is a clear difference in the fuel/water interface temperature under different turbulence intensities. For no turbulence case, the interface temperature reaches 124 °C at 190 s (Fig. 4.10a). This interface creates the condition for the onset of boilover and follows results reported by Torero et al. [21]. For turbulence intensity $u' = 0.017$ m/s and 0.033 m/s, the interface temperature drops to around 75 °C and 67 °C respectively. Hence boilover is not observed when the water layer is made turbulent and heat loss is facilitated because of convection under the interface.

Figure 4.11 shows the temperature profiles measured at location D (Fig. 4.3a), where the thermocouple is inserted into the center axis of the copper rods through the bottom. The vertical distance between the rod's bottom and the measuring location as mentioned previously is 12 mm, which is right above the fuel/water interface within the dodecane layer. Being the only interior temperature measurement point inside the rod, it offers the chance to study the rod's behavior in-depth especially around the area in contact with fuel. For both 10 mm and 20 mm rods, the temperature of the rod body in the immersed section decreases as the turbulence intensity u' being turned up. For $u' = 0$ m/s, the peak temperature reaches over 123 °C for 10 mm rod and 147 °C for 20 mm rod. For $u' = 0.017$ m/s and 0.033 m/s, the peak temperature of 10 mm rod decreases to 118 °C and 113 °C respectively. For 20 mm rod, the temperature peaks are also reduced to 134 °C and 130 °C correspondingly. It is noticed that the turbulence cooling from the water sublayer can effectively bring down the rod body temperature while the thicker 20 mm rod will retain at a higher temperature level than the 10 mm rod.
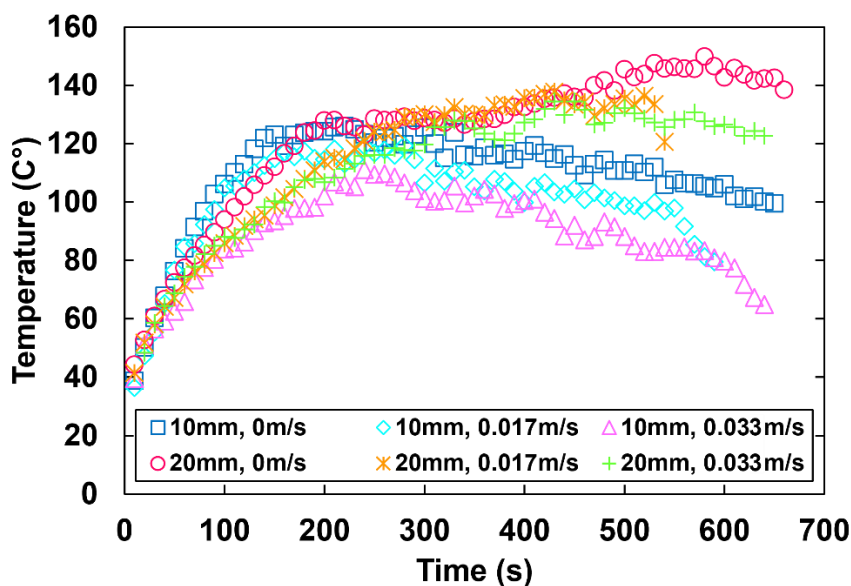
Figure 4. 11: Temperature profiles of rod center in the dodecane layer (thermocouple D).

Figure 4.11 shows that the time taken to reach the maximum temperature for the 10 mm rod is shorter than 20 mm, and for each rod diameter, this preheating time increases with higher turbulence. The shortest preheating time for 10 mm rod is when $u' = 0$ m/s where it takes 140 seconds to reach the peak temperature and the longest time is when $u' = 0.033$ m/s where the time is 230 seconds. After the peak temperature, the 10 mm rod is not able to hold at the highest temperature so a slowly temperature drop is observed for all turbulence conditions till the end of the burning. For the 20 mm rod, the thermal behaviors are quite different, where the preheating time is longer at 210 s, 260 s and 310 s for the three u' conditions. Most importantly, the rod temperature will keep increasing slowly after the preheating stage. This means the thicker rod reacts much less sensitively under the cooling effects of the turbulence. The 20 mm rod has much larger volume/surface ratio compared with the 10 mm rod. Since the convective cooling only occurs on the surface, the much larger thermal capacity of the thick rod ensures the temperature at a high level instead of descending slowly.

4.4.4 Burning Rate Formulation

The following will include two regression rate models which are used to formulate the burning rate based on the discussion of Section 4.3. The two models are the surface energy balance model

for no rod cases (Eqn. 4.1) and the control volume energy balance model for rod cases (Eqn. (4.4)). For each burning configuration, the energy terms in the burning rate model will be modified to match the experimental observations. Especially for the rod cases, the nucleate boiling location highly depends on the fuel type and different turbulence conditions.

4.4.4.1 Case 1: Dodecane Burning with no Rods Conditions (Baseline)

Energy balance at dodecane surface: $\dot{m}_F L_F = \dot{q}_s - \dot{q}_{cond}$ (Eqn. 4.1) is used to obtain regression rates for no rod cases based on the thermocouple measurements near the gas/fuel interface: $\dot{q}_s'' = k_{air}(dT/dy)_{y=0+}$ and $\dot{q}_{cond}'' = k_{fuel}(dT/dy)_{y=0-}$ [106]. The temperature data used for the model are selected within $230 - 270$ seconds after ignition, where the temperature in the dodecane layer is flat showing approximate quasi-steady burning behavior.
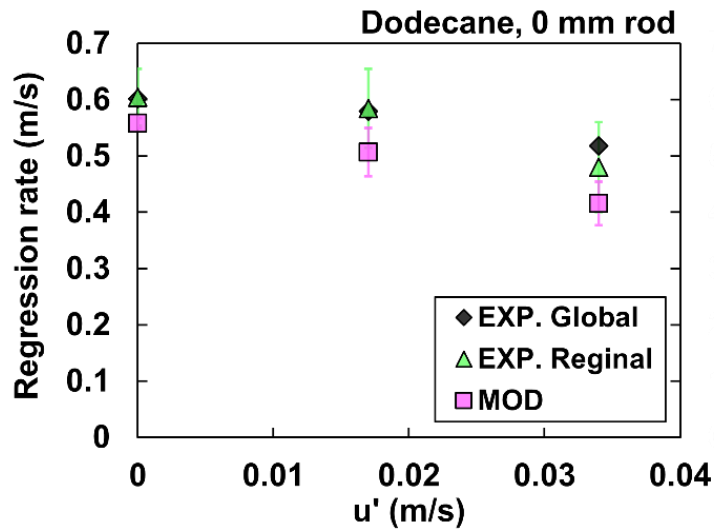
Figure 4. 12: Dodecane burning regression rate results from the surface energy balance model and experimental results for global average and regional average.

Figure 4.12 shows the comparisons between model results and experimental results. The experimental results have two parts: global average regression rate and regional average regression rate. The regional average regression rate is obtained as discussed in Section 4.4.3 by the surface moving speed between thermocouples, and usually occurs in the middle of the burning process. The results from the model (Eqn. 4.1) match reasonably well with the experimental results. The trend of the regression rate with different turbulence intensities and related causing mechanisms have been discussed in detail in previous section and will not be repeated here.

4.4.4.2 Case 2: Dodecane Burning with Rods and no Turbulence Conditions

The control volume energy balance from Equation 4.4 is modified as:

$$(\dot{m}_{W,rod} + \dot{m}_{W,int})L_W = \dot{q}_s + \dot{q}_{e,rod} - \dot{m}_{F,surf}L_F \quad , \tag{4.6}$$

Where $\dot{m}_{W,rod}$ is the water vapor mass generation rate on the rod's surface. $\dot{m}_{W,rod}L_W$ is the energy consumption rate used to convert water to steam at the fuel/water interface within the control volume. $\dot{q}_s = A_F k_{air}(dT/dy)_{y=0+}$ (Eqn. 4.5). $\dot{q}_{e,rod} = A_{rod}k_{copper}(dT/dy)_{A\to B}$ measured by the thermocouple A and B fixed on the rod (Fig 4.2a). $\dot{q}_{loss}$ can be neglected in this burning configuration because the water layer under the control volume quickly develops to the boiling point of water (Fig. 4.10 (a)). Hence conduction loss from the control volume to the water ambient can be assumed to be ignored as energy is used by latent heat transfer of water to steam. $\dot{m}_{F,surf}L_F$ is the energy absorption rate used to vaporize fuel at the surface and can be expressed by: $\dot{m}_{F,surf}L_F = A_F\rho_F r(t)L_F$. As mentioned earlier, L_F and L_W equal to the latent heat of vaporization of fuel and water respectively. The control volume for this burning configuration is shown in Figure 4.13. This control volume is appropriate for dodecane burning with the rod in still water condition because the water sublayer is constant at boiling point (isothermal) which means all the energy transferred to the liquids are used for water bubble generation and fuel evaporation.
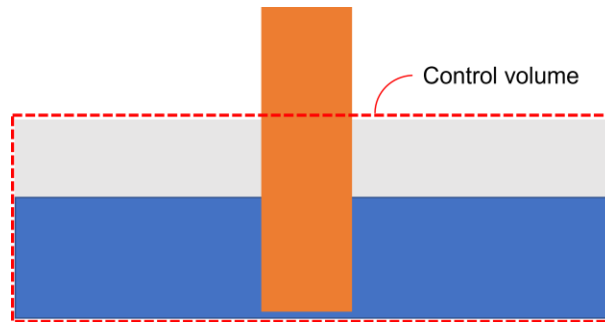
Figure 4. 13: Control volume for dodecane layer burning energy balance with copper rod in still water sublayer.

As mentioned in Section 4.3, the energy terms $\dot{q}_s$ and $\dot{q}_{e,rod}$ can be obtained by thermocouple measurements. However, the water vapor mass generation rate $\dot{m}_{W,rod}$ and $\dot{m}_{W,int}$ can only be obtained by bubble counting using highspeed videography, since the latent heat transfer cannot be

directly measured. From the model described by Equation 4.6, a calculated water application mass flux, $\dot{m}_W''$ on the pool area can be obtained and will be compared with experimental results.

For $\dot{m}_{W,rod}$ measurement, the highspeed video camera is set at 2873 FPS observing at the rod surface with a resolution of 800×600. Figure 4.14a shows the camera viewing position. The distance between the camera and the rod surface (~ 200 mm) is much larger than the rod diameter (10 mm), therefore the total bubble departure frequency on the entire sidewall area can be estimated by two times the measured bubble departure frequency in the front viewing section shown in Figure 4.14b. The bubbles generated at the nucleation sites will quickly merge into bubbles large enough to overcome surface tension holding force upon departure, and the number of the upwards-moving bubbles are counted when they reach the fuel/water interface in 600 continuous frames. 600 frames correspond to 0.21 s with 2873 FPS. Then, the number of counted bubbles is multiplied by 4.76 ($1\ s/0.21\ s$) to yield the bubble departure number during 1 second, which is the departure frequency in the unit of Hz. This bubble measurement is obtained at 250 s after ignition, which is following the thermocouple measurements in this steady burning region. Figure 4.14c shows a photo strip at a time interval of 18 ms (50 frames). Each bubble departure is numbered as it is approaching the fuel/water interface to demonstrate the counting process. During the 150 frames period, 4 bubbles have entered the upper surface. Note that 600 frames are used for measurement and Figure 4.14c is only for bubble movement demonstration.
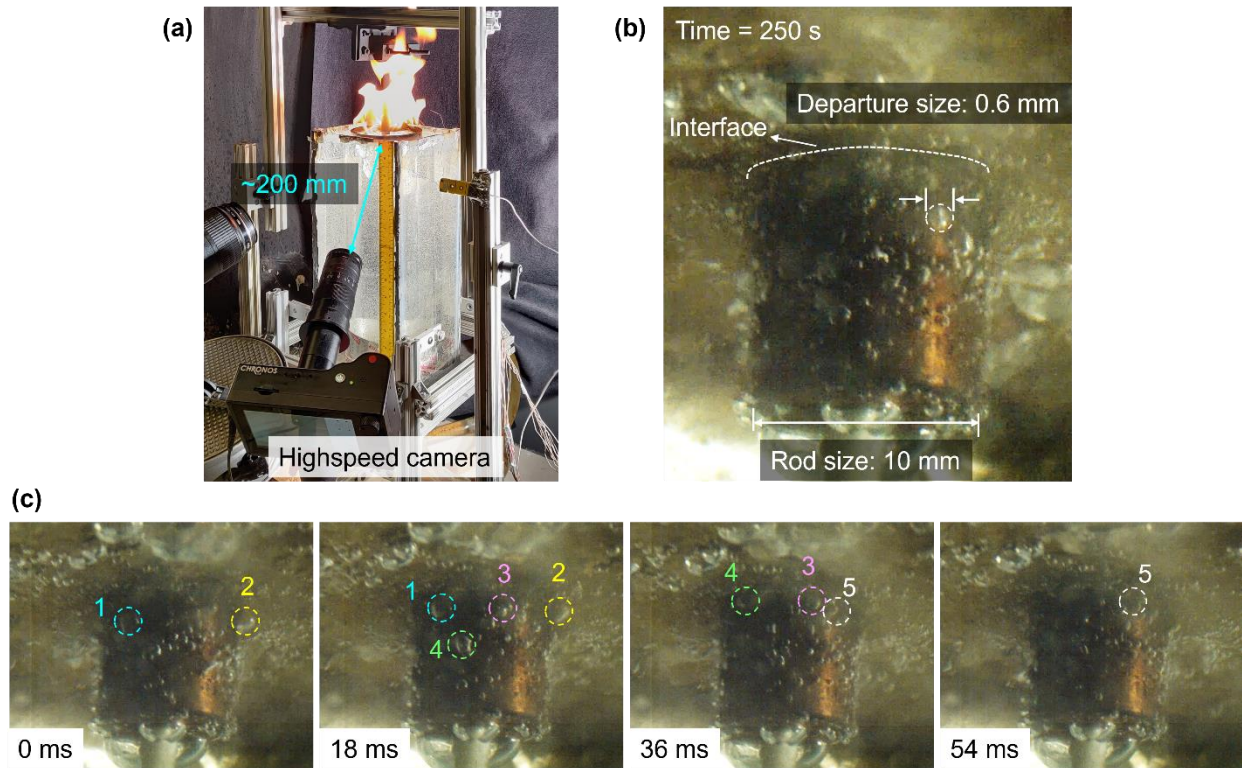
Figure 4. 14: Bubble measurement of water nucleation boiling on the 10 mm copper rod. (a) Highspeed camera viewing angle. (b) Highspeed video clip for the nucleate boiling on 10 mm copper rod at 250 s. (c) Photo strip of bubble movement tracking in 18 ms interval at 250 s.

Figure 4.15a shows the camera viewing position to measure $\dot{m}_{W,int}$. The highspeed video is set to 1057 FPS at the resolution of 1280×1026 because the bubble bursting rate and overall dynamics are slower on the pool surface, and it requires a wider recording frame to include the entire pool area. Similar to the $\dot{m}_{W,rod}$ bubble counting technique, the number of large bubbles bursting on the fuel surface is counted for 500 frames (corresponding to ~0.5 s). Then the number is multiplied by 2 (1 s/ 0.5 s) to obtain the boilover bubble bursting frequency during 1 second (Hz). For both bubble countings on the rod's surface and furl/water interface, three measurements are taken with 10 seconds interval in the quasi-steady burning period to obtained the averaged final results. Figure 4.15b shows the dome-shaped bubbles before bursting. The water bubble almost has the same diameter as the 10 mm copper rod, and each bubble originates at the fuel/water interface. As the water sublayer reaches the boiling temperature, nucleation at the interface begins to occur. The water vapor initially forms a small gas pocket at the interface and lifts off when the bubble volume grows large enough to overcome the surface tension. During this period, the nucleate boiling is violent at the fuel/water interface. Note than the dodecane surface does not undergo an explosive

burning condition which is referred to as thin layer boilover [19]. This is because the onset of water vapor formation occurs quite early at around 230 seconds, because of the additional heat transfer from the rod. The total burning time is over 600 seconds. Therefore, the dodecane layer is still thick and the bubble bursting on the fuel surface cannot effectively eject the entire dodecane layer into the gas phase as it does to the thin dodecane film during boilover [19].
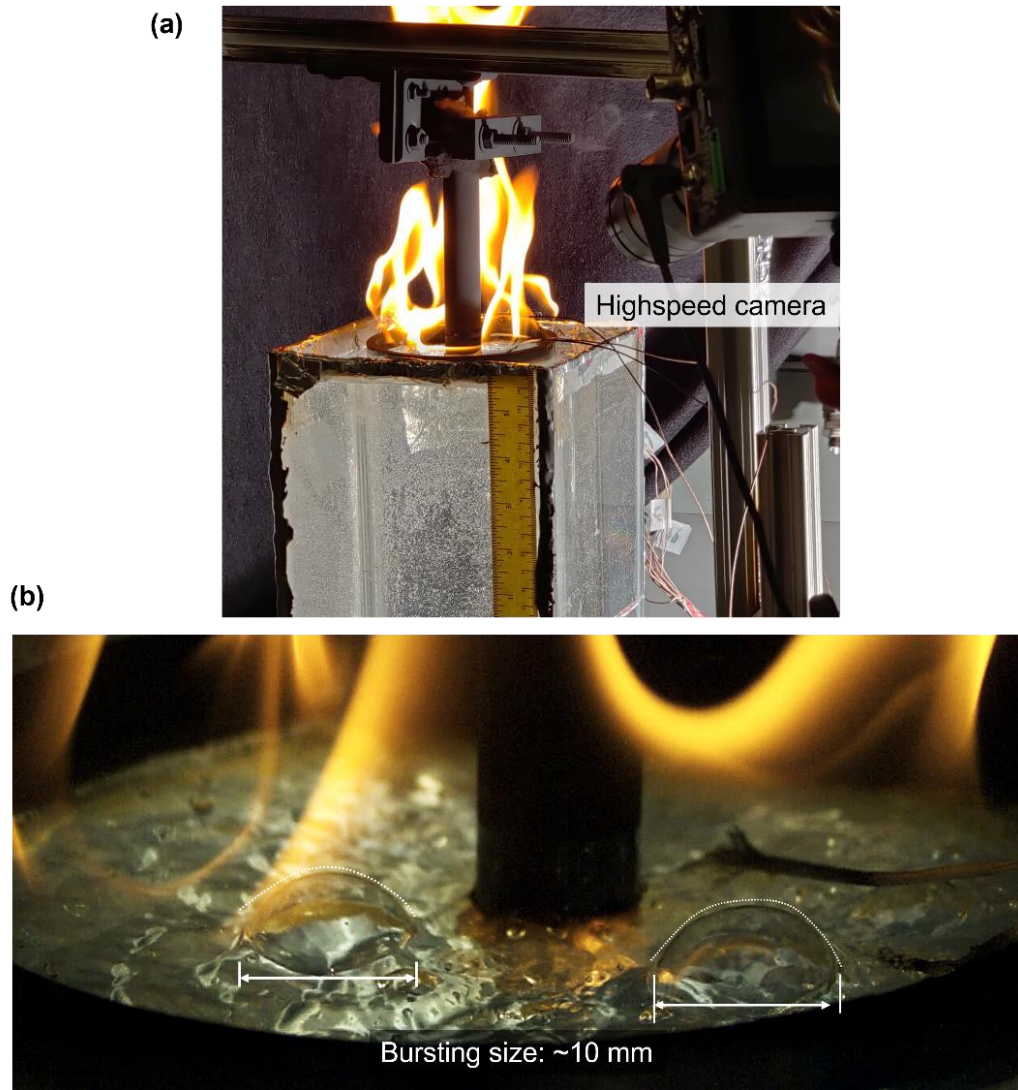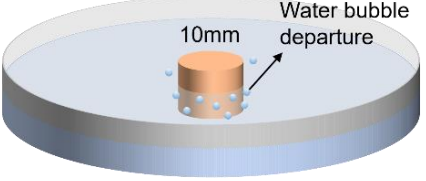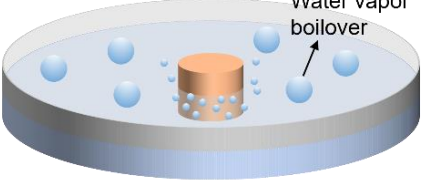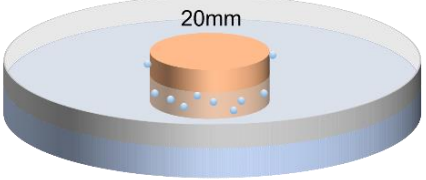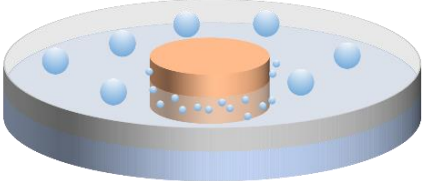
Figure 4. 15: Bubble measurement of large water bubbles at the pool surface caused by boilover. Water vapor bubbles formed at the fuel/water interface. (a) Highspeed camera viewing position. (b) Highspeed video clip for the bubble size before bursting during boilover with 10 mm copper rod at 250 s.

Table 4.2 shows the bubble counting results of 10 mm and 20 mm immersed rod cases under no turbulence conditions. The schematics illustrate bubble nucleation areas and corresponding

bursting size, where the small water bubbles with a diameter around 0.6 mm are generated on the rod's sidewall and large water bubbles with a diameter of 10 mm are generated on the interface of the liquids. Water vapor bubble generation at the interface of fuel and water occurs later than the onset of nucleate boiling on the rod's surface. As shown in Table 4.2. For a 10 mm rod, the onset time to nucleate boiling on the rod is 140 s which is shorter than the 20 mm rod case of 180 s. This is because the 20 mm rod has a larger volume so that the total heat capacity is larger. It requires longer to heat the rod body and bring the temperature difference between the hot surface and water boiling point sufficient for nucleate boiling. However, when the onset of nucleate boiling on the rod has been reached, the time to generation of water vapor bubbles at the dodecane/water interface is shorter with 20 mm rod, which is $235 - 180 = 55$ seconds compared with 10 mm rod of $230 - 140 = 90$ seconds. The shorter time difference between the onset of two scenarios in the 20 mm rod case is caused by the larger rod immersed area, where the high surface heat flux during the boiling process can heat the water sublayer more efficiently.

The departure frequency of each bubble condition is also recorded. This value is used in calculating the water vapor mass generation rate $\dot{m}_{W,rod}$ and $\dot{m}_{W,int}$. The bubble departure frequency measurement results shown in Table 4.2 represent the number of bubbles leaving the rod's surface and pool surface in a time duration of 1 second. At the onset of nucleate boiling on the rod, the departure frequency is comparatively low at 40 Hz at 140 s with 10 mm rod and 100 Hz at 180 s with 20 mm rod. When water vapor bubbling occurs at the fuel/water interface, after around 230 seconds, the frequency becomes steady at 80 Hz for 10 mm rod and 500 Hz for 20 mm rod. At this time, the water bubble (from the fuel/water interface) bursting frequency can be measured at 100 Hz for 10 mm rod and 120 Hz rod 20 mm rod. It is noticeable that small bubbles on the rod are generated at a much higher rate for 20 mm rod compared to 10 mm rod (400 % increase), while the bursting rate of large bubbles on the pool surface does not change too much (20 % increase). This is because the bubble counting area for small bubbles increases to 4 times when the diameter doubles. The pool surface, however, will have a slightly smaller surface area. Therefore, even though a thicker rod has a higher heating capability to the water sublayer, the boilover intensity is not enhanced significantly.

Table 4. 2: Bubble measurement results for dodecane layer burning with copper rods under no turbulence condition.

Schematic of dodecane layer burning	Time to onset (seconds)	Departure size (mm)	Departure frequency (Hz)	Boilover bubble size (mm)	Boilover frequency (Hz)
	140	0.6	40	NA	NA
	230	0.6	80	10	100
	180	0.6	100	NA	NA
	235	0.6	500	10	120

According to the water vapor bubble observation mentioned above, a considerable part of the energy input to the immersed rod section is lost to the water to vapor latent energy transition process. The dodecane layer burning regression rate, thus, decreases as copper rod size gets larger under no turbulence burning conditions (Fig 4.6). This suppression effect by water introduced by the immersed copper rod appears to be similar to applying water to a burning surface since the fundamental heat removal mechanism is identical to water evaporation.

Table 4. 3: Modeling and experimental results of water mass flux on the pool surface.

Dodecane layer burning configuration	Model result of $\dot{m}_W''$ (g/m²s)	Experimental result of $\dot{m}_W''$ (g/m²s)
10 mm rod, $u' = 0$ m/s	4.20	3.95
20 mm rod, $u' = 0$ m/s	4.82	4.89

The data in Table 4.3 show the comparisons of modeling results of water mass flux versus the experimental results based on bubble counting. The water mass flux is calculated by:

$$\dot{m}_W'' = \frac{\dot{m}_{W,rod} + \dot{m}_{W,int}}{A_F} \quad , \tag{4.7}$$

where A_F is the fuel surface area (pool surface minus the cross-section area of the rod). Thus, the mass flux represents the total water generation rate with respect to the entire fuel surface. The model results of $(\dot{m}_{W,rod} + \dot{m}_{W,int})$ are obtained using energy balance formulation expressed by Equation (4.6). The model results turn out to match well with experiments, where the water mass flux for 10 mm rod under no turbulence burning condition is around 4 g/m²s and 4.8 g/m²s for 20 mm rod. The additional 0.8 g/m²s of water causes the regression rate decrease from 0.47 mm/min to 0.43 mm/min (Fig 4.6) and the flame height reduction from 16 cm to 14 cm (Fig 4.7). Tewarson [111] reported a water application rate per unit surface area of the dodecane at flame extinction condition of 12 g/m²s. The water mass flux in this study can suppress the dodecane layer burning but is still far from the extinction threshold.

4.4.4.3 Case 3: Dodecane Burning with Rods and Turbulence Conditions

Under turbulence conditions, the nucleate boiling in the water layer is no longer observed. The suppression effects because of the water bubble generation hence stops. As a result, the heat loss transfer mechanism to the water sublayer is altered because the rod bottom now is cooled by the convection in water instead of the nucleate boiling. To capture the convective heat loss at the fuel/water interface and rod's bottom area, the control volume is changed to the shape as shown in Figure 4.16.
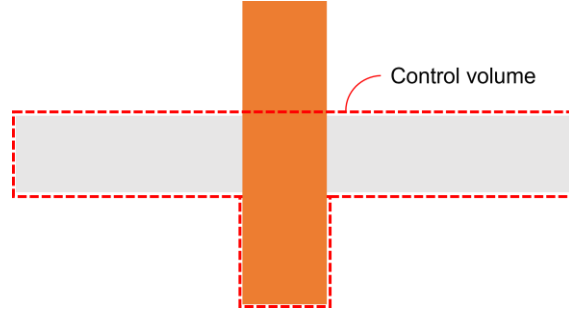
Figure 4. 16: Control volume for fuel layer burning energy balance with copper rod in turbulence condition.

The control volume energy balance from Equation 4.4 is modified as:

$$\dot{m}_F L_F = \dot{q}_s + \dot{q}_{e,rod} - \dot{q}_{loss,int} - \dot{q}_{loss,rod} \quad , \tag{4.7}$$

Two heat loss terms are added to the energy balance, where $\dot{q}_{loss,int}$ is the heat loss at the fuel/water interface because of the convective cooling effects and calculated using the thermocouple measurements at the water sublayer:

$$\dot{q}_{loss,int} = A_F h_{int}(T_{int} - T_\infty) \quad , \tag{4.8}$$

where T_{int} denotes the temperature at the fuel/water interface, and T_∞ is the ambient temperature of the water. The convective heat transfer coefficient at the fuel/water interface has been obtained in Chapter 3. Since the water sublayer is made turbulent using the identical system and conditions, the convective heat transfer coefficient at the fuel/water interface, h_{int} can be adopted from the results from Chapter 3. Additionally, heat loss also occurs at the rod bottom section. $\dot{q}_{loss,rod}$ can be expressed by:

$$\dot{q}_{loss,rod} = A_{rod,W} h_{rod}(T_{R,C} - T_\infty) \quad , \tag{4.9}$$

Where $A_{rod,W}$ is total area of the section area contacting with the water layer as shown by Figure 4.17. $T_{R,C}$ represents the rod temperature in the water layer and experimentally measured using the thermocouple on the rod affixed at location "C" shown in Figure 4.3. The energy input through the copper rod cross-section area can be written as:

$$\dot{q}_{e,rod} = A_{rod} k_{copper} \left(\frac{T_{R,A} - T_{R,B}}{S_{AB}} \right) \qquad (4.10)$$

The measurement locations to quantify $\dot{q}_{e,rod}$ are both on the rod surface and since the temperature difference is much more significant in vertical direction compared with radial direction because of the high thermal conductivity of copper, the surface measurements can provide good estimations of heat input through the rod.
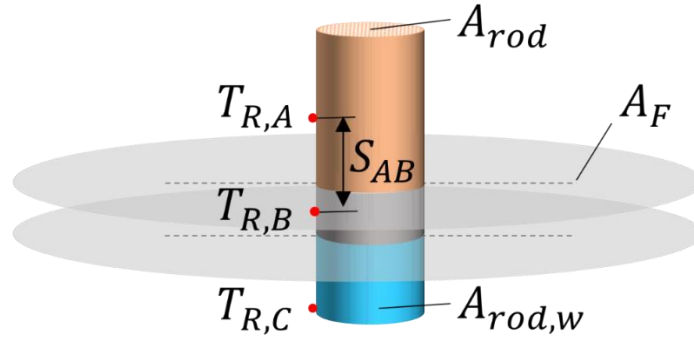
Figure 4. 17: Schematic of thermocouple measurement locations on the copper rod and areas for energy terms calculation.

Now, the only unknown parameter is the convective heat transfer coefficient at the rod surface in water, h_{rod}. The value of h_{int} mentioned above cannot be used for h_{rod}, because the h_{rod} should represent a hot cylinder in flow conditions while h_{int} is only valid for the convection at the horizontal liquid layers. To estimate the h_{rod}, the Nusselt number correlation for a circular cylinder in forced liquid convection by Churchill et al. [112] is used:

$$Nu_D = 0.3 + \frac{0.62 Re_D^{1/2} Pr^{1/3}}{[1 + (0.4/Pr)^{2/3}]^{1/4}} \left[1 + \left(\frac{Re_D}{282,000} \right)^{5/8} \right]^{4/5}, \qquad (4.11)$$

This single comprehensive equation covers the entire range of Re_D and a wide range of Pr, which is suitable for all $Re_D\, Pr \geq 0.2$. Table 4.4 shows the calculated convective heat transfer coefficient on the bottom rod surface, h_{rod}:

Table 4. 4: Convective heat transfer coefficient on the bottom rod surface, h_{rod}.

Configurations	u' [m/s]	D [m]	Re_D	Nu_D	h_{rod} [W/m²]
10 mm 0.017 m/s	0.017	0.01	217.9	15.54	964
10 mm 0.034 m/s	0.034	0.01	435.9	21.96	1362
20 mm 0.017 m/s	0.017	0.02	435.9	21.96	681
20 mm 0.034 m/s	0.034	0.02	871.8	31.16	966

The Reynolds number Re_D for the cylinder is calculated as $Re_D = \frac{u'D}{v}$ and h_{rod} is calculated by $h_{rod} = \frac{Nu_D k_W}{D}$. Since the convection fluid is water, the kinematic viscosity of water, v is 7.8×10^{-7} m²/s and the thermal conductivity of water, k_W is 0.62 W/m-K. To further validate the calculated h_{rod} values, the nucleate boiling curves of the hot wire experiments from Chapter 2 are used. Since the thin wire is cylindrical in shape and before the onset of nucleate boiling, the thin wire is cooled by pure convection. For low turbulence intensity, the average convective heat transfer coefficient around the hot wire can be calculated as $h_{wire} = \frac{\dot{q}_{ÖNB}}{T_{wire} - T_\infty} = \frac{0.3 \ kW/m^2}{195 \ K} \approx$ 1500 W/m². Hence the calculated values of h_{rod} around 1000 W/m² using Churchill's correlation (Eqn. 4.11) is reasonable.

Table 4.4 shows that when the turbulence RMS velocity u' is doubled, the convective heat transfer coefficient increases by around 40%. This is because the stronger turbulence is more capable of removing heat from the rod surface. Moreover, when the rod diameter is doubled, the coefficient decreases by around 40%. As a larger rod is placed in a flow field, the cooling effect will not be as high as with a smaller rod, because the ratio of volume and cooling surface for a thick rod is more significant. In other words, the larger rod is more thermally inert against the cooling flow, so the heat transfer coefficient is lower.

At this point, all the thermocouple measurement results, property data, and heat transfer coefficients are ready to be substituted into the governing burning rate formulation Equation 4.7,

which will yield a calculated fuel burning rate, $\dot{m}_F$. Table 4.5 shows the calculation process and related values in detail for each burning condition.

Table 4. 5: Calculations of energy terms in the burning rate formulation of dodecane burning with a copper rod in turbulence conditions.

Conditions	$A_F k_{air}\left(\dfrac{dT}{dx}\right)_{y=0+}$	$A_{rod} k_c \dfrac{T_{R,A}-T_{R,B}}{S_{AB}}$	$A_F h_{int}(T_{int}-T_\infty)$	$A_{r,W} h_{rod}(T_{R,C}-T_\infty)$	$\dot{m}_F$
$d = 0.01$ m $u' = 0.017$ m/s	0.007775*0.0469 *100678 =36.71 W	$\left(401\dfrac{37.8}{0.02}\right)\pi(0.005)^2$ =59.52 W	0.007775 * 92(92 − 29.4) =49.60 W	0.000393 * 963 * (82.5 − 29.4) =20.08 W	$\dfrac{36.7 + 59.5 - 49.6 - 20.1}{358 + 2.2(216 - 126)}$ =0.056 g/s EXP average: 0.049 g/s
$d = 0.01$ m $u' = 0.033$ m/s	0.007775*0.0469 *109100 =39.79 W	$\left(401\dfrac{35.7}{0.02}\right)\pi(0.005)^2$ =56.21 W	0.007775 * 126(87.9 − 32.7) =54.08 W	0.000393 * 1362 * (72.4 − 32.7) =21.23 W	$\dfrac{39.8 + 54.5 - 54 - 15.1}{358 + 2.2(216 - 112)}$ =0.035 g/s EXP average: 0.041 g/s
$d = 0.02$ m $u' = 0.017$ m/s	0.00754*0.0469 *99343 =35.13 W	$\left(401\dfrac{11.2}{0.02}\right)\pi(0.01)^2$ =70.55 W	0.00754 * 92(84.9 − 30.7) =37.60 W	0.000942 * 681 * (78.1 − 30.7) =34.79 W	$\dfrac{35.1 + 84.4 - 37.6 - 49.2}{358 + 2.2(216 - 121)}$ =0.059 g/s EXP average: 0.049 g/s
$d = 0.02$ m $u' = 0.033$ m/s	0.00754*0.0469 *112941 =39.9 W	$\left(401\dfrac{10.7}{0.02}\right)\pi(0.01)^2$ =67.40 W	0.00754 * 126(79 − 34.3) =42.47 W	0.000942 * 966 * (71.3 − 34.3) =43.15 W	$\dfrac{39.9 + 75 - 35.3 - 43.2}{358 + 2.2(216 - 114)}$ =0.037g/s EXP average: 0.047 g/s

Results represented in Table 4.5 show that the burning rate results from the proposed formulation agree well with the experimental mass loss measurements. More importantly, the burning rate formulation results follow the same trend with the experimental results when the burning configuration is changed. For instance, the calculated $\dot{m}_F$ decreases with higher turbulence intensity in the water sublayer, and slightly increases with larger copper rod diameter. The calculated dodecane burning rate peaks at 0.059 g/s when 20 mm copper rod is used in low turbulence of $u' = 0.017$ m/s. This also matches with the flame height results (Fig. 4.8) where the larger rod can enhance the burning rate in turbulence conditions and the convection heat loss through the fuel/water interface is low. On the contrary, the lowest burning rate occurs when the thinner rod is placed within the higher turbulence. This is shown in Table 4.4 where the lowest $\dot{m}_F$ of 0.033 g/s is calculated when 10 mm rod is used in high turbulence of $u' = 0.033$ m/s.

Apart from the burning rate results, each energy term included in the governing equation can reveal the fundamental heat transfer characteristics under the effect of both rod size and turbulent intensity. The energy input terms from the gas phase $\dot{q}_s = A_F k_{air} \left(\frac{dT}{dy}\right)_{y=0+}$ have similar values across all the cases, meaning the flame's heating effect is not sensitive to the rod size and turbulence condition in the water sublayer. According to the calculations, higher turbulence leads to a slightly higher gas-phase energy input. This can be explained by the lower flame heights for high turbulence conditions. Since the flame sheet or reaction zone is the hottest location in the gas phase, and with the flame sheet being pulled close to the fuel surface when flame height is reduced, the thermocouples above the surface captured this hot layer shifting. As a result, the gas phase energy input becomes larger at nearly 40 W for $u' = 0.033$ m/s and around 36 W for $u' = 0.017$ m/s.

The energy inputs through the copper rod $\dot{q}_{e,rod} = A_{rod} k_{copper} \left(\frac{T_{R,A} - T_{R,B}}{S_{AB}}\right)$ for 10 mm rod have lower values under 60 W compared with that of 20 mm rod, which is higher at 70 W. This verified the stronger heating capability of the thicker copper rod. Interestingly for 10 mm rod, the temperature difference between $T_{R,A}$ and $T_{R,B}$ is much larger above 30 °C compared with the temperature difference of around 10 °C for the 20 mm rod. This shows that it is more difficult for the larger rod to develop a higher temperature variation vertically because the larger body comes with a larger total thermal capacity which requires more time and energy to build up the temperature difference. However, even though the thinner rod has a higher temperature gradient, the total energy term is still surpassed by the 20 mm rod because of the much larger cross-section area (Table 4.5).

The convective heat loss through the fuel/water interface $\dot{q}_{loss,int} = A_F h_{int}(T_{int} - T_\infty)$ increases with stronger turbulence mostly because of the larger convective heat transfer coefficient of 126 W/m² for $u' = 0.033$ m/s over the lower value of 92 W/m² for $u' = 0.017$ m/s. The other convective heat loss occurs at the rod bottom section and is expressed by $\dot{q}_{loss,rod} = A_{rod,W} h_{rod}(T_{R,C} - T_\infty)$. For 10 mm rod, the heat loss from the copper rod bottom section to the water layer is distinctively smaller around 20 W compared to 20 mm rod cases of 35 W and 43 W respectively for the two turbulence cases. This indicates that the thinner rod is limited in terms of

heat loss through the bottom surface to the water sublayer, so the energy input can be transferred to the fuel layer more effectively. Based on the Spalding B number mass burning equation: $\dot{m}'' = \frac{h}{c_p} \ln(B+1)$ and $B = \frac{Y_{O_2,\infty} \Delta h_c / r - c_p(T_b - T_\infty)}{L}$ [113], it is clear that because the B number is within the logarithm term, the mass burning rate is fairly insensitive to small burning condition changes with the same type of fuel. Therefore, the heat consumed for fuel evaporation at the surface is limited as well. Consequently, the interface temperature T_{int} is measured higher with 10 mm rod at around 90 °C compared with 20 mm rod with T_{int} around 80 °C. The hotter interface temperature means a larger amount of energy loss given the water sublayer is maintained at ambient temperature for all the turbulence cases. This makes sense as the heat loss on the rod bottom and fuel surface are limited, the only path for heat loss is through the fuel/water interface by convection. As a result, the $\dot{q}_{loss,int}$ is larger for 10 mm rod at around 50 W while for the 20 mm rod, it is around 40 W.

4.5 Rod Effects on Heptane Burning

4.5.1 Regression Rate
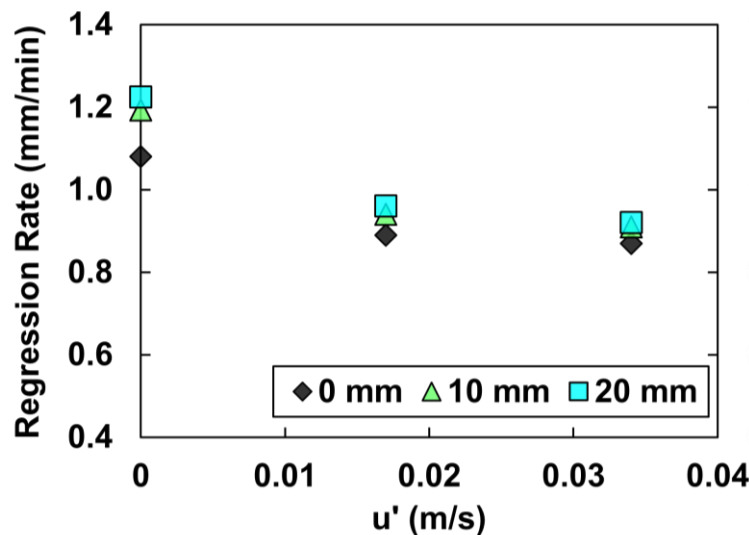
Figure 4. 18: Heptane layer burning regression rates with 0, 10, 20 mm diameter copper rods as a function of turbulence intensity.

Figure 4.18 shows the regression rate of heptane burning with 0, 10, 20 mm copper rods as a function of turbulence intensity. Overall, the regression rate is enhanced when a copper rod is used

for still water sublayer and low turbulence conditions, which is contrary to dodecane cases where the regression rate drops for all the rod cases. When $u' = 0$ m/s, the rod enhancement is the most significant. The no rod case has a regression rate of 1.08 mm/min, and as the rod size is increased to 10 mm and 20 mm, the regression rates are facilitated to 1.19 mm/min and 1.22 mm/min (10% and 13% of increase). As the water sublayer is made turbulent with $u' = 0.017$ m/s, the regression rates for all cases decrease and the rod cases (10 mm and 20 mm) burn at 0.96 and 0.94 mm/min compared with the no rod case, which burns at 0.89 mm/min. When $u' = 0.033$ m/s, the regression rate equals 0.87/0.91/0.92 mm/min (no rod case/10 mm rod/ 20 mm rod). The enhancement for the zero-turbulence case is because of the nucleate boiling observed at the rod's surface. While the 10 mm and 20 mm rod cases still have an enhancement effect on the regression rate, such enhancement decreases with the increase of turbulence intensity.

The bubble formation on the copper rod is different from the dodecane experiments no turbulence, where the nucleate boiling occurs in the water. This change in the location of bubble formation is because of the difference in the boiling points of heptane and dodecane (98 vs. 216 °C). When the onset of nucleate boiling is reached in the heptane layer, the heat and mass transfer increase. The result is that a large amount of heat finds its way into the fuel layer, thus enhancing the regression rate. With a thicker copper rod, this enhancement of heat going into the fuel layer becomes more intensive, so the higher regression rate is achieved.

In turbulence cases, the enhancement of regression rate by placing the copper rod is mitigated, and the copper rod does not noticeably affect the regression rate. The nucleate boiling of heptane on the rod's surface is significantly reduced with turbulence in the water sublayer. This is because the level of superheat provided by the rod is reduced by the change in the boundary condition. In no turbulence condition, the water layer temperature close to the fuel/water interface can be maintained at a high level nearly but not equal to the boiling point of water. As the water is made turbulent, the water sublayer temperature drops to ambient temperature immediately. The heat loss on the rod's bottom surface in contact with water becomes turbulent forced convection, which leads to an increase of energy passing through the rod's body into the water layer. Consequently, the heat cannot be sufficiently built up on the rod's surface in the heptane layer, and nucleate boiling on the rod's surface ceases. When a thicker rod is used, the surface area contacting the

water layer increases so the convective heat loss will also increase. As a result, the regression rates in rod cases eventually become very close to the no rod case under turbulence conditions.

4.5.2 Flame Height

Figure 4.19 shows the flame height measurements for all heptane layer burning conditions. The flame of the heptane pool is generally higher than the dodecane pool fire and similar to the dodecane cases, three different flaming stages are observed and illustrated by the dashed lines: pre-heating stage at 0 – 70 s, steady burning stage at 70 – 225 s, and decaying stage after 225 s. These three stages are present for all the heptane burning cases A time frame of 150 s is used to demonstrate the flame shape, and for selecting thermocouple data used in the burning rate formulations in the following sections. Under the same rod conditions, the flame height decreases as the turbulence in the water sublayer get stronger (Fig. 4.19). This is because of an increase in heat loss through the fuel/water interface and the rod's bottom surface. As lesser heat is available for fuel evaporation, the amount of heptane vapor rising into the flame sheet decreases. Therefore, the flame location descends closer to the pool surface resulting in a lower flame height.
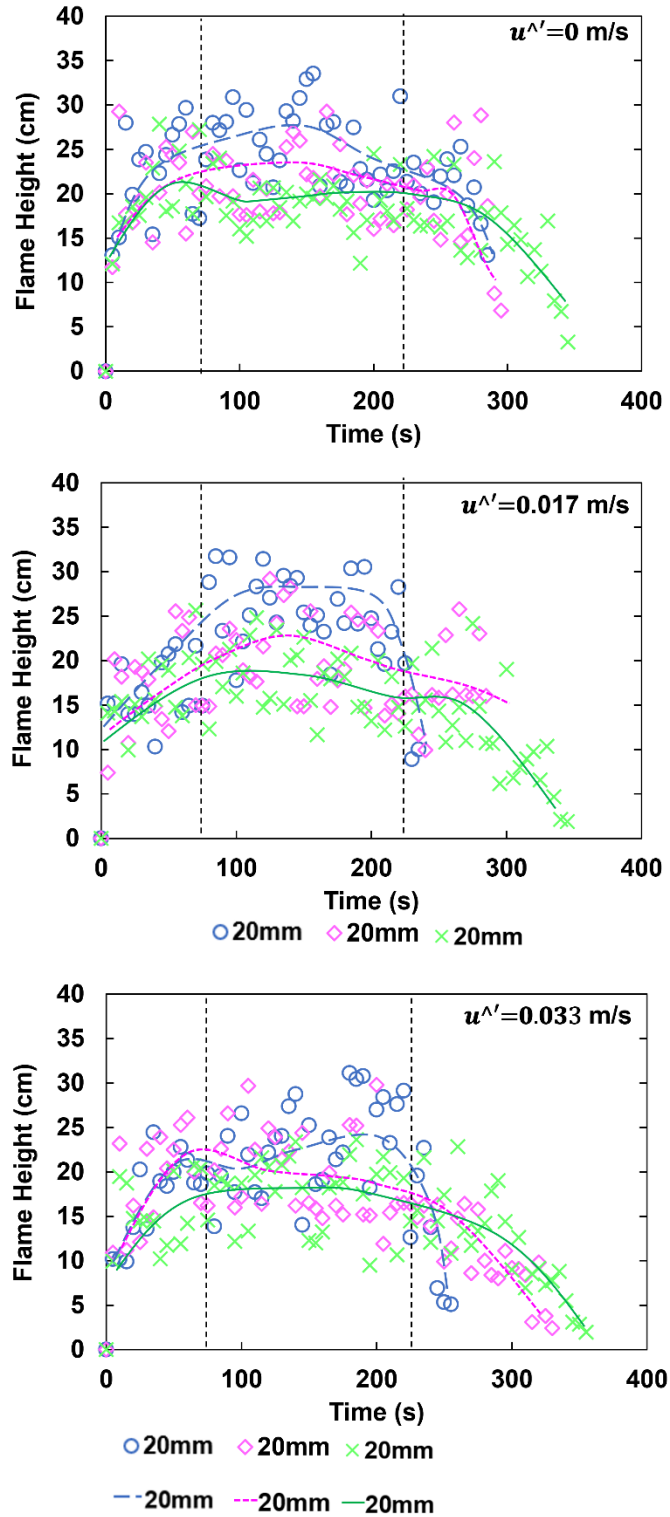
Figure 4. 19: Flame height for heptane layer burning experiments.

Figure 4.20 shows the photographs of the flame condition for all the heptane burning experiments at 150 seconds after ignition. This time stamp is selected as it is approximately midway of the

steady burning stage. The flame shapes are good examples to demonstrate the effects of different rods and turbulence on the heptane layer burning. In the no rod condition of $d = 0$ mm, the flame height has the peak value of 28 cm in stationary water sublayer ($u' = 0$ m/s). The flame shape appears to be sinuous at the flame sheet boundary with slight flame shedding. While the turbulence cases have a more unstable flame shape, such that the flame is wider in width and the flame shedding at the boundary is more apparent (Fig. 4.20a). The flame heights for $u' = 0.017$ m/s and 0.034 m/s decrease to 23 cm and 22 cm respectively.

Figure 4.20b and 4.20c illustrate the flame shapes for heptane layer burning with copper rod sizes of 10 mm and 20 mm. In general, the flame heights in rod cases are higher than the no rod cases. Under no turbulence condition, the nucleate boiling of the heptane layer is observed on the rod's immersed surface as shown in Figure 4.19. Heptane vapor bubbles are formed on the rod's surface and are released to the gas phase upon bursting, causing an enhancement of the burning rate. This explains higher flame heights of 31 cm and 32 cm for $d = 10$ mm and 20 mm under no turbulence conditions. Also, the flame shape is more curved with flame shedding at the boundary, because a larger flame sheet area is needed to consume the larger amount of heptane vapor. In turbulence cases, the flame is not as concentrated towards the rod compared with no turbulence conditions. The nucleate boiling in the heptane layer disappears for all the turbulence conditions. It follows a decrease in flame height to around 25 cm compared to more than 30 cm for $u' = 0$ m/s condition.
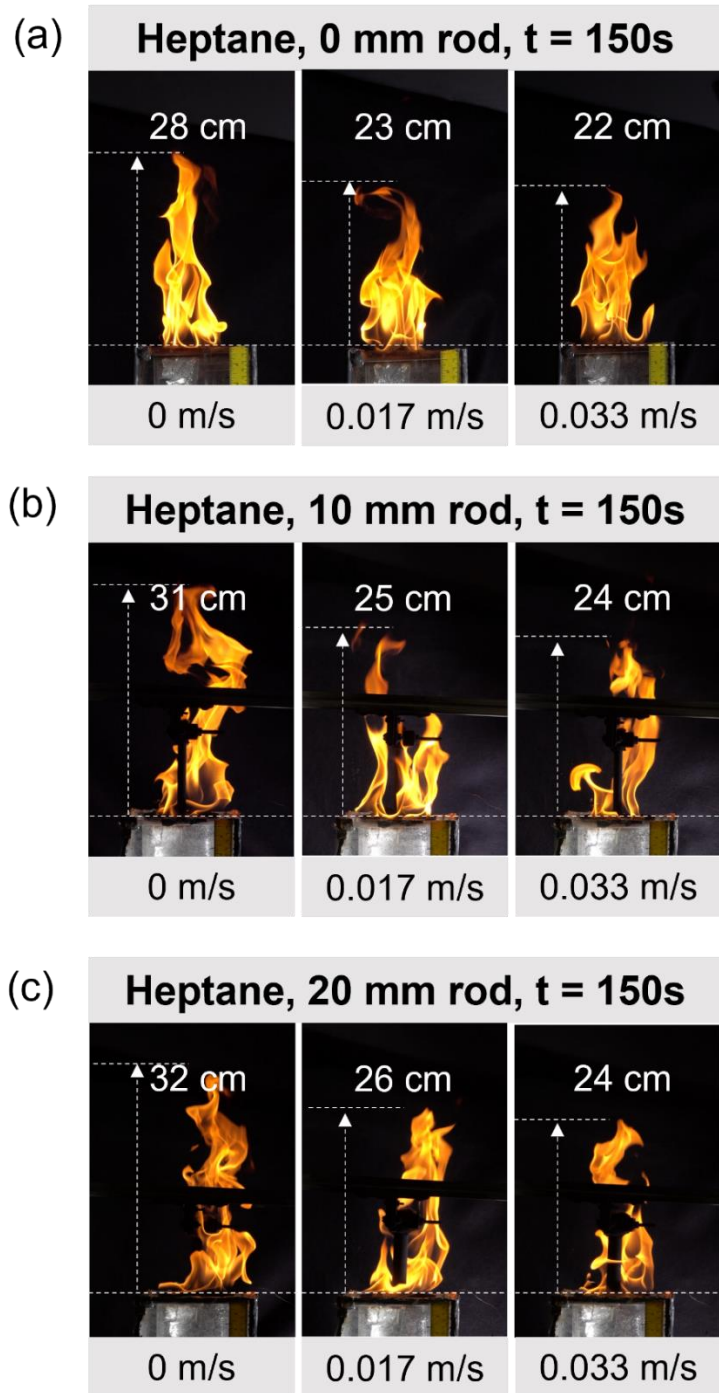
Figure 4. 20: Photographs of heptane burning flame heights in turbulence intensity of 0, 0.017, 0.033 m/s. (a) No copper rods. (b) 10 mm diameter copper rods. (c) 20 mm diameter copper rod. All the photos are taken 150 seconds after ignition.

Figure 4.21 shows the nucleate boiling of the heptane layer under no turbulence conditions with

10 mm and 20 mm rod cases. Nucleation sites are observed in the heptane layer with heptane

bubbles rapidly rising in columns, while in the water sublayer, bubbles attach to the rod's surface. These bubbles on the rod's surface in the water are dissolved air in the water similar to that observed just before water is about to boil in a hot pan for example. The bubbles grow very slowly in size, and some merge into larger bubbles. It takes up to 2 minutes for the bubbles to depart, which is very slow compared to the heptane bubble departure frequency of about 800 Hz on the 10 mm rod surface. Because of the high bubble departure frequency of heptane bubbles the heptane layer takes away nearly all the energy from the rod's collector section. It is under the effects of this nucleate boiling behavior, that the regression rate is enhanced with a copper rod.
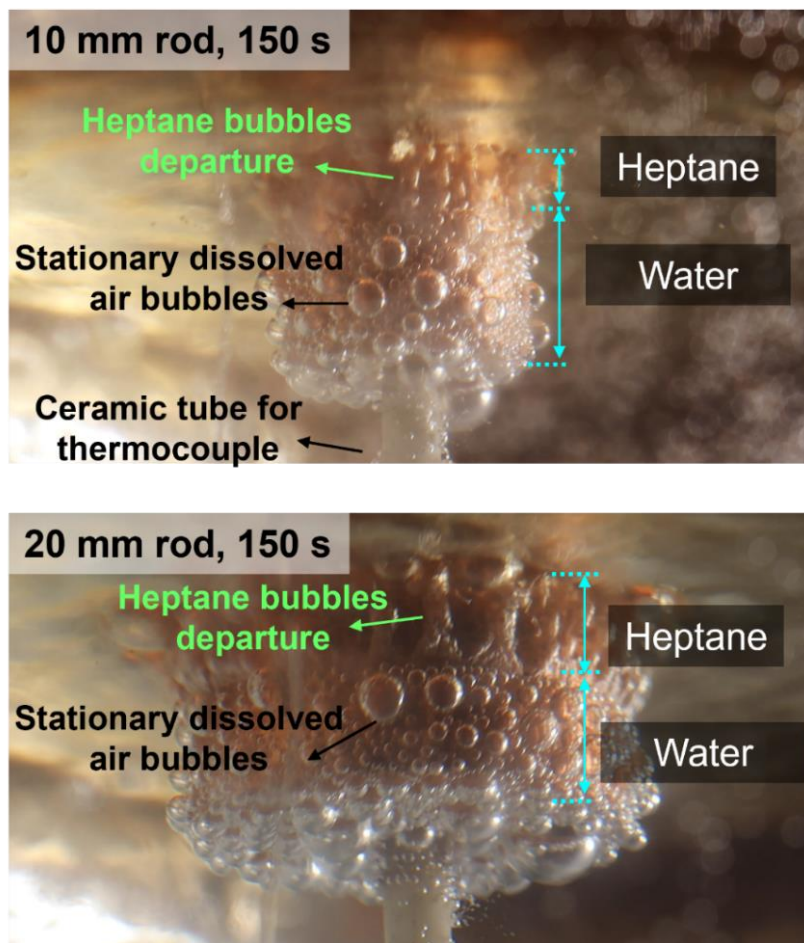
Figure 4. 21: Photograph of nucleate boiling at 150 s on 10 mm and 20 mm copper rod. The departure of heptane bubbles climbing upwards along the rod's surface. The dissolved air bubbles remain stationary in water layer.

4.5.3 Temperature profiles in the gas phase, fuel layer, water sublayer and rod for heptane burning

Section 4.4.3 discussed the temperature profiles of dodecane burning with the copper rod. The most distinctive difference between the temperature profiles of heptane and dodecane cases appears in the $u' = 0$ m/s no turbulence condition. Since the nucleate boiling behaviors are different, the heat transfer on the rod's surface for heptane burning mostly takes place in the fuel layer. While the heat transfer is more dominant in the water sublayer for dodecane layer burning. The result is that for the dodecane layer burning without turbulence, the water sublayer temperature will reach boiling point and eventually become superheated. Superheating of water to form water vapor bubbles does not occur in the case with heptane. Figure 4.22a shows that the temperature in the water sublayer never reaches the boiling point of water.

Compared with no turbulence case, when the turbulence intensity is set at the lower value of $u' = 0.017$ m/s, the burning time is significantly increased from 245 seconds to 329 seconds. The extended burning duration exhibits the negative impact of the turbulence cooling effects at the water sublayer and rod's bottom surface. Firstly, the temperature in the water sublayer is maintained at ambient temperature even with low turbulence of $u' = 0.017$ m/s as shown in Figure 4.22b. For the stronger turbulence at $u' = 0.033$ m/s, the burning time is the longest among the three conditions at 340 seconds. The extended burning time represents a slower regression rate because of the enhanced cooling effects on the fuel layer. At 150 seconds, the fuel/water interface temperature is measured at 75 °C for $u' = 0$ m/s, where for turbulence cases, the interface temperature drops to 65 °C and 61 °C for $u' = 0.017$ and 0.033 m/s respectively. The most significant fuel/water interface temperature decrease occurs from the no turbulence condition to the low turbulence condition, which corresponds to the distinctive extension in burning time. While as the turbulence intensity is turned up to $u' = 0.033$ m/s, the decrease of fuel/water interface temperature and extension of burning time do not change much. As one can expect, the significance is whether the water sublayer is made turbulent for the given experimental conditions. Since the heat loss from the interface to the water bath is very limited for stationary burning conditions, the enhancement of the turbulent cooling becomes obvious.
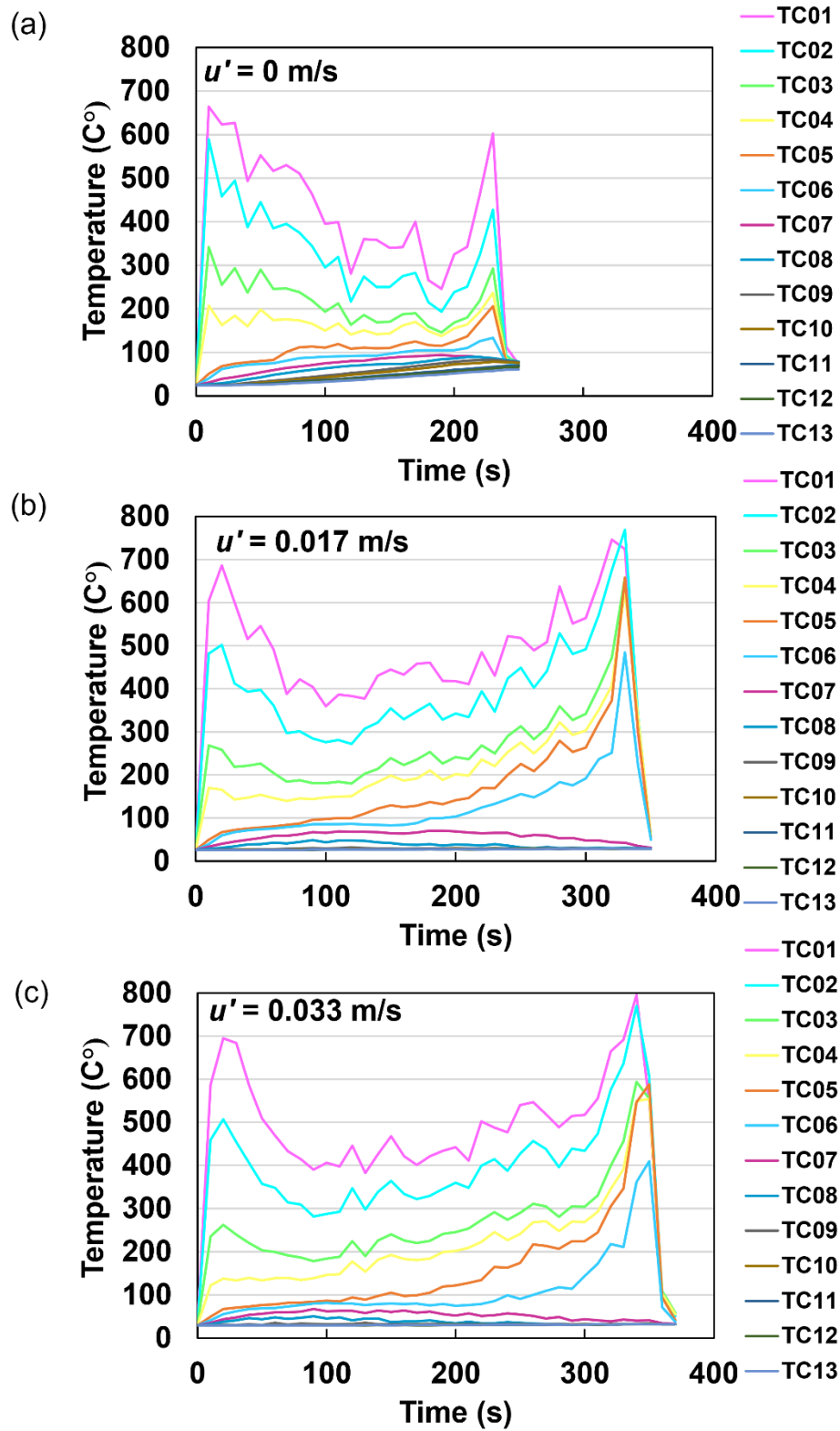
Figure 4. 22: Temperature profiles of heptane layer burning with 20 mm rod. (a) $u' = 0$ **m/s, (b)** $u' = 0.017$ **m/s, (c)** $u' = 0.033$ **m/s.**

Temperature profiles shown in Figure 4.22 provide two ways to directly measure the fuel layer regression rate. The first method is by dividing the burning duration of the initial fuel thickness for the global average regression rate. The second method is based on the thermocouple measurement data when the tip of the thermocouple comes out of the fuel surface as the surface regresses. The two methods have been explained in detail for dodecane cases in Section 4.4.3. Both methods are applicable for heptane as well.

For global average regression rates from Figure 4.22, the values can be calculated as 1.29, 1.00, and 0.82 mm/min given the initial heptane layer thickness of 5 mm. The regional regression rate at calculated using the time interval between the fuel surface descending from one thermocouple to the next. TC05 is a good reference thermocouple, because the temperature profile curves indicate the time when TC05 is moving into the gas phase as the values start to increase rapidly. By knowing the spacing between TC05 and TC06, and the time for the surface descending from TC05 to TC06, the regression rates can be calculated. For example, in the turbulent case shown in Figure 4.22b, the surface regression rate between the two thermocouples is: $1.2 \times 60/(160 - 90) = 1.03$ mm/min for 20 mm rod burning at $u' = 0.017$ m/s. For another turbulent case shown in Figure 4.22c, the regional regression rate is $1.2 \times 60/(190 - 110) = 0.90$ mm/min. calculated regional regression rates are slightly higher than the global average values because the regional regression rates are measured in the steady burning stage. The global average results include the pre-heating stage and decaying stage where the regression rates are comparably lower.
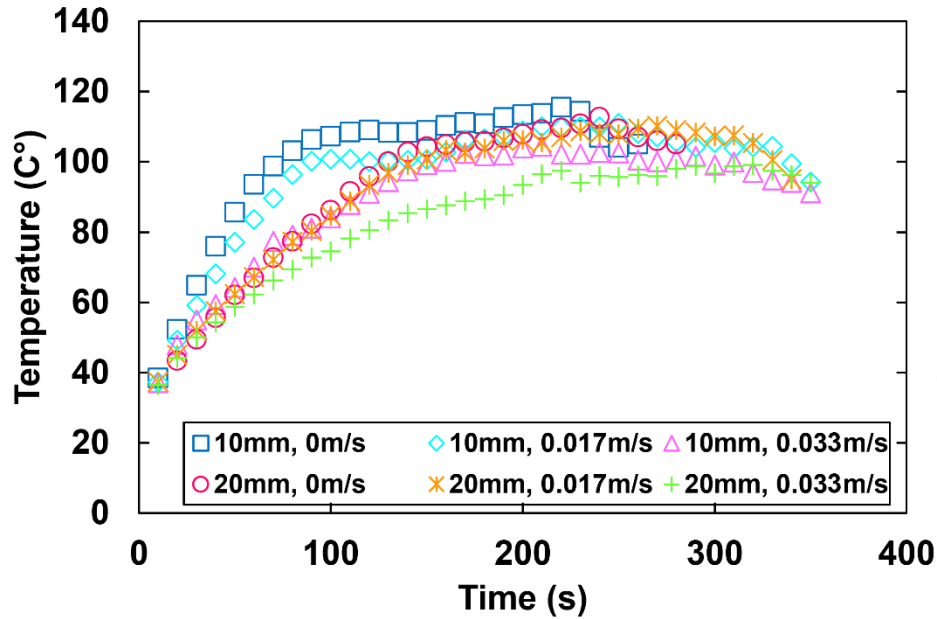
Figure 4. 23: Temperature profiles of rod center in the heptane layer (thermocouple D).

Figure 4.23 shows the temperature measurements of the thermocouple inserted into the rod body at location D in Figure 4.3a. As mentioned in the dodecane section, these temperature data represent the rod body temperature immersed in the heptane layer. Compared with the measurement results in Figure 4.11, some similarities are shared in heptane cases. Firstly, the thinner rod is more sensitive to the turbulence conditions such that the three curves of 10 mm rod cases are more separately placed especially in the pre-heating stage, while the temperature profiles of 20 mm rod cases cluster closely in the pre-heating stage. The pre-heating time for 10 mm rod is much shorter than the 20 mm rod heptane cases as well. For 10 mm rod cases, the no turbulence burning condition has a pre-heating time of 80, 90, and 160 s for $u' = 0$, 0.017, 0.033 m/s respectively. This time becomes much longer for 20 mm rod cases that the temperature curves do not flat out, and instead, the temperature constantly increases then drops as the burning rate decays to extinction. Therefore, the pre-heating stage for 20 mm rod cases can be presented by the time from the start until reaching the peak temperature. In that sense, the times are 240, 270, and 320 s for the three turbulence conditions respectively. Similar to the dodecane cases, the 20 mm rod will not have a flat stage of the temperature profiles given the initial fuel thickness of 5 mm. The peak temperature of 10 mm rod cases has values of 116, 111, and 106 °C for the three turbulence

109

intensities, and the temperature of 20 mm rod peaks at 113, 110, and 100 °C. The thicker rod appears to have a lower peak temperature during the burning process, given the fact that it is more capable of retaining heat under the effect of turbulent cooling. The reason would be that the burning times of heptane cases are so short that the thick rod has not reached a higher temperature yet and the burning already reaches the decaying stage with a very thin fuel layer left.

4.5.4 Burning Rate Formulation

In this section, the burning rate formulations of the heptane layer burning in no rod cases using the surface energy balance (Eqn. 4.1) and rod cases using the control volume energy balance (Eqn. 4.4) are discussed.

4.5.4.1 Case 1: Heptane Burning with no Rods Conditions

The burning rate can be modeled by a fuel surface energy balance given by Equation 4.1. Under this burning condition, the heat input onto the fuel surface is determined by the gas phase conduction, and the heat diffusion in the liquid layers is by means of conduction. This procedure is similar to the dodecane layer burning in Section 4.4.4.1 and will not be elaborated further.

Figure 4.24 shows the regression rate results of experiments (global and regional). Note that the thermocouple measurements used in the model are from the burning time between 130 – 170 seconds in the steady regression stage. The model results match with the experimental results reasonably well. The model also predicts the changing trend as the turbulence increases.
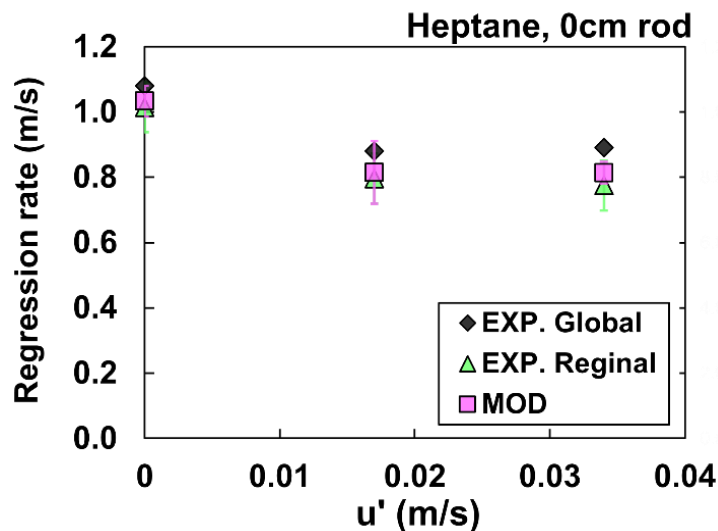
Figure 4. 24: Heptane burning regression rate results from the surface energy balance model and experimental results for global average and regional average.

4.5.4.2 Case 2: Heptane Burning with Rods and no Turbulence Conditions

Different from the suppression effects discussed in the dodecane cases, the burning rate is enhanced for the heptane layer burning with a copper rod in still water. This is caused by the nucleate boiling within the heptane layer as explained previously. This section focuses on the burning rate facilitation effects of the rod cases in the stationary water sublayer. The control volume energy balance based on Equation 4.4 is modified such that the bottom boundary includes the fuel/water interface and the rod's bottom surface immersed in the water layer (same as shown in Figure 4.16). Additionally, the extra heptane evaporation caused by the nucleate boiling on the rod's surface will be considered. The mass transfer as the form of water vapor bubbling at the fuel/water interface does not occur. As a result, the energy balance equation becomes:

$$\dot{m}_{F,surf} L_F = \dot{q}_s + \dot{q}_{e,rod} - \dot{q}_{loss,int} - \dot{q}_{loss,rod} - \dot{m}_{F,rod} L_F \ , \qquad (4.12)$$

where the heat input from the gas phase, $\dot{q}_s$ and from the rod's cross-section in the control volume is the same as the former dodecane cases of $\dot{q}_s = A_F k_{air} (dT/dy)_{y=0+}$ (Eqn. 4.5) and $\dot{q}_{e,rod} = A_{rod} k_{copper} (dT/dy)_{A \rightarrow B}$. The heat loss at the fuel/water interface, $\dot{q}_{loss,int}$ is by conduction in the water sublayer: $\dot{q}_{loss,int} = A_F k_W (dT/dy)_{F/W-}$. The above energy terms can be measured by the thermocouple array and the thermocouples on the rod's surface.

Furthermore, the heat loss on the rod's bottom section contacting the water layer can be estimated according to the dissolved air bubble condition at this rod area. As shown in Figure 4.21, the dissolved air bubbles only appear to be attached to the rod's surface and the departure rate can be neglected. This indicates the heat flux at this rod region is enough for bubble generation but not sufficient to pass the threshold of onset of nucleate boiling. Therefore, the boiling curve for water at 1 atm reported by Incropera et al. [107] can be used to estimate the heat flux value at the rod's bottom. When the surface heat flux approaches 10,000 W/m², the boiling curve starts to reach the boiling region from the pure convection region. Based on this, the heat loss term on the rod's bottom section, $\dot{q}_{loss,rod}$ can be expressed as $\dot{q}_{loss,rod} = A_{r,W} \dot{q}''_{ONB}$ and $\dot{q}''_{ONB} = 10,000$ W/m². The two energy terms for fuel evaporation terms are: (1) the fuel evaporation on the rod's surface

within the heptane layer by nucleation boiling, $\dot{m}_{F,rod}L_F$ and (2) the fuel evaporation on the burning heptane surface, $\dot{m}_{F,surf}L_F$.

The energy transferred by heptane bubble generation $\dot{m}_{F,rod}$ is analyzed by bubble counting using highspeed videography. The procedure is identical to the mass measurements of water bubbles on the rod's surface in dodecane cases (Section 4.4.4.2). Further, only one highspeed camera is needed to capture the heptane bubble departure on the rod's surface. The camera is set at 2873 FPS with a recording resolution of 800×600 viewing at the rod's immersed surface. The heptane bubbles quickly climb up along the rod's surface and burst at the fuel surface. To measure the departure frequency, 600 continuous frames are used. The number of heptane bubbles reaching the fuel surface are counted by image processing the 600 frames. Then the result is doubled to account for the entire rod perimeter. Next, a factor of 4.76 is multiplied to yield the bubble departure number for 1 second given that the 600 frames correspond to 0.21 seconds. This bubble measurement is performed at 150 s after ignition, which is following the thermocouple measurements in this steady burning region. Figure 4.25 shows an example of the highspeed camera snapshots of heptane bubble tracking. The bubble departure size is 1 mm and the number with dash circles tracks the bubble position.
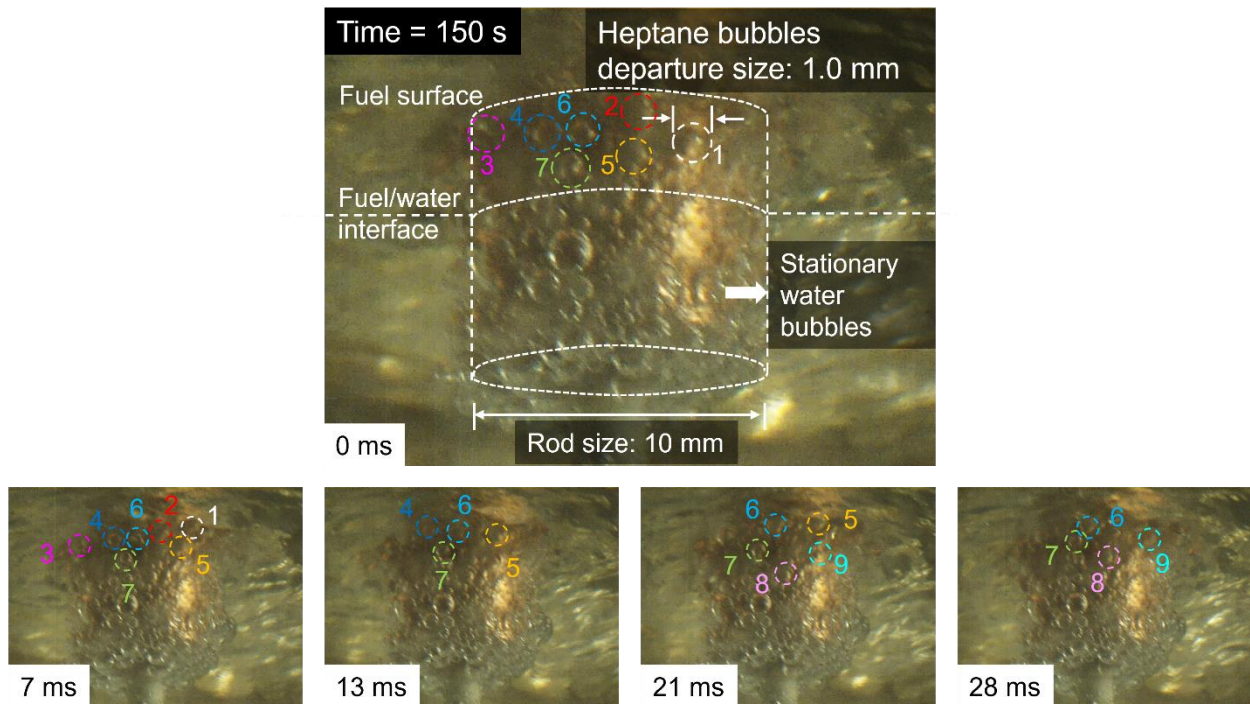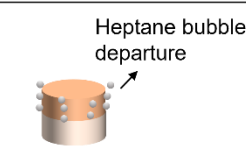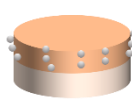
Figure 4. 25: Bubble measurement of heptane nucleation boiling on the 10 mm copper rod. The photo strip shows the bubble movement tracking in a 7 ms interval at 150 s.

Table 4.5 shows the bubble measurement results of 10 mm and 20 mm copper rod burning cases with no turbulence conditions. The schematics show heptane bubble nucleation areas. Note that only the rod's surface is shown in the drawing because the entire pool area is not needed in this case as no boiling occurs at the heptane/water interface. As the copper rod collects heat in the gas phase, the temperature gradient between the collector section and the immersed section will be formed, which causes the heat transfer into the rod's bottom section. The rod's surface temperature will rise until the boiling point of heptane is reached at 98 °C. At this condition, heptane bubbles are generated in the fuel layer, and the onset of nucleate boiling is shown in Table 4.5. For a 10 mm rod, the time to reach heptane boiling is 45 seconds and 85 seconds for a 20 mm rod. It takes longer for the thicker rod to accumulate energy because of the much larger heat capacity. The departure size of the heptane bubbles is measured to be identical at 1 mm for both rod sizes. For departure frequency, the heptane cases are much higher than the dodecane cases. Compared with the latent heat of gasification of dodecane at 358 J/g, heptane is lower at 318 J/g. Besides, the boiling point of dodecane is much higher at 216 °C than that of heptane (98 °C). Therefore, the latent energy for evaporation as calculated by $L_F = \Delta H_F + c_{p,l}(T_b - T_\infty)$ for heptane is much lower in value. This is demonstrated experimentally by a higher bubble departure frequency in heptane cases because the bubble generation is easier. For 10 mm rod, the departure frequency is 800 Hz and the value doubles to 1600 Hz for 20 mm rod. The thicker rod is heated at a lower speed, which causes the bubble generation at each nucleation site to be slower. However, because of the larger sidewall area in the heptane layer, the thicker rod still has a higher bubble departure rate.

Table 4. 6: Bubble measurement results for heptane layer burning with copper rods under no turbulence condition.

Schematic of heptane layer burning	Rod Diameter (mm)	Time to onset (seconds)	Departure size (mm)	Departure frequency (Hz)
Heptane bubble departure	10	45	1.0	800
	20	85	1.0	1600

Based on Equation 4.12, all terms can be estimated and the heptane consumption rate on the fuel surface, $\dot{m}_{F,surf}$ can be calculated. Now, the corresponding modeled results of $\dot{m}_F'' = \frac{\dot{m}_{F,surf} + \dot{m}_{F,rod}}{A_F}$ for each burning configuration can be obtained then it can be compared with the experimental results.

Table 4. 7: Modeling and experimental results of heptane mass flux on the pool surface.

Heptane layer burning configuration	Model results of $\dot{m}_F''$ (g/m²s)	Experimental results of $\dot{m}_F''$ (g/m²s)
10 mm rod, $u' = 0$ m/s	14.15	14.35
20 mm rod, $u' = 0$ m/s	15.43	15.16

Table 4. 7 shows the modeled and experimental results of the heptane mass flux on the pool surface. By comparison with the two sets of results, the modeled heptane mass flux values have good agreement with the experimental data. Also, the modeled mass burning rate increases with a larger rod diameter, which matches the experiments as well. Kang et al. [114] reported the burning rate of small-scale heptane pool fires. Their experimental measurement of mass loss flux at the fuel surface was around 10 g/m²s for a 10 cm pool fire, where the lower experimental result is supposed to be caused by their temperature condition at 13.4 °C compared to 28 °C in this study.

4.5.4.3 Case 3: Heptane Burning with Rods and Turbulence Conditions

When the water sublayer is made turbulent, the nucleate boiling on the rod's surface in the heptane layer disappears because the film of liquid heptane touching the rod's surface cannot be kept at super-heated condition within a dynamic fuel layer. Therefore, the control volume energy balance needs to be modified to describe the turbulent conditions. The equation is similar to that used for dodecane and given by: $\dot{m}_F L_F = \dot{q}_s + \dot{q}_{e,rod} - \dot{q}_{loss,int} - \dot{q}_{loss,rod}$ (Eqn. 4.7). Each energy term is discussed in detail in Section 4.4.4.3.

Table 4.8 shows the details of energy terms in the burning rate formulation. The calculated burning rates have a good match with the experimental burning rates. For the same rod size, the burning rate decreases with stronger turbulence intensity. When the 10 mm rod is used, the calculated mass burning rates are 0.103 and 0.076 g/s as u' increases from 0.017 m/s to 0.033 m/s. The same trend

is also found in the 20 mm rod cases, where the calculated burning rate is 0.108 g/s for $u' = 0.017$ m/s and 0.076 m/s for $u' = 0.033$ m/s. Moreover, under the same turbulence intensity, the difference between 10 mm and 20 mm rods is very minor. This means the water sublayer turbulence is a more influential factor compared with the rod's size in heptane burning.

From Table 4.8, we can exam each energy term to have comprehensive understandings of the effects of water sublayer turbulence and rod diameter. In terms of the energy input from the gas phase to the pool surface, $\dot{q}_s = A_p k_{air} \left(\frac{dT}{dy}\right)_{y=0+}$ increases as the turbulence increases, because the pool surface is exposed to a lower flaming zone. As in the dodecane cases, the thermocouples in the gas phase close to the fuel surface capture this flame location shifting. $\dot{q}_s$ for heptane is lower compared to dodecane cases because the flame height in dodecane cases is much lower.

Table 4. 8: Calculations of energy terms in the burning rate formulation of heptane burning with a copper rod in turbulence conditions.

$A_F k_{air} \left(\frac{dT}{dx}\right)_{y=0+} + A_R k_c \frac{T_{R,A} - T_{R,B}}{S_{12}} - A_F h_{int}(T_{int} - T_\infty) - A_{r,W} \dot{q}''_{bottom,rod} = \dot{m}_F L_F$					
Conditions	$A_F k_{air} \left(\frac{dT}{dx}\right)_{y=0+}$	$A_R k_c \frac{T_{R,A} - T_{R,B}}{S_{AB}}$	$A_F h_{int}(T_{int} - T_\infty)$	$A_{r,W} h_{rod}(T_{R,C} - T_\infty)$	$\dot{m}_F$
$d = 0.01$ m $u' = 0.017$ m/s	$0.007775*0.0469$ $*65721$ $=24.97$ W	$\left(401\frac{35.5}{0.02}\right)\pi(0.005)^2$ $=55.90$ W	0.007775 $*92(55.5 - 26.9)$ $=20.46$ W	$0.000393 * 963 * (76.8$ $- 26.9)$ $=18.87$ W	$\frac{24 + 55.9 - 20.5 - 18.9}{317.7 + 2.3 * (98 - 65.7)}$ $=0.103$ g/s EXP average: 0.086 g/s
$d = 0.01$ m $u' = 0.033$ m/s	$0.007775*0.0469$ $*71626$ $=26.12$ W	$\left(401\frac{32.8}{0.02}\right)\pi(0.005)^2$ $=51.65$ W	0.007775 $*126(52.8 - 28.4)$ $=23.9$ W	$0.000393 * 1362$ $* (71.7 - 28.4)$ $=23.16$ W	$\frac{26.1 + 48.5 - 23.9 - 16.4}{317.7 + 2.3 * (98 - 61)}$ $=0.076$ g/s EXP average: 0.083 g/s
$d = 0.02$ m $u' = 0.017$ m/s	$0.00754*0.0469$ $*63958$ $=22.6$ W	$\left(401\frac{11.1}{0.02}\right)\pi(0.001)^2$ $=69.92$ W	0.00754 $*92(53.6 - 27.4)$ $=18.17$ W	$0.000942 * 681 * (75.6$ $- 27.4)$ $=31.55$ W	$\frac{22.6 + 76.9 - 18.2 - 44.6}{317.7 + 2.3 * (98 - 64.3)}$ $=0.108$ g/s EXP average: 0.085 g/s
$d = 0.02$ m $u' = 0.033$ m/s	$0.00754*0.0469$ $*68405$ $=24.2$ W	$\left(401\frac{9.8}{0.02}\right)\pi(0.001)^2$ $=61.73$ W	0.00754 $*126(51.3 - 30.1)$ $=20.1$ W	$0.000942 * 966 * (68.6$ $- 30.1)$ $=35.09$ W	$\frac{24 + 65.5 - 20.5 - 30.1}{317.7 + 2.3 * (98 - 65.7)}$ $=0.076$ g/s EXP average: 0.083 g/s

The energy inputs through the copper rod's cross-section area $\dot{q}_{e,rod} = A_{rod} k_{copper} \left(\frac{T_{R,A} - T_{R,B}}{S_{AB}}\right)$ are smaller in 10 mm rod (55.90 and 51.65 W) than 20 mm rod (69.92 and

61.73 W). Even the temperature difference of $T_{R,A} - T_{R,B}$ is more significant on the 10 mm rod, which is above 30 °C for both turbulence intensities. The small cross-section area of the thinner rod brings down the $\dot{q}_{e,rod}$ value even with the $T_{R,A} - T_{R,B}$ values being only around 10 °C. Comparing the two energy input terms, we can notice that the rod helps to transfer a larger amount of energy into the liquid layers than the energy transfer from the gas to the fuel surface. However, the turbulent water sublayer at the rod's bottom section takes away a noticeable amount of heat as well. Another heat loss is through the fuel/water interface by convection. This term is expressed by $\dot{q}_{loss,int} = A_{pool}h_{int}(T_{int} - T_\infty)$ and the values are larger with 10 mm rod, which is caused by the lower interface temperatures measured in 10 mm rod. It appears that the convective heat loss on the 20 mm rod's bottom section is quite strong so that there is not enough energy going into the heptane layer to rise the interface temperature. As the result, the $\dot{q}_{loss,int}$ of 10 mm cases are 20.46 and 23.9 W with respect of the two turbulence conditions while in 20 mm rod cases, the $\dot{q}_{loss,int}$ are lower at 18.17 and 20.1 W.

Figure 4.26 shows the summary of energy terms for dodecane and heptane layer burning with rod and turbulent water sublayer from Equation (4.7) that are listed in Table 4.5 and Table 4.8. Each bar represents the energy value in the unit of W corresponding to the heat input term or heat loss term under each specific burning configuration. For both types of fuel, the energy inputs through the copper rod appear to be the dominate heat source going into the liquid layers compared to the heat input through the fuel surface. The heat inputs through the fuel surface, $\dot{q}_s$ remain almost constant for all the case. The thicker rods have both higher energy inputs $\dot{q}_{e,rod}$ and more heat loss to the water sublayer $\dot{q}_{loss,rod}$. Under the turbulence range ($u' = 0.017$ and 0.033 m/s) in this chapter, the rod diameter ($d_r = 10$ and 20 mm) is more influential compared to the turbulence intensity in terms of altering the heat transfer behaviors of the copper rod. However, as more heat is transferred to the fuel layer with a thicker rod, more heat loss is lost to the water sublayer at the same time. Therefore, the mass burning rate is not so sensitive to the rod size because the two effects tend to cancel out. By comparison, the water sublayer turbulence intensity has more influence on the mass burning rate. This is because the additional heat loss at the fuel/water interface further reduces the amount of heat being used for fuel evaporation at the pool surface. Among all the experimental parameters, the most influential factor is the fuel type since heptane burns much more quickly than dodecane under every burning condition. From Figure 4.26, the

heat loss through the fuel/water interface $\dot{q}_{loss,int}$ is much higher in dodecane cases because the temperature difference of the interface and water sublayer is measured much larger.
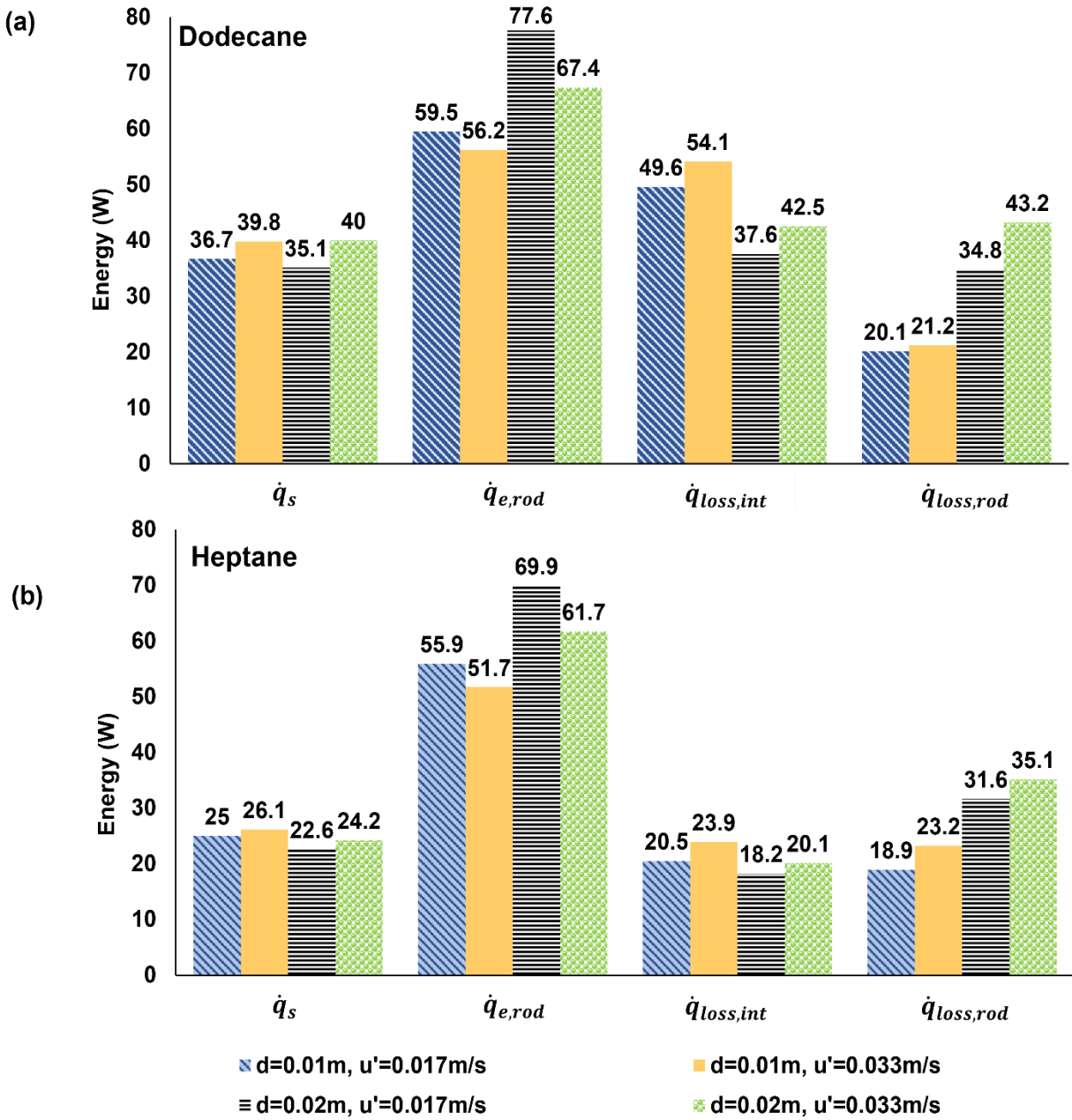
Figure 4. 26: Summary of energy terms. (a) Dodecane layer burning with a copper rod and turbulent water sublayer. (b) Heptane layer burning with a copper rod and turbulent water sublayer.

4.6 Effect of multiple rods placement in turbulent condition

The previous sections have demonstrated the experimental and modeled results of fuel layer burning in various configurations, among which the data of the burning cases with rod placement and turbulent water sublayer are considered most meaningful to help us investigate the effectiveness of the Flame Refluxer in real world applications. Although there is only a single rod used in this study and the convective heat loss is high, the thicker rod (20 mm) still has a positive effect on the burning rate of both dodecane (Fig. 4.6) and heptane layer (Fig. 4.18). This leads to the following theoretical discussions of using multiple rods to increase the fuel layer burning rate.

Figure 4.26 shows that the amount of energy lost to the water layer on the rod's bottom area $\dot{q}_{loss,rod}$ appears to be quite large given the fact that a short section of 1 cm of the rod is immersed in the water layer. In turbulence condition, the bottom of the rod acts as a heat sink, which constantly drains the energy collected from the flame. To achieve the best, the bottom of the copper rods should be placed within the fuel layer. The contact between the rods and water sublayer should be avoided therefore all the collected energy can be dissipated into the fuel slick. Under this situation, the governing energy equation considering the fuel layer as the control volume can be modified based on Equation 4.3 without the energy loss term on the rod $\dot{q}_{loss.rod}$ to:

$$\dot{m}_{F,surf}L_F = \dot{q}_s + \dot{q}_{e,rod} - \dot{q}_{loss.int} \quad , \tag{4.12}$$

The energy terms used for bubble generation are neglected because the nucleate boiling of any liquids is hardly observed under turbulent conditions. Let's assume N rods with the diameter of 10 mm are used. The thermal interaction between rods is neglected in this analysis. The energy input in the gas phase on the fuel surface can be expressed by:

$$\dot{q}_s = \left(A_{pool} - NA_{rod}\right)k_{air}\left(\frac{dT}{dy}\right)_{y=0+} \quad , \tag{4.13}$$

This value is almost constant for the same fuel type across different burning configurations as shown in Figure 4.26. For dodecane burning $\dot{q}_s$ is assumed to be 38 W and 25 W for heptane burning. Next, the energy input through the copper rods into the fuel layer is:

$$\dot{q}_{e,rod} = NA_{rod}k_{copper}(dT/dy)_{A\to B} \quad , \tag{4.14}$$

where the temperature gradient of the rod at the fuel surface $(dT/dy)_{A \to B}$ can be estimated using the measured thermocouple data. For dodecane layer burning case, $T_{R,A} - T_{R,B}$ equals 37 °C for 10 mm copper rod (Table 4.5). For Heptane burning, $T_{R,A} - T_{R,B}$ equals 34 °C for 10 mm copper rod (Table 4.8). These vertical temperature difference on the rod is assumed to be constant across the use of N rods, and the distance between A and B is fixed at 2 cm. From the experimental results, the temperature difference Furthermore, the convective loss at the fuel/water interface becomes:

$$\dot{q}_{loss.int} = A_{pool} h_{int} (T_{int} - T_\infty) \quad , \tag{4.15}$$

The surface of the pool is used because the rod's bottom does not reach into the water layer. To investigate the rods effect under the worst scenario, the fuel/water interface temperature T_{int} is assumed to be the boiling point of the fuel which yields a maximum value of $\dot{q}_{loss.int}$. Therefore, T_{int} equals 216 °C and 98 °C for dodecane and heptane layer burning respectively. The convective heat transfer coefficient in the water layer h_{int} increases with u' and the values are adopted from Table 3.9.

To achieve enhancement on the fuel burning rate, the external heat supplied by the rods ($\dot{q}_{e,rod}$) need to compensate the convective heat loss at the water interface ($\dot{q}_{loss.int}$). Figure 4.27 shows the comparisons of the $\dot{q}_{e,rod}$ and $\dot{q}_{loss.int}$. The dashed horizontal lines represent the heat inputs from N number of rods. The curve lines represent the convective heat loss increase as turbulence intensity (u') increases. Each figure is divided into two areas: 1) the area above the heat loss curve stands for the condition where the N rods act positively to enhance the fuel burning rate and 2) the area below the curve represents the condition where the convective heat loss surpasses the heat input by the rods. In the enhancement region, the energy provided by the rods can overcome the heat loss to the water sublayer so that all the energy absorbed on the fuel surface can be used for fuel evaporation, thus achieving burning enhancement. It is noticed that the dodecane burning condition requires more rods for enhancement compared to the heptane burning under the same turbulence intensity, which matches with the fact that heptane is more flammable. A – F are chosen for sample calculations to demonstrate the effect of the multiple rod placement where each fuel type includes three data points. These points are selected in the fashion that one point is lower than the convective heat loss curve with $N = 1$ and the next point has a greater number of rods under

the same turbulence intensity. Then, the third point is at the same number of rods placement but in higher water layer turbulence (Fig. 4.27).

(a)

(b)
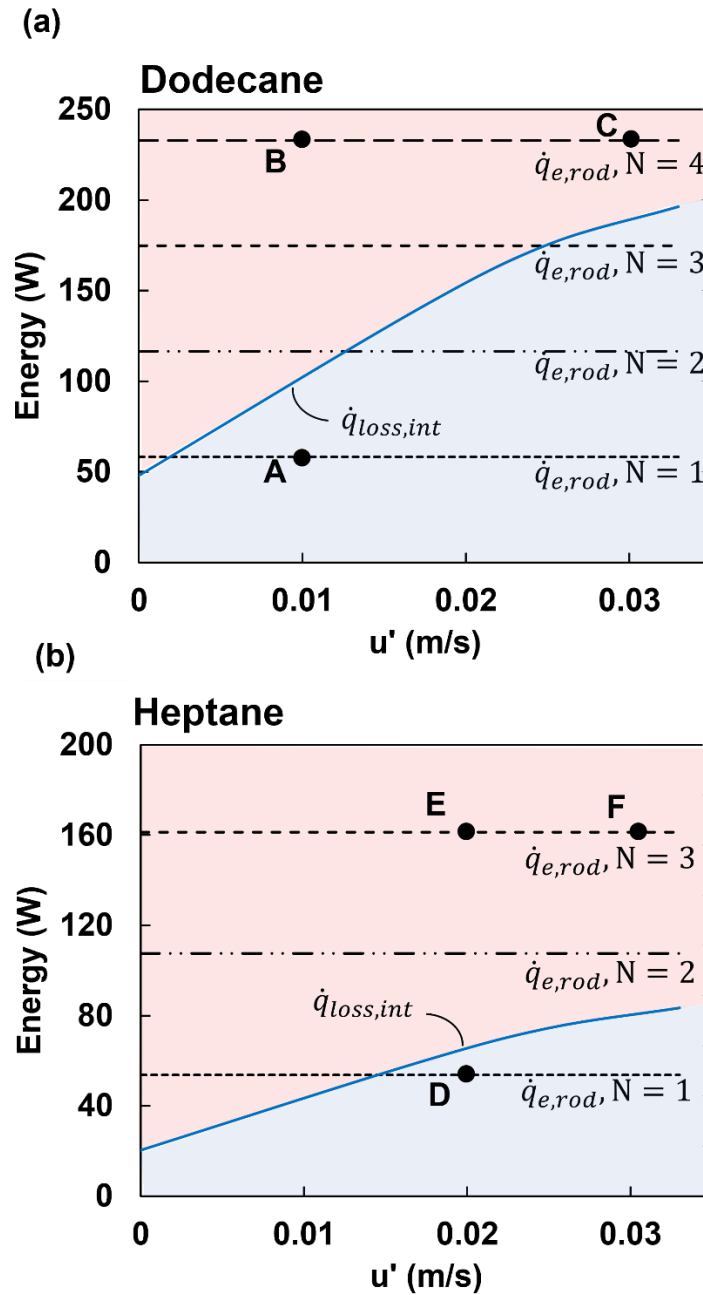
Figure 4. 27: Comparison between convective heat loss at the fuel/water interface and external energy input through the N rods. (a) Dodecane layer burning. (b) Heptane layer burning. A – F represent six sample calculation points.

Table 4.9 shows the details of mass burning calculation of the selected data point A – F. The pool area is 10 cm in diameter. The estimated mass loss results obtained by the multiple rods theory are

compared to the baseline mass loss measurements under no rod placement condition with a still water layer. According to the ratio of calculated results over experimental baseline, the application of additional copper rods can effectively increase the burning rate. When water layer turbulence intensity is $u' = 0.03$ m/s, the burning rate can increase to more than 300% the baseline when 4 copper rods with diameter of 10 mm are immersed in the fuel layer. The increase of burning rate is significant when 4 rods are used compared to 1 rod condition. For heptane burning cases, the burning rate increases to more than 400% the baseline when 3 rods immersed in the fuel slick. Since the heptane layer is more flammable than dodecane layer, it requires fewer rods to achieve a very high burning rate in heptane burning cases. The calculated increase ratios match with the results from Arsava et al. [28] where the crude oil pool fire burning speed is enhanced up to 500% in a 1 m pan.

Table 4. 9: Sample calculations of multiple rods effects on the burning rate.

Data Point	Num. Rods	u' (m/s)	L_f (J/g)	$\dot{q}_s$ (W)	$\dot{q}_{loss,int}$ (W)	$\dot{q}_{e,rod}$ (W)	$\dot{m}_{theory}$ (g/s)	$\dot{m}_{base,exp}$ (g/s)	% over baseline
				Dodecane					
A	1	0.01	596	38	94	61	0.0088	0.058	**15.1%**
B	4	0.01	596	38	94	244	0.33	0.058	**586%**
C	4	0.03	596	38	175	244	0.19	0.058	**323%**
				Heptane					
D	1	0.02	394	25	59	53	0.047	0.10	**46.6%**
E	3	0.02	394	25	59	212	0.45	0.10	**448%**
F	3	0.03	394	25	72	212	0.42	0.10	**415%**

The above theory provides an engineering design basis in terms of copper rods (Flame Refluxer) application on in-situ burning in a dynamic water environment. The calculations benefit from the experimental measurements to reasonably estimate the heat transfer through the rod and liquid interfaces.

4.7 Conclusions

Under no turbulence condition ($u' = 0$ m/s), the fuel layer burning rate is noticeably affected by the fuel type, or more specifically, the boiling point of the fuel compared to the water boiling point when a copper rod is placed in the fuel and water layers. For the two fuels used in this chapter, the dodecane layer (boiling point of 216 °C) burning condition has nucleate boiling on the rod's surface in the water sublayer. On the contrary, the nucleate boiling occurs on the rod's surface within the fuel layer in heptane layer (boiling point of 98 °C) burning condition. The different nucleate boiling region causes suppression and facilitation on the dodecane and heptane burning rate separately, where water bubbles are generated in dodecane burning and heptane bubbles are generated in heptane burning. The heat transfer by bubble generation is estimated by bubble counting using highspeed image processing. The burning rates under both burning conditions are modeled and the calculated results match with the experimental results.

Under turbulence conditions ($u' = 0.017$ and 0.033 m/s), the nucleate boiling is not observed for both types of fuel on the rod's surface. The suppression and facilitation effects by bubbles in no turbulence conditions are no longer in consideration. Despite that, heptane still has a much higher burning rate compared with dodecane. This is because the comparably higher fuel/water interface temperature for dodecane and the water sublayer temperature is constant at ambient temperature for all the cases. The rod diameter ($d_r = 10$ and 20 mm) is influential in terms of altering the heat transfer behaviors through the copper rod, but not so much to the burning rate. Instead, the water sublayer turbulence intensity has more influence on the fuel layer burning speed.

The theoretical analysis of multiple rods placement indicates a burning rate increase of 300% for dodecane layer burning with 4 immersed copper rods under water turbulence intensity of $u' = 0.03$ m/s. And the increase of 400% is achieved in heptane layer burning with 3 immersed copper rods under the same turbulence condition.

The theoretical analysis of multiple rods placement indicates a burning rate increase of 300% for dodecane layer burning with 4 immersed copper rods under water turbulence intensity of $u' = 0.03$ m/s. And the increase of 400% is achieved in heptane layer burning with 3 immersed copper rods under the same turbulence condition. The enhancement is made possible by avoiding the rod's bottom contacting the water sublayer.

Chapter 5: Conclusions

5.1 Outcome of the current work

A lab-scale turbulence generation system is built to create isotropic turbulence as the experimental foundation of this study. The water surface region is made turbulent using an upward confined jet and the turbulence intensity (root-mean-square velocity, u') can be adjusted precisely by controlling the flow rate through the jet nozzle. The turbulence is measured using Particle Image Velocimetry and the result shows the system can simulate the fluctuating turbulence as measured in a calm ocean surface. The u' operation range in this study is $0 - 0.050$ m/s for the wire experiment in Chapter 2 and $0 - 0.033$ m/s for the fuel layer burning experiments in Chapter 3 and Chapter 4.

In Chapter 2, the heat transfer mechanism and bubble behaviors of subcooled nucleate pool boiling using 0.127 mm diameter nichrome wire are experimentally studied in a 4 cm thick isotropic turbulent dodecane layer. The heat transfer is closely interrelated with bubble behaviors so that four stages of bubble behaviors characterize different corresponding regions of the nucleate boiling curve. They are, respectively: sweeping stage, bouncing and merging stage, hanging stage, and film boiling stage. The heat transfer shows improvement under turbulent cases. Bubble departure frequency (BDF) and critical heat flux (CHF) increase as a function of turbulence strength represented by root-mean-square (RMS) velocity. Bubble departure size decreases as a function of turbulence RMS velocity. The bubble propulsion mechanism is dominated by two competing factors: Marangoni force and thermocapillary convection. Both are subject to the impact of turbulent eddies, which facilitates the bubble lift-off, and improves the heat transfer performance compared with the baseline case. This chapter offers a basic understanding of the heat transfer of hot objects immersed in the turbulent liquids, which contributes to the analysis of Chapter 4 where the pool fire is coupled with the copper rod placement in the fuel and water layer.

In Chapter 3, the crude oil slick burning on a turbulent water bath is studied. An oil layer with an initial thickness of 5 mm has been used and the mass loss rate decreases when the water sublayer is made turbulent. A weaker burning process with smaller flame height and boilover behavior is

observed as the turbulence intensity becomes stronger. The thermocouple array measurements indicate that the water sublayer cannot develop temperature gradients even at the low level of turbulence intensity at $u' = 0.017$ m/s. The heat reaching the water will be instantly taken away because of the turbulent mixing thus facilitating the heat loss of the oil slick, which causes a reduction in MLR up to 34% at $u' = 0.033$ m/s compared to baseline. The convective heat transfer coefficient in the water sublayer is obtained by matching the one-dimensional conduction model to the measurement data and has the value of $h_{conv} = 78, 93, 125$ W/m^2 corresponding to $u' = 0.017, 0.025, 0.033$ m/s. The value of χ indicates the fraction of the total combustion heat release rate being absorbed onto the fuel surface, and it decreases with the turbulence intensity which is a result of weakened flame causing heat flux changes in the mass burning rate model. The heat and mass transfer characteristics during the oil slick burning are highly related and both are subject to the impact of the presence of turbulence in the water sublayer. The results in this study reveal the challenge of in-situ burning in the ocean environment and lead to the fuel burning experiments with a copper rod aiming to enhance the burning rate under turbulent conditions.

Based on the understandings and results from the wire experiment and the crude oil burning experiment, the ultimate experiment configuration, which is the hydrocarbon fuel burning with an immersed copper rod on the turbulent water surface is studied in Chapter 4. Dodecane and heptane are used as two types of fuel with different boiling points. Under zero turbulence conditions ($u' = 0$ m/s), the fuel layer burning rate is noticeably affected by the fuel type, or more specifically, the boiling point of the fuel compared to the water boiling point. The dodecane layer (boiling point of 216 °C) burning cases have nucleate boiling on the rod's surface in the water sublayer, while the nucleate boiling occurs on the rod's surface within the fuel layer in the heptane layer (boiling point of 98 °C) burning cases. The different nucleate boiling region causes suppression and facilitation on the dodecane and heptane burning rate respectively. The heat transfer by bubble generation is estimated by bubble counting using highspeed image processing. While the nucleate boiling is not observed for both types of fuel on the rod's surface under turbulence conditions ($u' = 0.017$ and 0.033 m/s), the suppression and facilitation effects by bubbles in no turbulence condition are no longer in consideration, and the convective heat loss at the water interface become a major factor causing a low enhancement by the copper rod. For each burning configuration, a burning rate

formulation coupled with experimental results is used to capture the details in the heat and mass transfer features.

Finally, a theoretical analysis on the effects of multiple copper rods placement is studied using the measurement data adopted from the experiments. The copper rod position is optimized such that the rod's bottom area does not touch the water layer and the heat coming from the rod can be transferred to the fuel layer. The results predict an over 300% increase for dodecane burning rate when 4 copper rods with a diameter of 10 mm are immersed in the fuel layer under turbulence intensity of $u' = 0.03$ m/s. For heptane burning cases, the burning rate increases to more than 400% of the baseline when 3 rods are immersed in the fuel slick. This analysis provides a reasonable engineering basis to determine the number of copper rods required for the Flame Refluxer design to achieve a certain level of enhancement.

This study comprehensively incorporates the experiments from simple configurations to complex forms to answer the questions raised in the introduction. Most importantly, this work provides a novel experimental platform to investigate the Flame Refluxer's performance on a controllable lab scale. Although the heat and mass transfer mechanisms are inherently complicated with the coupling of immersed conductive object and underlayer turbulence, the burning rate formulations can offer an engineering solution to predict the burning rate enhancement using Flame Refluxer during an *in-situ* burning process.

5.2 Suggestions for future work

The fuel slick burning with immersed conductive objects on a turbulent water surface can benefit from this work as it is governed by the same heat and mass transfer mechanisms that were investigated herein. Although, much consideration shall be given to account for the application of the Flame Refluxer in the real-world scenario. A single copper rod is chosen as the experimental subject across this work because of its geometrical symmetry. The measurements of energy used in both heat transfer and nucleate boiling behaviors take advantages of the simple rod geometry. However, metal rods might not be the optimal format for the Flame Refluxer because they can be heavy and hard to deploy. Other shapes like metal sheets are worth investigating because of their

much larger surface-to-volume ratio and cost-effect considerations during the manufacture, transport, and deployment process.

The length scale of the turbulence generated in the confined jet system is fixed to the cylinder diameter. Therefore, the turbulence length scale does not vary much in the current study, and only the change of intensity is investigated. The turbulence in the ocean has a wide range of length scales and intensities. Although to fully reproduce the complex dynamic ocean surface is challenging and lack experimental significance, it is worthy of increasing the tank size so that the fuel-burning behaviors under different turbulence length scales can be studied. It would be very useful as we are expanding the results of this work towards the improvement guidelines on the Flame Refluxer design.

Bibliography

[1]   J. Beyer, H.C. Trannum, T. Bakke, P. V. Hodson, T.K. Collier, Environmental effects of the Deepwater Horizon oil spill: A review, Mar. Pollut. Bull. 110 (2016) 28–51. https://doi.org/10.1016/j.marpolbul.2016.06.027.

[2]   I. Buist, J. Mccourt, S. Potter, S. Ross, K. Trudel, In Situ Burning, Pure Appl. Chem. - PURE APPL CHEM. 71 (1999) 43–65. https://doi.org/10.1351/pac199971010043.

[3]   S. Potter, I. Buist, In-Situ Burning for Oil Spills in Arctic Waters: State-of-the-Art and Future Research Needs, in: 2008. https://doi.org/10.1007/978-1-4020-8565-9_5.

[4]   M. Fitzpatrick, U. S. Coast Guard Arctic Pollution Response Research and Development., in: Ocean. Conf. Rec., 1985. https://doi.org/10.1109/oceans.1985.1160122.

[5]   S.A. Stout, J.R. Payne, Chemical composition of floating and sunken in-situ burn residues from the Deepwater Horizon oil spill, Mar. Pollut. Bull. (2016). https://doi.org/10.1016/j.marpolbul.2016.04.031.

[6]   V.I. Blinov, G.. Khudyakov, Diffusion Burning of Liquids, Army Engineer Research and Development Labs, Fort Belvoir, VA, 1961. https://apps.dtic.mil/sti/citations/AD0296762.

[7]   V. Babrauskas, Estimating large pool fire burning rates, Fire Technol. (1983). https://doi.org/10.1007/BF02380810.

[8]   H. Koseki, H. Hayasaka, Estimation of Thermal Balance in Heptane Pool Fire, J. Fire Sci. (1989). https://doi.org/10.1177/073490418900700402.

[9]   C.H. Thompson, G.W. Dawson, J.L. Goodier, Combustion: An Oil Spill Mitigation Tool, Richland, WA, 1978. https://trid.trb.org/View/152169.

[10]   E.M. Twardus, A study to evaluate the combustibility and other physical and chemical properties of aged oils and emulsions, Waterloo, Ontario, Canada, 1980.

[11]   R.S. Alger, R.C. Corlett, A.S. Gordon, F.A. Williams, Some aspects of structures of turbulent pool fires, Fire Technol. (1979). https://doi.org/10.1007/BF01983759.

[12]   W.W. HILLSTROM, Ignition and Combustion of Unconfined Liquid Fuels, Combust. Sci. Technol. 3 (1971) 179–186. https://doi.org/10.1080/00102207108952285.

[13]   T.J. McMinn, Crude Oil Behavior on Arctic Winter Ice, Washington, D.C, 1973. https://apps.dtic.mil/sti/pdfs/AD0754261.pdf.

[14]   M.A. ALRAMADHAN, V.S. ARPACI, A. SELAMET, Radiation Affected Liquid Fuel Burning on Water, Combust. Sci. Technol. 72 (1990) 233–253. https://doi.org/10.1080/00102209008951649.

[15]   S.E. Petty, Combustion of crude oil on water, Fire Saf. J. (1983).
       https://doi.org/10.1016/0379-7112(83)90005-X.

[16]   I. Glassman, F.L. Dryer, Flame spreading across liquid fuels, Fire Saf. J. (1981).
       https://doi.org/10.1016/0379-7112(81)90038-2.

[17]   D.D. Evans, G.W. Mulholland, H.R. Baum, W.D. Walton, K.B. McGrattan, In situ
       burning of oil spills, J. Res. Natl. Inst. Stand. Technol. (2001).
       https://doi.org/10.6028/jres.106.009.

[18]   M. Arai, K. Saito, R.A. Altenkirch, A Study of Boilover in Liquid Pool Fires Supported
       on Water Part I: Effects of a Water Sublayer on Pool Fires, Combust. Sci. Technol.
       (1990). https://doi.org/10.1080/00102209008951622.

[19]   J.P. Garo, J.P. Vantelon, A.C. Fernandez-Pello, Boilover burning of oil spilled on water,
       Symp. Combust. (1994). https://doi.org/10.1016/S0082-0784(06)80792-7.

[20]   J.P. Garo, J.P. Vantelon, A.C. Fernande-Pello, Effect of the fuel boiling point on the
       boilover burning of liquid fuels spilled on water, Symp. Combust. (1996).
       https://doi.org/10.1016/S0082-0784(96)80367-5.

[21]   J.L. Torero, S.M. Olenick, J.P. Garo, J.P. Vantelon, Determination of the burning
       characteristics of a slick of oil on water, Spill Sci. Technol. Bull. (2003).
       https://doi.org/10.1016/S1353-2561(03)00071-9.

[22]   L.A. Gritzo, V.F. Nicolette, Coupling of large fire phenomenon with object geometry and
       object thermal response, J. Fire Sci. (1997).
       https://doi.org/10.1177/073490419701500601.

[23]   B.L. Bainbridge, N.R. Keltner, Heat transfer to large objects in large pool fires, J. Hazard.
       Mater. (1988). https://doi.org/10.1016/0304-3894(88)87004-3.

[24]   N.R. Keltner, V.F. Nicolette, N.N. Brown, B.L. Bainbridge, Test unit effects on heat
       transfer in large fires, J. Hazard. Mater. (1990). https://doi.org/10.1016/0304-
       3894(90)85068-E.

[25]   A.S. Rangwala, K.S. Arsava, G. Mahnken, X. Shi, A Novel Experimental Approach to
       Enhance Burning Of Oil-Water Emulsions by Immersed Objects, Worcester, 2015.
       https://www.bsee.gov/sites/bsee.gov/files/osrr-oil-spill-response-research/1049aa.pdf.

[26]   H. Sezer, K.S. Arsava, S.P. Kozhumal, A.S. Rangwala, The effect of embedded objects on
       pool fire burning behavior, Int. J. Heat Mass Transf. (2017).
       https://doi.org/10.1016/j.ijheatmasstransfer.2016.12.021.

[27]   H. Sezer, K.S. Arsava, A.S. Rangwala, Oil spill clean-up using immersed metal wool, J.
       Environ. Chem. Eng. (2017). https://doi.org/10.1016/j.jece.2017.09.052.

[28]   K.S. Arsava, G. Mahnken, A.S. Rangwala, Use of immersed conductive objects to

enhance the burning rate of hydrocarbon pool fires, Cold Reg. Sci. Technol. (2018). https://doi.org/10.1016/j.coldregions.2017.12.002.

[29]   K.S. Arsava, A.S. Rangwala, K. Hansen, An offshore in-situ burn enhanced by immersed objects, in: 40th AMOP Tech. Semin. Environ. Contam. Response, 2017.

[30]   K.S. Arsava, V. Raghavan, A.S. Rangwala, Enhanced Oil Spill Clean-Up Using Immersed Thermally Conductive Objects, Fire Technol. (2018). https://doi.org/10.1007/s10694-018-0767-2.

[31]   X. Pi, L. Chang, A.S. Rangwala, The burning rate of a pool fire increased by bubble behaviors during nucleate boiling, Fire Saf. J. (2020). https://doi.org/10.1016/j.firesaf.2020.103097.

[32]   E.D. Skyllingstad, W.D. Smyth, G.B. Crawford, Resonant wind-driven mixing in the ocean boundary layer, J. Phys. Oceanogr. (2000). https://doi.org/10.1175/1520-0485(2000)030<1866:RWDMIT>2.0.CO;2.

[33]   S.A. Thorpe, An introduction to ocean turbulence, 2007. https://doi.org/10.1017/CBO9780511801198.

[34]   A. Gargett, Ocean Turbulence, Annu. Rev. Fluid Mech. (1989). https://doi.org/10.1146/annurev.fluid.21.1.419.

[35]   W.D. Smyth, J.N. Moum, 3D turbulence, in: Encycl. Ocean Sci., 2019. https://doi.org/10.1016/B978-0-12-409548-9.09728-1.

[36]   W.K. Hu, Particle ejection and suspension due to isotropic turbulence, Massachusetts Institute of Technology, 1993. http://hdl.handle.net/1721.1/12634.

[37]   T.L. Morse, H.K. Kytömaa, The effect of turbulence on the rate of evaporation of LNG on water, J. Loss Prev. Process Ind. (2011). https://doi.org/10.1016/j.jlp.2011.06.004.

[38]   A.A. Sonin, M.A. Shimko, C. Jung-Hoon, Vapor condensation onto a turbulent liquid-I. The steady condensation rate as a function of liquid-side turbulence, Int. J. Heat Mass Transf. (1986). https://doi.org/10.1016/0017-9310(86)90164-X.

[39]   J.S. Brown, B.C. Khoo, A.A. Sonin, Rate correlation for condensation of pure vapor on turbulent, subcooled liquid, Int. J. Heat Mass Transf. (1990). https://doi.org/10.1016/0017-9310(90)90230-R.

[40]   B.C. Khoo, A numerical and experimental study of the scalar transport at a turbulent liquid free surface, in: 1988. http://hdl.handle.net/1721.1/4013.

[41]   M. Barchilon, R. Curtet, Some details of the structure of an axisymmetric confined jet with backflow, J. Basic Eng. Trans. ASME. 86 (1964) 777–787. https://doi.org/10.1115/1.3655953.

[42] B.C. Khoo, T.C. Chew, P.S. Heng, H.K. Kong, Turbulence characterisation of a confined jet using PIV, Exp. Fluids. (1992). https://doi.org/10.1007/BF00209510.

[43] S. Nukiyama, The maximum and minimum values of the heat Q transmitted from metal to boiling water under atmospheric pressure, Int. J. Heat Mass Transf. 9 (1966) 1419–1433. https://doi.org/10.1016/0017-9310(66)90138-4.

[44] J.Y. Chang, S.M. You, Heater orientation effects on pool boiling of micro-porous-enhanced surfaces in saturated FC-72, J. Heat Transfer. 118 (1996) 937–943. https://doi.org/10.1115/1.2822592.

[45] H. Wang, X.F. Peng, B.X. Wang, W.K. Lin, C. Pan, Experimental observations of bubble dynamics on ultrathin wires, Exp. Heat Transf. 18 (2005) 1–11. https://doi.org/10.1080/08916150490502253.

[46] J.F. Lu, X.F. Peng, B. Bourouga, Nucleate boiling modes of subcooled water on fine wires submerged in a pool, Exp. Heat Transf. 19 (2006) 95–111. https://doi.org/10.1080/08916150500479414.

[47] X. Pi, A.S. Rangwala, The influence of wire orientation during nucleate pool boiling in subcooled dodecane, Int. J. Heat Mass Transf. 137 (2019) 1247–1257. https://doi.org/10.1016/j.ijheatmasstransfer.2019.03.088.

[48] Y. Iida, K. Tsutsui, Effects of ultrasonic waves on natural convection, nucleate boiling, and film boiling heat transfer from a wire to a saturated liquid, Exp. Therm. Fluid Sci. (1992). https://doi.org/10.1016/0894-1777(92)90059-E.

[49] A. Ozbey, M. Karimzadehkhouei, K. Sefiane, A. Koşar, J.R.E. Christy, On bubble dynamics in subcooled nucleate boiling on a platinum wire, Int. J. Therm. Sci. (2019). https://doi.org/10.1016/j.ijthermalsci.2018.11.007.

[50] A. Duchesne, C. Dubois, H. Caps, Tightrope dancer bubbles, Phys. Rev. Fluids. (2016). https://doi.org/10.1103/physrevfluids.1.050504.

[51] J.F. Klausner, R. Mei, D.M. Bernhard, L.Z. Zeng, Vapor bubble departure in forced convection boiling, Int. J. Heat Mass Transf. 36 (1993) 651–662. https://doi.org/10.1016/0017-9310(93)80041-R.

[52] G.E. Thorncroft, J.F. Klausner, R. Mei, An experimental investigation of bubble growth and detachment in vertical upflow and downflow boiling, Int. J. Heat Mass Transf. 41 (1998) 3857–3871. https://doi.org/10.1016/S0017-9310(98)00092-1.

[53] W. Frost, C.J. Kippenhan, Bubble growth and heat-transfer mechanisms in the forced convection boiling of water containing a surface active agent, Int. J. Heat Mass Transf. 10 (1967). https://doi.org/10.1016/0017-9310(67)90070-1.

[54] L. Lee, B.N. Singh, The influence of subcooling on nucleate pool boiling heat transfer, Lett. Heat Mass Transf. 2 (1975) 315–323. https://doi.org/10.1016/0094-4548(75)90015-

6.

[55] K. Cornwell, The influence of bubbly flow on boiling from a tube in a bundle, Int. J. Heat Mass Transf. 33 (1990) 2579–2584. https://doi.org/10.1016/0017-9310(90)90193-X.

[56] R. Situ, M. Ishii, T. Hibiki, J.Y. Tu, G.H. Yeoh, M. Mori, Bubble departure frequency in forced convective subcooled boiling flow, Int. J. Heat Mass Transf. (2008). https://doi.org/10.1016/j.ijheatmasstransfer.2008.04.028.

[57] H. Chi-Yeh, P. Griffith, The mechanism of heat transfer in nucleate pool boiling-Part I. Bubble initiaton, growth and departure, Int. J. Heat Mass Transf. 8 (1965) 887–904. https://doi.org/10.1016/0017-9310(65)90073-6.

[58] H. Chi-Yeh, P. Griffith, The mechanism of heat transfer in nucleate pool boiling-Part II. The heat flux-temperature difference relation, Int. J. Heat Mass Transf. 8 (1965) 905–914. https://doi.org/10.1016/0017-9310(65)90074-8.

[59] P. Griffith, Discussion: "A Study of Bubble Departure in Forced-Convection Boiling" (Koumoutsos, N., Moissis, R., and Spyridonos, A., 1968, ASME J. Heat Transfer, 90, pp. 223–230), J. Heat Transfer. 90 (1968) 230. https://doi.org/10.1115/1.3597484.

[60] I.P. Vishnev, Effect of orienting the hot surface with respect to the gravitational field on the critical nucleate boiling of a liquid, J. Eng. Phys. (1973). https://doi.org/10.1007/BF00827332.

[61] W. Wu, P. Chen, B.G. Jones, T.A. Newell, A study on bubble detachment and the impact of heated surface structure in subcooled nucleate boiling flows, Nucl. Eng. Des. (2008). https://doi.org/10.1016/j.nucengdes.2008.05.013.

[62] M. Mahamudur Rahman, J. Pollack, M. Mccarthy, Increasing Boiling Heat Transfer using Low Conductivity Materials, Sci. Rep. (2015). https://doi.org/10.1038/srep13145.

[63] Y. Mei, Y. Shao, S. Gong, Y. Zhu, H. Gu, Effects of surface orientation and heater material on heat transfer coefficient and critical heat flux of nucleate boiling, Int. J. Heat Mass Transf. 121 (2018) 632–640. https://doi.org/10.1016/j.ijheatmasstransfer.2018.01.020.

[64] A. Bergles, H. Morton, Survey and evaluation of techniques to augment convective heat transfer, (2011). http://hdl.handle.net/1721.1/61479.

[65] I.L. Pioro, W. Rohsenow, S.S. Doerffer, Nucleate pool-boiling heat transfer. I: Review of parametric effects of boiling surface, Int. J. Heat Mass Transf. (2004). https://doi.org/10.1016/j.ijheatmasstransfer.2004.06.019.

[66] R. Situ, Y. Mi, M. Ishii, M. Mori, Photographic study of bubble behaviors in forced convection subcooled boiling, Int. J. Heat Mass Transf. 47 (2004) 3659–3667. https://doi.org/10.1016/j.ijheatmasstransfer.2004.04.005.

[67] N. Basu, G.R. Warrier, V.K. Dhir, Wall Heat Flux Partitioning During Subcooled Flow Boiling: Part 1- Model Development, J. Heat Transfer. (2005).

[68] T. V. Davies, G.K. Batchelor, The Theory of Homogeneous Turbulence, Math. Gaz. (1954). https://doi.org/10.2307/3609796.

[69] R.R. Long, Theory of turbulence in a homogeneous fluid induced by an oscillating grid, Phys. Fluids. (1978). https://doi.org/10.1063/1.862087.

[70] B.H. Brumley, G.H. Jirka, Near-surface turbulence in a grid-stirred tank, J. Fluid Mech. 183 (1987) 235–263. https://doi.org/10.1017/S0022112087002623.

[71] I.P.D. De Silva, H.J.S. Fernando, Oscillating grids as a source of nearly isotropic turbulence, Phys. Fluids. (1994). https://doi.org/10.1063/1.868193.

[72] V. Aumelas, Y. Lecoffre, G. Maj, J.P. Franc, Micro-bubbles seeding for flow characterization, in: IOP Conf. Ser. Earth Environ. Sci., 2016. https://doi.org/10.1088/1755-1315/49/6/062005.

[73] W. Thielicke, R. Sonntag, Particle Image Velocimetry for MATLAB: Accuracy and enhanced algorithms in PIVlab, J. Open Res. Softw. (2021). https://doi.org/10.5334/jors.334.

[74] M. Raffel, C.E. Willert, S.T. Wereley, J. Kompenhans, S. Willert, S.T. Wereley, J. Kompenhans, Particle Image Velocimetry: A Practical Guide, 2007.

[75] W. Thielicke, E.J. Stamhuis, PIVlab – Towards User-friendly, Affordable and Accurate Digital Particle Image Velocimetry in MATLAB, J. Open Res. Softw. (2014). https://doi.org/10.5334/jors.bl.

[76] P. Mycek, B. Gaurier, G. Germain, G. Pinon, E. Rivoalen, Experimental study of the turbulence intensity effects on marine current turbines behaviour. Part I: One single turbine, Renew. Energy. (2014). https://doi.org/10.1016/j.renene.2013.12.036.

[77] C.T. Crowe, J.D. Schwarzkopf, M. Sommerfeld, Y. Tsuji, Multiphase Flows with Droplets and Particles, 2011. https://doi.org/10.1201/b11103.

[78] R.A. Gore, C.T. Crowe, Effect of particle size on modulating turbulent intensity, Int. J. Multiph. Flow. (1989). https://doi.org/10.1016/0301-9322(89)90076-1.

[79] A. Duchesne, H. Caps, Walks of bubbles on a hot wire in a liquid bath, Epl. 118 (2017) 44001. https://doi.org/10.1209/0295-5075/118/44001.

[80] D.M. Christopher, J. Jiang, Bubble sweeping and interactions on wires during subcooled boiling, Int. J. Heat Mass Transf. (2009). https://doi.org/10.1016/j.ijheatmasstransfer.2009.04.036.

[81] H. Luo, H.F. Svendsen, Theoretical Model for Drop and Bubble Breakup in Turbulent

Dispersions, AIChE J. (1996). https://doi.org/10.1002/aic.690420505.

[82]   R. Marek, J. Straub, Origin of thermocapillary convection in subcooled nucleate pool boiling, Int. J. Heat Mass Transf. (2001). https://doi.org/10.1016/S0017-9310(00)00124-1.

[83]   T. Koller, T. Klein, C. Giraudet, J. Chen, A. Kalantar, G. Laan, M. Rausch, A. Fröba, Liquid Viscosity and Surface Tension of n -Dodecane, n -Octacosane, Their Mixtures, and a Wax between 323 and 573 K by Surface Light Scattering, J. Chem. Eng. Data. 62 (2017). https://doi.org/10.1021/acs.jced.7b00363.

[84]   D.M. Christopher, H. Wang, X. Peng, Heat transfer enhancement due to Marangoni flow around moving bubbles during nucleate boiling, Tsinghua Sci. Technol. (2006). https://doi.org/10.1016/S1007-0214(06)70229-2.

[85]   H.D. Ross, Ignition of and flame spread over laboratory-scale pools of pure liquid fuels, Prog. Energy Combust. Sci. (1994). https://doi.org/10.1016/0360-1285(94)90005-1.

[86]   A. Ito, K. Saito, T. Inamura, Holographic interferometry temperature measurements in liquids for pool fires supported on water, J. Heat Transfer. (1992). https://doi.org/10.1115/1.2911905.

[87]   N.H. Jason, Alaska Arctic Offshore Oil Spill Response Technology Workshop Proceedings, US Government Printing Office, Washington DC, 1989. https://nvlpubs.nist.gov/nistpubs/Legacy/SP/nistspecialpublication762.pdf.

[88]   C. Bech, P. Sveum, I. Buist, The effect of wind, ice and waves on the in-situ burning of emulsions and aged oils, (1993). https://inis.iaea.org/search/search.aspx?orig_q=RN:25063980 (accessed August 22, 2020).

[89]   A. Putorti, D. Evans, E. Tennyson, Ignition of Weathered and Emulsified Oils (NIST SP 995), (2003). https://tsapps.nist.gov/publication/get_pdf.cfm?pub_id=911215.

[90]   J.P. Garo, H. Koseki, J.P. Vantelon, C. Fernandez-Pello, Combustion of liquid fuels floating on water, Therm. Sci. (2007). https://doi.org/10.2298/TSCI0702119G.

[91]   H. Koseki, G.W. Mulholland, The effect of diameter on the burning of crude oil pool fires, Fire Technol. (1991). https://doi.org/10.1007/BF01039527.

[92]   X. Shi, P.W. Bellino, A. Simeoni, A.S. Rangwala, Experimental study of burning behavior of large-scale crude oil fires in ice cavities, Fire Saf. J. (2016). https://doi.org/10.1016/j.firesaf.2015.11.007.

[93]   H.F. Farahani, X. Shi, A. Simeoni, A.S. Rangwala, A study on burning of crude oil in ice cavities, Proc. Combust. Inst. (2015). https://doi.org/10.1016/j.proci.2014.05.074.

[94]   L. Van Gelderen, N.L. Brogaard, M.X. Sørensen, J. Fritt-Rasmussen, A.S. Rangwala, G. Jomaas, Importance of the slick thickness for effective in-situ burning of crude oil, Fire Saf. J. (2015). https://doi.org/10.1016/j.firesaf.2015.07.005.

[95] M. Fingas, An Overview of In-Situ Burning, in: Oil Spill Sci. Technol., 2011. https://doi.org/10.1016/B978-1-85617-943-0.10023-1.

[96] J. McCourt, I. Buist, J. Mullin, B. Pratte, W. Jamieson, Continued development of a test for fire booms in waves and flames, in: Environ. Canada Arct. Mar. Oil Spill Progr. Tech. Semin. Proc., 1998.

[97] D. Drysdale, An Introduction to Fire Dynamics: Third Edition, 2011. https://doi.org/10.1002/9781119975465.

[98] B. McCaffrey, Purely buoyant diffusion flames: some experimental results, NBSIR 79-1910, Natl. Bur. Stand. (1979). https://doi.org/NBSIR 79-1910.

[99] G. Cox, Combustion fundamentals of fire, London: Academic, 1995.

[100] L. Chang, A.S. Rangwala, The Influence of Turbulence on Subcooled Nucleate Pool Boiling, Int. J. Heat Mass Transf. 165 (2021) 120694. https://doi.org/https://doi.org/10.1016/j.ijheatmasstransfer.2020.120694.

[101] K. Steckler, T. Kashiwagi, H. Baum, K. Kanemaru, Analytical Model For Transient Gasification Of Noncharring Thermoplastic Materials, Fire Saf. Sci. (1991). https://doi.org/10.3801/iafss.fss.3-895.

[102] K. Butler, Analytical Model of Pyrolysis for a Finite Thickness Sample on a Semi-Infinite Base., in: National Institute of Standards and Technology. Annual Conference on Fire Research: Book of Abstracts, Gaithersburg, MD, 1996. https://tsapps.nist.gov/publication/get_pdf.cfm?pub_id=916671.

[103] C.L. Beyler, Fire hazard calculations for large, open hydrocarbon fires, in: SFPE Handb. Fire Prot. Eng. Fifth Ed., 2016. https://doi.org/10.1007/978-1-4939-2565-0_66.

[104] J.E. Sargison, S.M. Guo, M.L.G. Oldfield, G.D. Lock, A.J. Rawlinson, A converging slot-hole film-cooling geometry-Part 1: Low-speed flat-plate heat transfer and loss, J. Turbomach. (2002). https://doi.org/10.1115/1.1459735.

[105] A. goleman, daniel; boyatzis, Richard; Mckee, Stephen R. Turns - An Introduction to Combustion Concepts and Applications-McGraw-Hill (2012), 2019.

[106] P.L. Blackshear, Heat transfer in fires: thermophysics, social aspects, economic impact, Scripta Book Co., Washington, 1974.

[107] F. Incropera, D.DeWitt, T. Bergman, A.Lavine, Fundamentals of heat and mass transfer - Sixth edition, 2005.

[108] J.G. Quintiere, Fundamentals of Fire Phenomena, 2006. https://doi.org/10.1002/0470091150.

[109] H. Lhuissier, E. Villermaux, Bursting bubble aerosols, J. Fluid Mech. (2012).

https://doi.org/10.1017/jfm.2011.418.

[110] S. Poulain, E. Villermaux, L. Bourouiba, Ageing and burst of surface bubbles, J. Fluid Mech. (2018). https://doi.org/10.1017/jfm.2018.471.

[111] Tewarson, Generation of Heat and Chemical Compounds in Fires, SFPE Handb. Fire Prot. Eng. Third Ed. (2002).

[112] S.W. Churchill, M. Bernstein, A correlating equation for forced convection from gases and liquids to a circular cylinder in crossflow, J. Heat Transfer. (1977). https://doi.org/10.1115/1.3450685.

[113] D.B. Spalding, Combustion of liquid fuels, Nature. (1950). https://doi.org/10.1038/165160a0.

[114] Q.S. Kang, S.X. Lu, B. Chen, Experimental study on burning rate of small scale heptane pool fires, Chinese Sci. Bull. (2010). https://doi.org/10.1007/s11434-009-0741-y.

Appendix 1: Experimental setup photos

Few photos are presented to show the experimental setup details.

Figure A1. 1: Top view of the turbulence generation system bottom.

The center nozzle (inner diameter of 1.27 cm) directs the confined jet upwards into the cylinder (inner diameter of 10 cm). Two suction ports are placed adjacent to the jet nozzle to recirculate the water back to the pump.

Figure A1. 2: The pump used in the turbulence generation system.

A magnetic drive pump with capacity of 1325 gallons per hour (GPH) is used in the turbulence generation system. This type of centrifugal pump can deliver steady and constant flow which minimizes the water surface periodic oscillation. The propeller is indirectly driven by the

magnetic force from the motor section, so there is no over-heating issue when the flow rate is low. This pump is overall quite during operation and has low vibrations.

Figure A1. 3: The flow meter used in the used in the turbulence generation system.

A turbine type flow meter is used to measure the volumetric flow rate in the pipeline. The readings are obtained by the rotation speed of the propeller within the meter. A metal mesh filter should be installed at the inlet to avoid any potential damage to the propeller. The flow meter needs to be calibrated with water before used in the experiments.


Figure A1. 4: The pipelines and control valve in the turbulence generation system.

The pipelines coming from the two suction ports join before attaching to the pump inlet. A manually control valve is used to adjust the flow rate by turning the handle and checking the flow meter readings.

Figure A1. 5: Quick adjustable frame for holding the copper rod.

The copper rod is clamped on a height adjustable frame. Two quick release mechanisms are used for the ease of changing the rod position. The base is wider than the turbulence generation system and open in one direction (back) so that the whole structure can be slide in position.
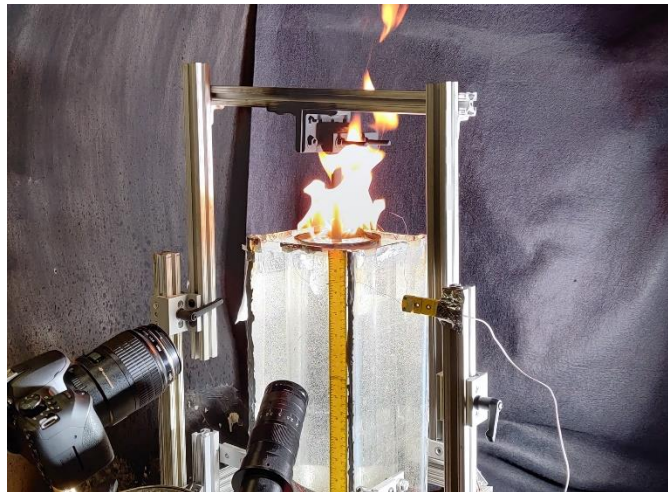
Figure A1. 6: The photograph of fuel layer burning in the turbulence generation system with a copper rod hold by the adjustable frame.

Appendix 2: Particle Image Velocimetry (PIV) measurements

A2.1 Software

PIVlab – an open research software based on MATLAB (https://pivlab.blogspot.com).

Reference:

- W. Thielicke, E.J. Stamhuis, (2014) PIVlab – Towards User-friendly, Affordable and Accurate Digital Particle Image Velocimetry in MATLAB, J. Open Res. Softw. https://doi.org/10.5334/jors.bl.
- W. Thielicke, R. Sonntag, (2021) Particle Image Velocimetry for MATLAB: Accuracy and enhanced algorithms in PIVlab. J. Open Res. Softw, 9: 12. DOI: https://doi.org/10.5334/jors.334)

A2.2 Camera optical criteria

Figure A2. 1: The highspeed camera used for PIV image capture.

Chronos 1.4 highspeed camera with microscope lens are used to capture the tracer movements. The camera is set to record at a resolution of 1280×1024 at 1057 FPS for 8 seconds for each turbulence intensity (root-mean-square (RMS) velocity, u') measurement. The recording image window is 68×55 mm at the water surface.
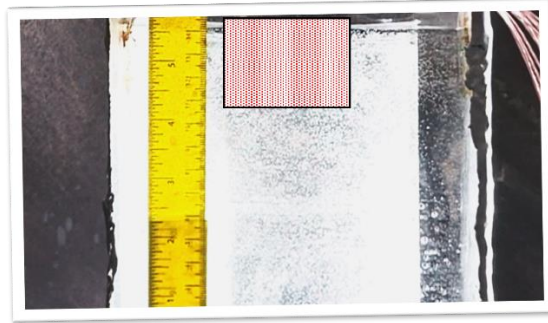
Figure A2. 2: Highspeed recording window (68 X 55 mm) position at the water surface.

PIV setting:

1. Multi-pass (4) with fast Fourier transform (FFT) window deformation
2. The interrogation areas are set to 1.7×1.7 mm (32×32 pixels) with 50% overlap
3. The interrogation area resolution approximately follows the "1/4" rule that the tracer displacement is about 0.03 mm between frames to ensure the detection
4. 3000 frames are analyzed to output the RMS velocity under each flow rate through the jet nozzle

A2.3 Tracer particles

Micro air bubbles with diameter of around 100 μm are used as tracer or seeding particles. The air bubbles were formed due to the break-ups of air pocket initially in the pipelines when the pump is turned on. The diameter of the bubbles is measured near the surface.
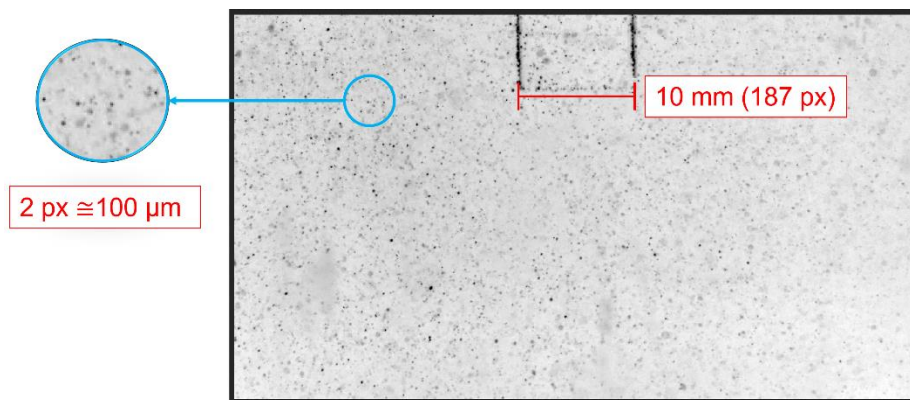

Figure A2. 3: The measurement of the air bubble diameter.

A 10 mm thin metal strip is placed into the frame as a scale reference which measured to have 187 pixels. Each air bubble takes about 2 pixels in the image which equals to 100 μm in diameter.

The bubbles should be small enough to follow the Stokes law, the non-dimensional velocity error induced by gravitational force is given by:

$$\frac{\Delta U}{U} = \frac{d_b{}^2 (\rho_L - \rho_G)}{18 \, \mu_L} \gamma \frac{1}{U}$$

where d_b is the bubble size, γ notes the acceleration field, ρ_L and ρ_G are the gas and liquid densities, U is the flow velocity.
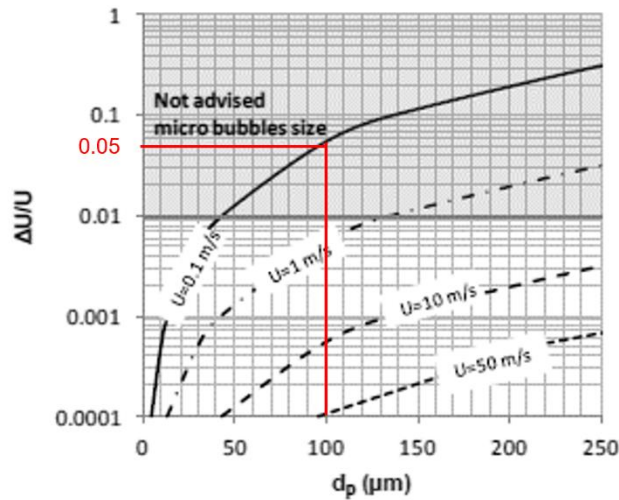
Figure A2. 4: Theoretical non-dimensional velocity deviation due to gravitational force for air bubbles.

(V.Aumelas, Y.Lecoffre, G.Maj, J.-P.Franc, Micro-bubbles seeding for flow characterization. (2016). *IOP Conference Series: Earth and Environmental Science*, Volume 49, Issue 6)

For 10 cm/s flow, 100 μm air bubble has velocity deviation from the flow of ~5%.

To measure the air bubbles size across the image frame. A MATLAB algorithm is used:

a.

```
clear all;clc;close all
I=imread('count.jpg');
% A2=A(:,:,1)+A(:,:,2)+A(:,:,3);    % a bit more contrast
A2=I(:,:,2);  % since green marker used no need for red blue layers
th1=190;
A2(A2>th1)=255;
A2(A2<th1)=0;
A20=~A2;
area_threshold=6;
Ibinary = bwareaopen(A20,area_threshold);
figure(10);imshow(Ibinary);


C = 0.000045; % Conversion factor m/pixel. This was a guess, you shoul
[labeledImage, numberOfBlobs] = bwlabel(Ibinary);
blobMeasurements = regionprops(labeledImage, 'Centroid','EquivDiameter'); % I believe equivalent diameter is a good way to measure size,
                                                                          % you can also check different metrics
% Get equivalent diameter
EquivDiameter = [blobMeasurements.EquivDiameter];
ValidDia = find(EquivDiameter>0.2); % Some empiric threshold
blobMeasurements = blobMeasurements(ValidDia);
EquivDiameter        = EquivDiameter(ValidDia);
% Probability estimation of size
figure,histogram(EquivDiameter*C,'Normalization','probability'),xlabel('Size[m - uncalibrated]'),ylabel('Probability')
% Display some particles
figure, imshow(Ibinary); hold on
% Display areas on image
for idx = 1:2: length(ValidDia)          % Loop through all blobs.
    Centroid = [blobMeasurements(idx).Centroid(1), blobMeasurements(idx).Centroid(2)];
    DiamSize = ['Diam. = ', num2str((EquivDiameter(idx)*C))];
    text(Centroid(1), Centroid(2), DiamSize, 'Color', 'c');
    viscircles(Centroid,EquivDiameter(idx)/2);
end
```
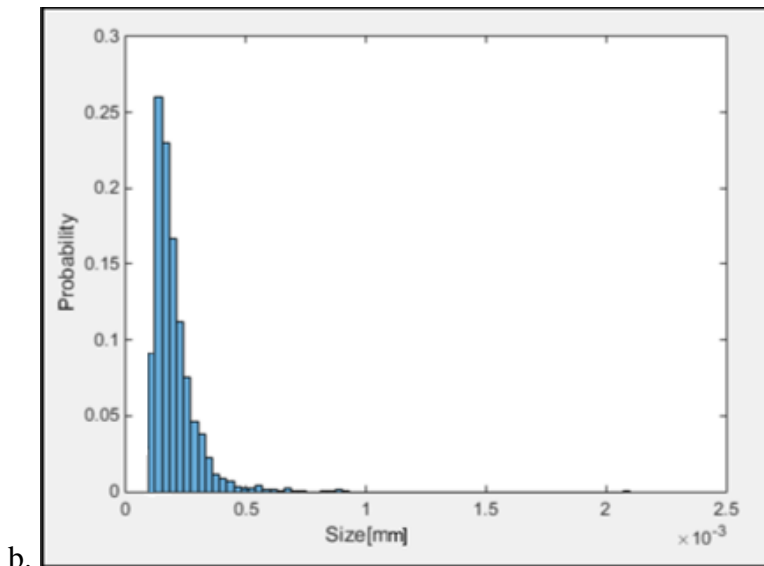
Acquiring image and processing

Calibrating pixel length (m/px)

Processing on diameter and probability estimation

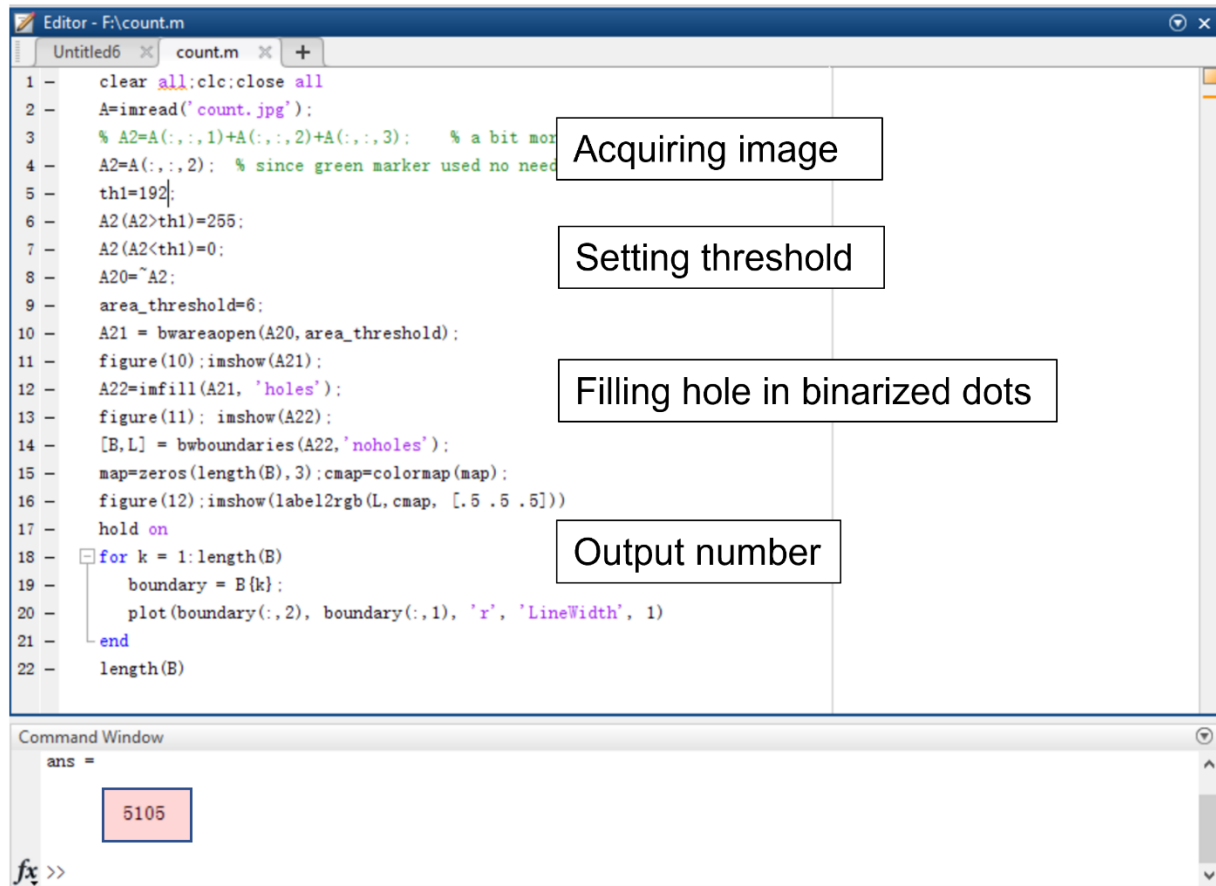Output size distribution

b.

Figure A2. 5: Measurement of the bubble (tracer particle) size. (a) Algorithm. (b) Probability distribution results.

142

To measure the total number of particles in the fame:


```
Editor - F:\count.m
Untitled6 ×   count.m ×   +
1 -     clear all;clc;close all
2 -     A=imread('count.jpg');
3       % A2=A(:,:,1)+A(:,:,2)+A(:,:,3);    % a bit mor
4 -     A2=A(:,:,2);  % since green marker used no need
5 -     th1=192;
6 -     A2(A2>th1)=255;
7 -     A2(A2<th1)=0;
8 -     A20=~A2;
9 -     area_threshold=6;
10 -    A21 = bwareaopen(A20,area_threshold);
11 -    figure(10);imshow(A21);
12 -    A22=imfill(A21, 'holes');
13 -    figure(11); imshow(A22);
14 -    [B,L] = bwboundaries(A22,'noholes');
15 -    map=zeros(length(B),3);cmap=colormap(map);
16 -    figure(12);imshow(label2rgb(L,cmap, [.5 .5 .5]))
17 -    hold on
18 -    for k = 1:length(B)
19 -        boundary = B{k};
20 -        plot(boundary(:,2), boundary(:,1), 'r', 'LineWidth', 1)
21 -    end
22 -    length(B)

Command Window
    ans =

        5105
fx >>
```

Acquiring image

Setting threshold

Filling hole in binarized dots
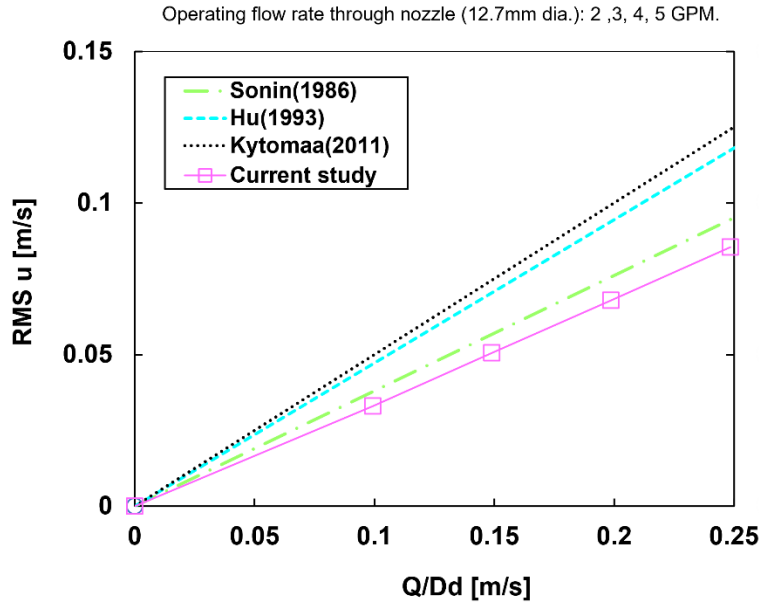
Output number

Figure A2. 6:: Measurement of the bubble (tracer particle) number.

The number of about 5100 particles in the highspeed camera recording area corresponds to the particle image density of 8 (number of tracers per interrogation area).

Operating flow rate through nozzle (12.7mm dia.): 2 ,3, 4, 5 GPM.

Figure A2. 7: Measurement results of u' compared with literatures using the confined jet turbulence generation system Q/Dd is the characteristic velocity [m/s]. Q, flow rate through the nozzle [m³/s]. D, diameter of the cylinder [m]. d, diameter of the nozzle [m].

The convergence analysis shows that at least 500 velocity data is required for u' calculation. The 3000 data used in this study is appropriate.
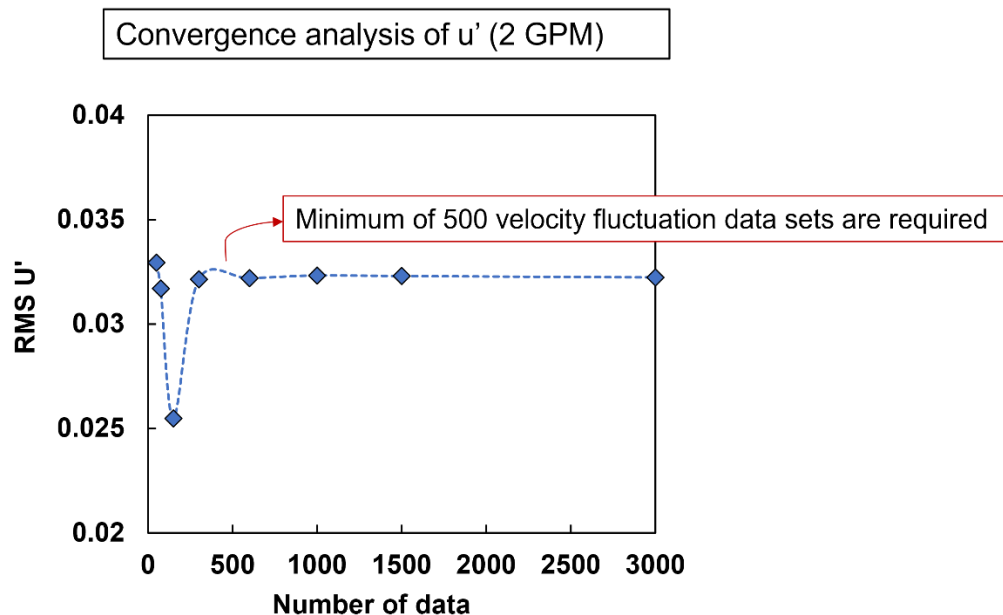
Figure A2. 8: Convergence analysis of required data number for turbulence measurement.

Appendix 3: Calibration of nichrome wire electrical resistance vs. temperature

The nucleate boiling experiments in Chapter 2 applied thin nichrome wire with diameter of 0.127 mm so it could be impossible to directly measure the wire temperature. Therefore, an alternative method, based on the relationship between wire resistance and temperature was used. The wire was placed in an oil bath which is slowly heated in a pan from 50 – 150 °C. A thermocouple was place near the wire and the oil temperature was assumed to be same as the wire temperature because the wire is extremely thin. A multimeter was used to measure the resistance change of the wire. During the heating process, the temperature and corresponding resistance results were recorded.
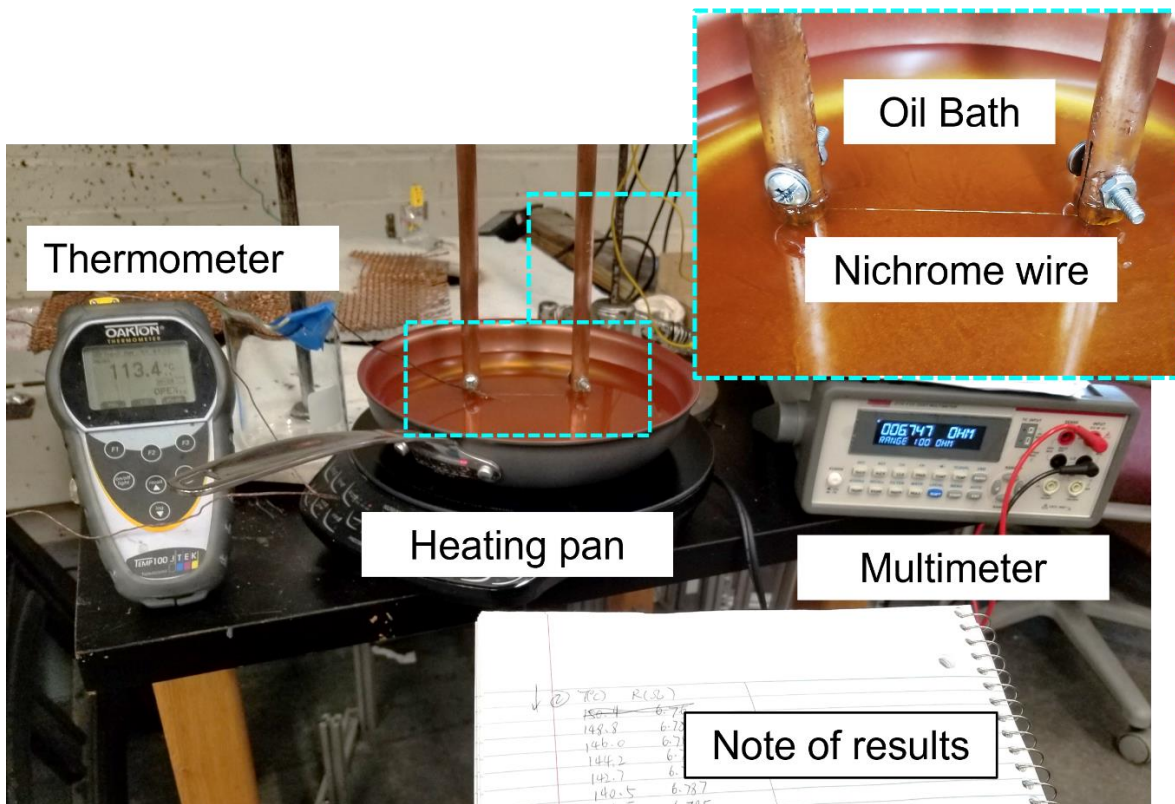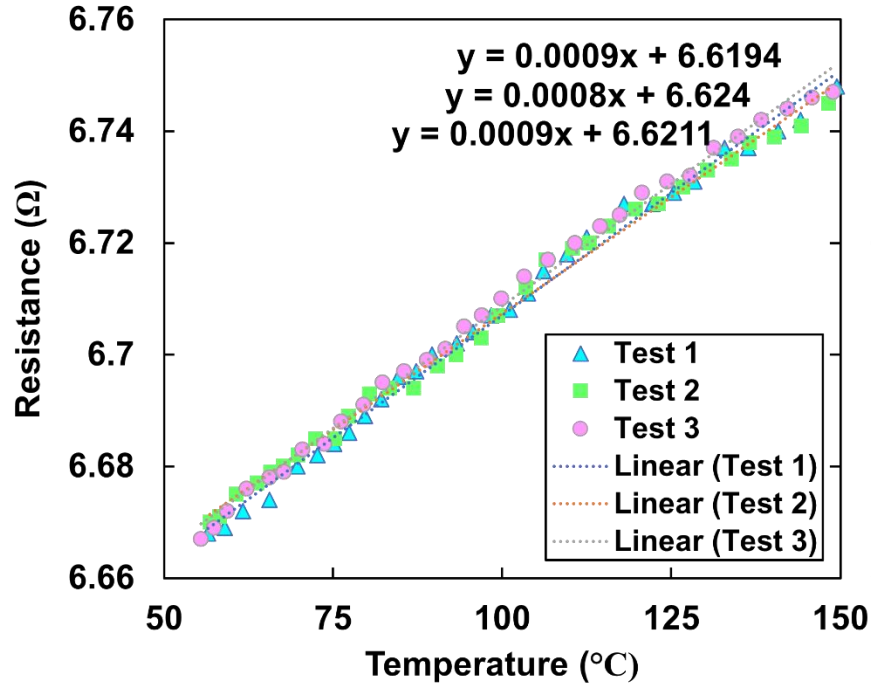

Figure A3. 1: Resistance vs. temperature calibration experiment.

The experiment was repeated three times and the curves have good consistence. The relationship between resistance and temperature can be expressed as: $R = \alpha T + R_0$, and the coefficient α is 9×10^{-4} $\Omega/°C$

Figure A3. 2: Temperature calibration results.

The wire measurements could be very sensitive as any particulate attached to the wire during the process of the experiment. To avoid change of resistance, the test wire was carefully cleaned before each experiment.

Appendix 4: Algorithm for flame height measurement

```
close all
clear all
clc

%VIDEO TO FRAMES: WPI
%%%Script combined from the codes used in Fire Laboratory of
WPI%%%
%Navigating to the desired working folder
uiwait(msgbox('Select folder for the video','modal'));
path_vid=uigetdir;
cd(path_vid);


%loading the video into matlab
uiwait(msgbox('Select the video','modal'));
vidname=uigetfile('*.mp4'); %getting the name of vid through UI
vid=VideoReader(vidname); %creating the vid object


% User Input to determine when to start and stop processing the
video
uiwait(msgbox('Specify start & stop time','modal'))
b=inputdlg('Enter starting time in seconds');
t_start=str2num(b{1});
b=inputdlg('Enter ending time in seconds');
t_end=str2num(b{1});

%User Input to for cropping the video to desired size
answer='No';
uiwait(msgbox('Crop the picture by dragging and then double-
click inside the square to finalize','modal'))
while strcmp(answer,'No')
    [crop,dim]=imcrop(readFrame(vid)); %GUI
    close all;
    dim=int16(dim);% converting to integer
    xmi=dim(2);   %getting the xmin,xmax,ymin,ymax coordinates
    xma=dim(2)+dim(4)-1;
    ymi=dim(1);
    yma=dim(1)+dim(3)-1;
    b=readFrame(vid);
    imshow(b(xmi:xma,ymi:yma,:));
    answer=questdlg(' Is this good?');
    if strcmp(answer,'No')
```

```matlab
        uiwait(msgbox('Try again !','modal'));
    end
end
close all

%msgbox('Processing...')

% Going from vid to img
dur=t_end-t_start; % duration of the segment of vid to treat
nmb_of_frame=int16(dur*vid.Framerate); %number of frames to
treat
nmb_of_frame=double(nmb_of_frame);



%loading the video into matlab
uiwait(msgbox('Select the video','modal'));
vidname=uigetfile('*.mp4'); %getting the name of vid through UI
vid=VideoReader(vidname); %creating the vid object



% User Input to determine when to start and stop processing the
video
uiwait(msgbox('Specify start & stop time','modal'))
b=inputdlg('Enter starting time in seconds');
t_start=str2num(b{1});
b=inputdlg('Enter ending time in seconds');
t_end=str2num(b{1});

%User Input to for cropping the video to desired size
answer='No';
uiwait(msgbox('Crop the picture by dragging and then double-
click inside the square to finalize','modal'))
while strcmp(answer,'No')
    [crop,dim]=imcrop(readFrame(vid)); %GUI
    close all;
    dim=int16(dim);% converting to integer
    xmi=dim(2);   %getting the xmin,xmax,ymin,ymax coordinates
    xma=dim(2)+dim(4)-1;
    ymi=dim(1);
    yma=dim(1)+dim(3)-1;
    b=readFrame(vid);
    imshow(b(xmi:xma,ymi:yma,:));
    answer=questdlg(' Is this good?');
    if strcmp(answer,'No')
        uiwait(msgbox('Try again !','modal'));
    end
end
```

```matlab
close all

%msgbox('Processing...')

% Going from vid to img
dur=t_end-t_start; % duration of the segment of vid to treat
nmb_of_frame=int16(dur*vid.Framerate); %number of frames to
treat
nmb_of_frame=double(nmb_of_frame);

%CODE TO FIND FLAME HEIGHT

for i = t_start:60:t_end    %saving every minute
     vid.CurrentTime= i
    img=readFrame(vid);

imwrite(img(xmi:xma,ymi:yma,:),['img_',num2str(i,'%05d'),'.png']
) % writing the pictures
end
%}

clear a;
n=1;
for k=t_start:60:t_end
    check=0;
    img=imread(['img_',num2str(k,'%05d'),'.png']);
    img=rgb2gray(img);
    img=imbinarize(img);
    img=im2double(img);

  sum=0;
  dim=size(img);

  for i=3:1:dim(1)-3    %skipping first 3 and last 3 pixels
      sum=0;
      for j=3:1:dim(2)-3  %skipping first 3 and last 3 pixels
            sum=sum+img(i,j);
      end
      a(i-2,1,n)=i;
      a(i-2,2,n)=sum;

      if(sum>0)
          flhtp(n)=dim(1)-3-i;
          check =1;
        break;
      end
```

```
        end

    if(check==0)
       flhtp(n)=0;
    end
    n=n+1;
end
flhtcm
length=10; %in cm
no_of_pixel=360; %obtain pixels for known distance
m_per_pixel=length/no_of_pixel;
    flhtcm= flhtp*m_per_pixel;          %flame height in cm
    flhtcm=flhtcm';
```